Title
Fluid Mechanics Problems Motivated by Gravure Printing of Electronics

Author
Ceyhan, Umut

Publication Date
2016

Peer reviewed|Thesis/dissertation

Fluid Mechanics Problems Motivated by Gravure Printing of Electronics

by

Umut Ceyhan

A dissertation submitted in partial satisfaction of the

requirements for the degree of

Doctor of Philosophy

in

Engineering - Mechanical Engineering

in the

Graduate Division

of the

University of California, Berkeley

Committee in charge:

Professor Stephen Morris, Chair
Professor Andrew Szeri
Professor Per-Olof Persson

Spring 2016

Fluid Mechanics Problems Motivated by Gravure Printing of Electronics

Abstract

Fluid Mechanics Problems Motivated by Gravure Printing of Electronics

by

Umut Ceyhan

Doctor of Philosophy in Engineering - Mechanical Engineering

University of California, Berkeley

Professor Stephen Morris, Chair

During intaglio (gravure) printing, a blade wipes excess ink from the engraved plate with the object of leaving ink–filled cells defining the image to be printed. That objective is not completely attained. Capillarity draws some ink from the cell into a meniscus connecting the blade to the substrate, and the continuing motion of the engraved plate smears that ink over its surface. That smear behind the cell delivers a feature lacking in sharpness. Even though the smear formation occurs at micron scale, it affects the functionality at the scale of micron size printed electronics. By examining the limit of vanishing capillary number (Ca, based on substrate speed), we reduce the problem of determining smear volume to one of hydrostatics. Using numerical solutions of the corresponding free boundary problem for the Stokes equations of motion, we show that the hydrostatic theory provides an upper bound to smear volume for finite Ca; as Ca is decreased, smear volume increases. The theory explains why polishing to reduce the tip radius of the blade is an effective way to control smearing. As the motion continues, smear volume under the meniscus is printed as a tail behind the cell extending back toward the blade. In the limit of vanishing Ca, an inner and outer analysis of the meniscus printing problem shows that the meniscus rotates around the pinned contact line at the trailing edge of the cell, and the volume under the meniscus is used to coat a film of thickness decreasing linearly in time forming a tail shape. The tail lengthens with decreasing Ca, owing to the concomitant increase in smear volume; the opposite is true as Ca approaches $O(1)$. For small Ca, it is computationally expensive to use the Stokes solver to show that the physical mechanism of tail formation described by the analysis as $Ca \to 0$ is correct. Lubrication theory, on the other hand, predicts tail formation mechanism closely for contact angles over the blade close to $\pi/2$, and this motivates us to use the lubrication model for smaller Ca. With the continuing motion of substrate, we show the transition from the tip region (squeeze film) to the Landau-Levich film in the form of a tail shape extending back toward the bulk meniscus (static), and this agrees with the physical picture described by the analysis as $Ca \to 0$. The results contribute to the control and understanding of smear formation mechanism during gravure printing of electronics.

To my parents

Contents

Contents **ii**

List of Figures **iv**

1 Introduction **1**
1.1 Gravure printing and smear formation during gravure printing of electronics 1
1.2 Fluid mechanics problems during wiping and outline of the dissertation . . . 3

2 Development and Testing of a Numerical Method for the Stokes Problem **9**
2.1 Problem formulation . . . 10
2.2 Numerical method . . . 12
2.2.1 Galerkin formulation . . . 12
2.2.2 Discretization . . . 14
2.2.3 Time integration . . . 16
2.3 Validation of the solver . . . 17
2.3.1 Flow through a slit . . . 17
2.3.2 Overdamped capillary wave problem . . . 19
2.3.3 Stick–slip problem . . . 25

3 Meniscus Growth During Wiping **29**
3.1 Analysis as $Ca \to 0$ . . . 30
3.2 Hydrostatic limit when $Ca \to 0$ . . . 31
3.3 Viscous effects . . . 34
3.4 Blade geometry . . . 38

4 Tail Formation **41**
4.1 Outer problem: static prediction . . . 41
4.2 Inner problem: viscous effect . . . 44
4.3 Composite expansion . . . 47
4.4 Later stage of tail formation in the limit $Ca \to 0$ . . . 52
4.5 Tail formation studied using numerical solution of Stokes equations with no cell 54
4.6 Tail formation studied using numerical solution of Stokes equations with cell 59

4.7 Lubrication analysis 65
4.7.1 A model for smear formation including the cell 65
4.7.2 Model for meniscus printing 69
4.7.3 Effect of a sequence of cells on tail formation 74

5 Conclusions **77**

A Numerical Method for Lubrication Analysis **79**

B Numerical Integration of Inner Viscous Problem over Semi–Infinite Domain **82**

Bibliography **84**

List of Figures

1.1 Schematic of gravure printing. 2

2.1 Flow domain Ω for the Stokes problem of smearing: S_1, wiper blade; S_2, cell boundary; S_3, free surface. Coordinate axis is fixed on wiper blade which is stationary, cell translates with velocity $U\boldsymbol{i}$. T is the trailing edge, B is the leading edge of the cell and the contact line is at H. The aspect ratio of the cell is set to $L/d = 2$ where L is the length of the cell, d is the depth of the cell. 10
2.2 Nodal points in the isoparametric plane: 1 to 6 is used for $P2$ element, 1 to 3 is used for $P1$ element. 14
2.3 Geometry for the flow through a slit. 17
2.4 Comparison of the numerical solution of the Stokes problem with exact solution of flow through a slit at $x = 0$. 19
2.5 Streamlines of the flow through a slit, corresponding to figure 2.3. 19
2.6 Overdamped capillary wave problem: solution domain; streamlines are obtained from the numerical solution corresponding to the interface perturbed with amplitude a=0.01 at $t = 0$. 20
2.7 Comparison of numerical solution of the Stokes problem with the exact solution of overdamped capillary–wave problem: (a) v–velocity on free surface at $t = 0$, 2–norm of the difference is 3.0525e-6, (b) Comparison of the Stokes solution and perturbation solution: u–velocity on free surface at $t = 0$, 2–norm of the difference is 2.3769e-05. See text for the discussion on the discrepancy in u-velocity and the definition of the 2–norm is given in (2.35). 21
2.8 Comparison of the numerical solution of the Stokes problem and perturbation solution of the overdamped capillary–wave problem: x and y–velocity at the mid of the domain at $t = 0$; 2-norm of the difference in u is 1.0259e-5 and in v is 1.1537e-05. 22
2.9 Comparison of the numerical solution of the Stokes problem and perturbation solution of the overdamped capillary–wave problem: evolution of the interface. . 23
2.10 Comparison of the numerical solution of the Stokes problem and perturbation solution of the overdamped capillary–wave problem: pressure on interface at $t = 0.1$. 24
2.11 Stick–slip problem domain. 25

2.12 Comparison of the numerical solution of the Stokes problem and Richardson solution for stick–slip problem: centerline and slip plane u-velocity. 26
2.13 Comparison of the numerical solution of the Stokes problem and Richardson solution for stick–slip problem: centerline pressure. 27
2.14 Convergence of the method: convergence is given both in terms of infinity and 2-norm errors for pressure and u-velocity (error is obtained by taking the norm of the difference between computed and correct solution), h is the element size, s is the slope. 28

3.1 Flow domain Ω for the Stokes problem of smearing: S_1, wiper blade; S_2, cell boundary; S_3, free surface. Wiper blade is stationary, cell translates with velocity $U\boldsymbol{i}$. 30
3.2 Cell translating rightwards beneath a stationary blade occupying the second quadrant of the xOy plane: (a) cell emerging; (b) cell fully emerged. See text for discussion. 32
3.3 Interface shape at the instant $t = 0.95$ the trailing edge of the cell leaves the blade; L/d=2, $\theta = \pi/6$. Curve (a) hydrostatic; curves (b) to (g), computed for $Ca = 0.025, 0.1, 0.25, 0.5,$ 1 and 2. Inset, ratio v_0/U of contact line velocity to substrate velocity. 35
3.4 Streamlines corresponding to curves (b) to (d) in figure 3.3. Region $0 < x/L < 0.5$, $-0.125 < y/L < 0.25$ and (a), Ca= 0.025; (b), 0.10 and (c) 0.25. 35
3.5 Interface shape at the instant $t = 1.35$ the trailing edge of the cell is at $x/L = 0.4$. For θ and L/d, see caption to figure 3.3. Curve (a), hydrostatic; curves (b) to (e), computed for $Ca = 0.0025, 0.005, 0.01$ and 0.025. Inset, ratio v_0/U of contact line velocity to substrate velocity. 36
3.6 Flow rate at the trailing edge of the cell; configuration as in figure 3.5. 37
3.7 Relation defined by (3.15) and (3.16) for L/d=2, and contact angle $\theta \uparrow \pi/2$. Solid curve, equation (3.16); dotted curve, small–β asymptote (3.17). 39
3.8 Meniscus of a marginally wetting liquid beneath a parabolic blade. 40

4.1 Meniscus sitting between blade and trailing edge (T) of the cell. 41
4.2 Relation between r and distance $x_T = |OT|$ for $\theta = 0$ (solid line), $\theta = \pi/6$ (dashed line). 43
4.3 Inner problem: meniscus pinned at the trailing edge T of the cell, x grows into the meniscus. 44
4.4 Inner viscous solution for the meniscus printing problem, (a) $\phi = 0$, (b) steady state solution. $\phi_0 = 0.468$ is taken to be corresponding to the problem with contact angle on the blade is $\theta = \pi/6$. Inset: the neighborhood of the contact line in linear scale corresponding to curve (a). 46
4.5 Effect of viscosity: meniscus is displaced by an amount δ as the trailing edge T advances. 47
4.6 Geometry for the composite expansion. 48

4.7 Composite expansion $(y^C - y^P)/L$ for $\theta = 5\pi/12$; (top) $Ca = 10^{-7}$,(bottom) $Ca = 10^{-8}$; we have subtracted parabolic interface to be able to see the structure at the tip. The inset scale is the same as the main figure axes. See text for the values of α and ϕ. 51
4.8 Coating of a Landau–Levich film. 52
4.9 For a fixed point on substrate, expected tail formation. 53
4.10 Geometry of the meniscus sitting between blade and trailing edge (T) of the cell. 54
4.11 Time evolution of meniscus printing computed using Stokes equations, $Ca = 0.001$, $\theta = \pi/6$. 55
4.12 Comparison of the static prediction and Stokes solution of meniscus printing problem, $Ca = 0.001$, $\theta = \pi/6$: (a) $x/L = 0.5096$, (b) $x/L = 0.5596$, (c) $x/L = 0.6596$; (—) Stokes solution, (- - -) static prediction. 56
4.13 Comparison of the inner viscous solution and Stokes solution. - - -: inner solution solution, —: the difference u/L between Stokes solution and static prediction at the corresponding time. Inner solution is obtained using α and x/L corresponding to Stokes problem solved for $Ca = 0.001$, $\theta = \pi/6$, $x/L = x_0/L + 0.23$. 57
4.14 Comparison of the inner viscous solution and Stokes solution. - - -: inner solution, —: the difference u/L between Stokes solution and static prediction at the corresponding time. Inner solution solution is obtained using α and x/L corresponding to Stokes problem solved for $Ca = 0.001$, $\theta = 5\pi/12$, $x/L = x_0/L + 0.2$. 58
4.15 Geometry of the domain for tail formation problem, cell translating rightwards beneath a stationary blade occupying the second quadrant of the xOy plane: (a) cell fully emerged; (b) cell is away from the blade. 59
4.16 Interface evolution into tail shape for $Ca = 0.1$, $\theta = \pi/6$. The history of the interface profiles are plotted starting from x_T/L=0.05 to x_T/L=0.75 with 0.1 increments. Each curve is overlaid relative to the distance of leading edge of the cell to the blade. Solid circles along ξ axis show the corresponding location of the trailing edge of the cell: $\xi = 0.0476, 0.1304, 0.2, 0.2593, 0.3103, 0.3548, 0.3939, 0.4286$, respectively. 60
4.17 Streamlines corresponding to figure 4.16, x_T/L=0.2,0.4 and 0.6. 61
4.18 Interface shape at the instant the minimum film thickness behind the tail is 0.01. Curves are for Ca=1,0.5 and 0.1. Each curve is overlaid relative to the distance of leading edge of the cell to the blade. Solid circles along ξ axis show the corresponding location of the trailing edge of the cell: $\xi = 0.0834, 0.1797, 0.4595$, respectively. 62
4.19 Comparison of interface profiles computed from the Stokes equations for $Ca = 0.025, 0.01$ and 0.005 at $t = 1.773$. 63
4.20 See caption for figure 4.19, $t = 2.368$. 64
4.21 Change of film thickness with time at (left)$x = 0.5L$ away from the blade, Ca=0.025, (right)$x = 0.6L$ away from the blade, Ca=0.005; s is the slope of the line; $\theta = \pi/6$. 64

4.22 Schematic of a cell emerging beneath the stationary blade used in the lubrication analysis of tail formation. 65
4.23 Comparison of lubrication model and the numerical solution of the Stokes problem, $Ca = 0.01$, $\theta = \pi/3$. The power series expansion uses two terms in (4.44). The bottom of the cell is at $y = 0$. 69
4.24 Geometry of meniscus printing problem 70
4.25 Comparison of the meniscus printing problem obtained from lubrication model and Stokes solution, Ca=0.001, $\theta = 5\pi/12$, (a) tip advanced $x/L = 0.2$ away from its initial position (solid line), (b) tip advanced $x/L = 0.4$ away from its initial position, (c) tip advanced $x/L = 0.8$ away from its initial position. 71
4.26 Comparison of lubrication solution of meniscus printing problem with composite expansion, $Ca = 10^{-8}$. This comparisons are made at the time when α drops to 0.00327. 72
4.27 Interface profile when the tip advances $x/x_0 = 1$ away from its initial position, $Ca = 10^{-5}$, $\theta = 5\pi/12$, (solid line) interface profile, (dashed line) corresponding pressure distribution. 73
4.28 Film shape at t'=20 with two cells, Ca=0.01, $\theta = 55^o$, $\epsilon = 0.01$, cell spacing (top) $L/2$, (bottom) L. 75
4.29 Film shape at t'=20 with three cells, Ca=0.01, $\theta = 55^o$, $\epsilon = 0.01$, cell spacing $L/4$. 76

Acknowledgments

'*...He looked across the sea and knew how alone he was now. But he could see the prisms in the deep dark water and the line stretching ahead and the strange undulation of the calm. The clouds were building up now for the trade wind and he looked ahead and saw a flight of wild ducks etching themselves against the sky over the water, then blurring, then etching again and he knew no man was ever alone on the sea...*'[1] I am grateful to my tremendous mentor, Prof. Stephen Morris, for his investments into my education and life experiences, for his time, support and perseverance throughout my journey at Berkeley. Prof. Stephen Morris has taught me how to fish, and now it is time to start eating.

I thank Prof. Andrew Szeri, Prof. Per-Olof Persson, Prof. Vivek Subramanian and his printed electronics group for the fruitful discussions and comments on the dissertation.

Finally, I could not have accomplished this journey if i did not have endless love, support and patience of my parents. There is no need to say more, but '*i love you too!*'.

[1] Ernest Hemingway, *The Old Man and the Sea*, New York: Charles Scribner's Sons, 1952, p.67.

Chapter 1

Introduction

1.1 Gravure printing and smear formation during gravure printing of electronics

Gravure printing is a transfer printing method and is suitable for low-cost, large area and high-throughput printing. Figure 1.1 shows a basic schematic of gravure printing method. A gravure roll with engraved cells (generally engraved by chemical etching) translates beneath a stationary blade. Liquid placed upstream of the blade fills the cells as they enter the gap between the blade and substrate. The objective of the blade is to wipe the excess liquid from the unengraved parts of the gravure roll leaving liquid-filled cells. The pattern defined by those cells can then be printed onto another substrate by a transfer method.

Printing by gravure method is different than coating which has been studied to coat a uniform film over a substrate (Ruschak, 1985). Coating a uniform film is a steady process. Printing, on the other hand, is inherently an unsteady process due to existence of moving boundaries, contact lines and moving interfaces; all are associated with the topographic features of the gravure roll.

Femtoliter intaglio (gravure) printing is one of the printing methods which includes transfer of ink to print electronics onto flexible substrates. A representative length scale of the method is 3–orders of magnitude smaller than the conventional gravure printing used for printing books, newspaper *etc.* In the conventional size printing, any defect smaller than $50\mu m$ cannot be recognized by human eye (Kumar, 2015). In printed electronics, on the other hand, micron–sized defects degrade the printed features at this scale. For instance, organic field-effect transistor (OFET) is an example of printed electronics. It consists of several layers to be printed and the layer patterning should be precise, except the dielectric layer. The precision of the printed source/drain electrodes layer determines the OFET's function (Kang et al., 2013). These electrodes are rectangular channels whose length and width affect the function, therefore any defect in the pattern affects the performance. Smaller channel length increases the operating speed of the transistor (Noh et al., 2007); however, as the patterns become smaller, defects become more important throughout the printing process.

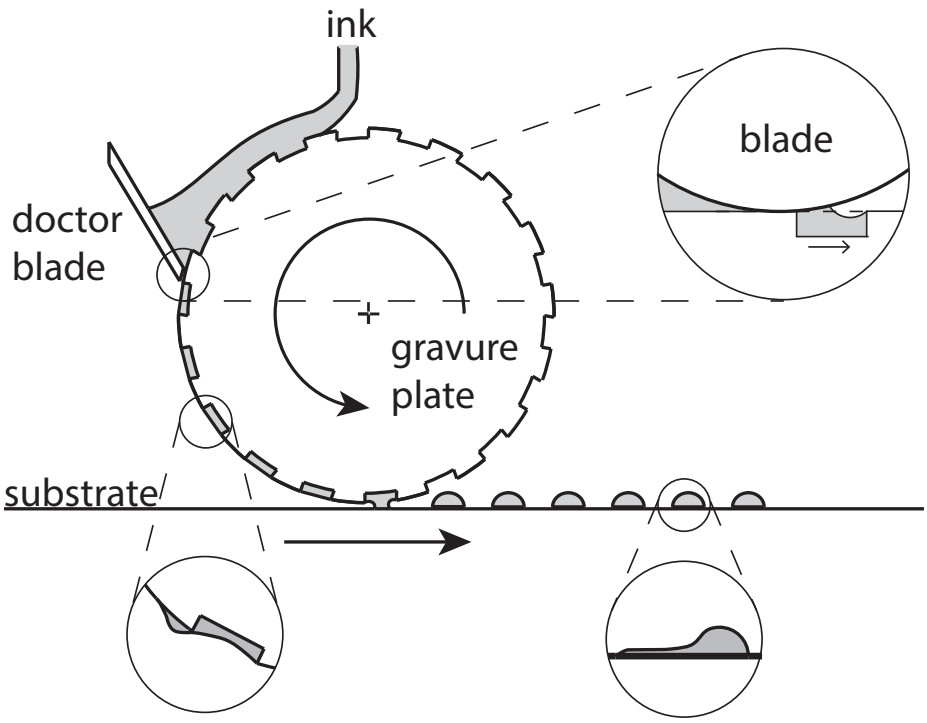

Figure 1.1: Schematic of gravure printing.

Kitsomboonloha et al. (2012) describe the deposition of femtoliter drops by the gravure method. In their experiments, the substrate (gravure plate) translates beneath a stationary blade. In plan view, engraved cells are square with edge length ranging from 1 to 10 μm; cell depth is half the edge length. Liquid placed on the substrate upstream of the blade fills the cells as they enter the gap between the blade and substrate. Motion of the substrate beneath the blade is intended to sweep excess liquid from the unengraved parts of the substrate, leaving liquid–filled cells. The pattern so defined can then be printed onto another material.

The objective is not completely attained. As each cell leaves the blade, some liquid is drawn from the cell (top magnified view in figure 1.1) and left behind as a tail on the substrate later in time (bottom left magnified view in figure 1.1) and that tail smears the printed feature (bottom right magnified view in figure 1.1).

1.2 Fluid mechanics problems during wiping and outline of the dissertation

The smear formation problem consists of two main problems to be addressed. The first problem is the growth of a meniscus due to capillarity while the cell emerges from beneath the wiper blade. The second problem is printing of that meniscus as a tail behind the cell.

Several dimensionless numbers are useful to determine the relative strength of forces in the smear formation problem. Owing to the small size of the cell, the flow is not affected by inertial and gravitational forces. Reynolds number (Re) is a dimensionless number giving the ratio of inertial forces to viscous forces and Weber number (We) is another dimensionless number giving the ratio of inertial forces to surface tension forces. Bond number (Bo) determines the strength of gravitational forces over surface tension forces. Defined by fluid density ρ, fluid dynamic viscosity η, surface tension γ, substrate speed U, characteristic cell size L and gravitational acceleration g; all three, Reynolds number ($Re = \rho UL/\eta < 10^{-6}$), Weber number ($We = \rho U^2 L/\gamma < 10^{-5}$) and Bond number ($Bo = \rho g L^2/\gamma < 10^{-8}$), are small compared with one. The flow is governed by the Stokes equations of motion which is the linearization of the Navier–Stokes equations because the inertial forces are small compared with the viscous forces. Capillary number ($Ca = \eta U/\gamma$), on the other hand, is a dimensionless number giving the strength of viscous forces over surface tension forces. Ca is used to determine the flow characteristics in printed electronics.

While the cell emerges from beneath the blade, the liquid interface meets the blade surface at a contact angle θ and it is in contact with solid surfaces and a gas (vapor). Assuming that each interface has a well–defined surface energy (defined by surface tension γ) and atomically smooth and chemically homogeneous substrates, the liquid–vapor interface may advance or stay static depending on the force balance tangent to the blade surface. By the balance of forces along the substrate direction, we can write a relation between surface tension and contact angle θ as follows:

$$\cos\theta = \frac{\gamma_{SV} - \gamma_{SL}}{\gamma_{LV}}. \tag{1.1}$$

In (1.1), γ_{SV} refers to the surface tension along the solid–vapor interface, γ_{SL} refers to the surface tension along the solid–liquid interface and γ_{LV} refers to the surface tension along the liquid–vapor interface. This equation is defined by Young (1805) and is known as 'Young condition'.

A spreading parameter S can be defined as the difference between energies per unit area of the unwetted and wetted substrates (Marangoni, 1871) by

$$S = \gamma_{SV} - (\gamma_{SL} + \gamma_{LV}). \tag{1.2}$$

If $S > 0$, liquid spreads to cover the substrate and the phenomenon is defined as '*complete wetting*'. If $S < 0$, liquid–vapor interface forms a contact angle $\theta > 0$ whose value depends on the spreading parameter S and it is defined as '*partial wetting*'. The same argument can

be made by the sign of the right hand–side of (1.1). It must lie between -1 and 1. One extreme case occurs when $\theta = 0$. When the right hand side of (1.1) is one, liquid wets the surface perfectly. When $0 < \theta < \pi/2$, the liquid wets the surface partially. When $\theta \uparrow \pi/2$, the liquid wets the surface marginally and when $\theta \geq \pi/2$ the liquid cannot spread over the surface and the liquid is defined as '*non–wetting*'.

The surface tension γ exerts a resultant force per unit area on the interface and it is given by

$$\boldsymbol{f} = \left[\nabla\gamma - \boldsymbol{n}\frac{\partial\gamma}{\partial n}\right] - \boldsymbol{n}\left(\boldsymbol{\nabla}\cdot\boldsymbol{n}\right). \tag{1.3}$$

In (1.3), $\boldsymbol{n}$ is the outward unit normal to the interface. The first term on the right hand side of (1.3) is due to variation in γ and it is tangent to the interface. This contribution is known as Marangoni traction. The second term describes the contribution due to normal component of the resultant force and this term is non–zero if the surface curvature $\boldsymbol{\nabla}\cdot\boldsymbol{n}$ is non–zero. In this study we do not treat the Marangoni traction by assuming the surface tension to be uniform along the interface.

In reality, the assumption of clean surface is not valid and this results with contact angle hysteresis. Throughout the wiping process, the contact line over the blade first advances and then retreats and the static contact angle is in between the advancing contact angle θ_A and receding contact angle θ_R due to hysteresis: $\theta_R < \theta < \theta_A$. When the contact line moves over the blade, the viscous stress near the contact line distorts the interface. Due to small size of this region, the local flow is also governed by the Stokes equations of motion. Because the viscous stress in this region scales as $\sim \eta U/r$, r being the radial distance away from the contact line, shear stress diverges as $r \to 0$. The molecular processes, however, regularizes this stress singularity. The apparent contact angle (at the macroscopic scale) differs from the static (equilibrium) contact angle. Hoffman (1975), Voinov (1976), Tanner (1979), Hocking (1983), Cox (1986) discuss the relation between the two. Moving with the advancing contact line and matching the outer meniscus to the inner viscous solution, the apparent contact line varies logarithmically with the distance to the contact line showing the viscous bending of the interface and this relation is given by

$$\theta_{ap}^3 = \theta^3 - 9Ca\,\ln\left(\frac{y}{l_i}\right). \tag{1.4}$$

In (1.4), we use y to emphasize that the contact line motion occurs over the blade; l_i is the inner length scale. In the limit as $Ca \to 0$, the difference between dynamic and static contact angles vanishes.

One way of releasing the stress singularity at the moving contact line is to allow the contact line to slip over a distance l away from the wall using the Navier–slip condition. Though, in this study, the application of the Navier–slip boundary conditions along a certain length releases the shear stress singularity, the pressure is still logarithmically divergent.

Throughout the wiping process, the contact line first advances over the blade and a meniscus grows. After the cell has emerged fully from beneath the blade, the drag introduced

by the gravure land pulls that meniscus; the contact line retreats and the meniscus is printed as a tail behind the cell extending back toward the blade. Over the range of capillary numbers (Ca, based on substrate velocity) studied by Kitsomboonloha et al. (2012), tails were always present; tail length is comparable with the cell length for Ca $O(1)$, and increases as Ca is reduced. Maximum tail width (dimension normal to substrate velocity) is comparable with cell width. As shown by Kitsomboonloha et al. (2012, figure 13), tails are manifested as smearing of printed features. Similar behavior is described by Nguyen et al. (2014) and by Secor et al. (2014).

Kitsomboonloha et al. (2012) propose that tails form owing to lateral wicking along the apparent line between the blade and substrate (when the substrate motion is in the x–direction, lateral wicking refers to wicking of liquid in the z–direction which is out of page considering figure 1.1; a cross–section in the x–y plane).

The value of the advancing contact angle determines the smear volume. For Ca fixed, it attains its maximum value for a perfectly wetting fluid. Because wicking requires liquid to wet the blade, tails could, therefore, be eliminated by making the blade non–wetting. By verifying experimentally that tails do not occur if the blade is non–wetting, Kitsomboonloha et al. (2012) demonstrate a connection between wettability and tail formation.

It can not be concluded that wicking causes tail formation, however. Owing to small size of the cell, the flow is governed by the Stokes equations of motion. For a small slope interface, when the pressure gradient along the substrate balances the shear stress and pressure across the streamlines is uniform, the Stokes equations of motion can be reduced to lubrication equations. If the blade is assumed to be perpendicular to the substrate, lubrication theory holds throughout the entire liquid film if the cell is shallow, and the contact angle θ on the blade is only slightly less than $\pi/2$. By numerically solving the evolution equation describing the unsteady film, we show that tails form in plane flow (where wicking can not occur). We conclude that tail formation is a problem in plane Stokes flow. This conclusion leads us to the mechanism being analyzed here.

To be able to integrate the Stokes equations of motion corresponding to the smear formation problem, we wrote a finite element based solver and have validated our solver by solving several Stokes problems and by making comparison of a lubrication model of smear formation problem and numerical solutions of the Stokes equations of motion for the corresponding problem. We give the details of the numerical method and validation problems in chapter 2.

As the leading edge of a liquid–filled cell emerges from beneath the blade, liquid rises on the blade to satisfy the Young condition (now, of course, with θ arbitrary). From our studies using lubrication theory, we know that the meniscus can be taken as being pinned to the leading edge of the cell. As the cell moves away from the blade, its trailing edge eventually approaches the meniscus, isolating a certain volume of liquid from the cell. This isolated meniscus is then deformed by the drag exerted by the moving substrate. As far as the quality of the printing application is concerned, we believe the solution involves minimizing the quantity of liquid drawn into the meniscus. The evolution of the isolated meniscus into a tail is, however, of considerable hydrodynamic interest. In § 3.2, we give a geometric analysis

of meniscus growth; this (hydrostatic) analysis describes the limit of vanishing Ca based on substrate speed U. The radius of curvature of the blade tip is 7.5-75 times larger than a typical cell size (Kitsomboonloha et al., 2012, Table 1). During wiping stage, the blade tip entirely fills the top of the cell acting as a lid. To avoid detail, we approximate the blade tip as horizontal to the substrate with its trailing edge face, initially, to be perpendicular to the substrate. Evidently the hydrostatic theory would be of limited interest if viscous (normal) stresses exerted by the blade caused even more liquid to be removed from the cell. In § 3.3, numerical solutions of the free boundary problem, a problem in which flow variables and the flow domain are unknown, for the Stokes equations of motion are used to show that the hydrostatic theory closely describes the process of meniscus formation if $Ca < 10^{-2}$; moreover, as Ca is increased, less liquid is removed from the cell. Because we show that hydrostatics provides an upper bound to the volume removed, the problem of controlling tail formation now reduces to the conceptually simpler problem of reducing the size of the meniscus. In § 3.4, we use the hydrostatic theory to explain why Kitsomboonloha and Subramanian (2014) were able to minimize smearing by polishing the blade to reduce its tip radius.

Tail formation extending back toward the blade occurring later in stage is also of considerable hydrodynamic interest. The meniscus drawn from the cell is printed as a tail behind the cell, and this smear formation degrades the printed features at the scale of micron size printed features. In chapter 4, we analyze the mechanism of tail formation. Meniscus drawn from the cell is separated from the cell in the limit as $Ca \to 0$, and that meniscus sitting between blade and the trailing edge of the cell is printed as a tail: the mechanism occurs between these two points, the cell is irrelevant.

This limit shows that the second fluid mechanics problem can be connected to two other real life problems. The first one is is the deposition of the tear film when we blink. Wong et al. (1996) study the deposition and thinning of the human tear film. This film covers the exposed part of the eyeball by the rise of a meniscus of the upper lid during a blink and that meniscus is used to coat the tear film. The second problem is the liquid entrainment from the meniscus of a liquid wedge during coating (Gutenev et al., 2002, Reznik et al., 2009). A film of tail shape is printed onto a horizontal substrate to be used in the deposition of micro–nano particle suspensions such as blood smears for histological analysis. The problem differs from the film drawing problem first shown by Landau and Levich (1942) because of the finite volume meniscus. As the coating film is drawn from this meniscus, the changes in the volume of the meniscus must be considered throughout the process. In the Landau-Levich problem, on the other hand, a steady film of constant thickness of $1.34rCa^{2/3}$ is coated on the substrate far from an infinite bath where r is the radius of curvature of the static meniscus forming on the bath surface. Capillary pressure gradient and substrate motion (convection) balance to produce, asymptotically, a uniform film thickness.

Though we reduce the problem to the entrainment of a film from the meniscus of liquid wedge, this reduction is valid for the limiting case of $Ca \to 0$ in the printed electronics problem. Gutenev et al. (2002) analyze the problem of film entrainment in the low capillary regime. Reznik et al. (2009) extend it to finite Ca regime using boundary integral method.

Even in the finite Ca regime, they take the contact lines both on the blade and substrate to be pinned at all times. According to our analysis in chapter 3, even for $Ca = 0.0025$, the contact line on the blade retreats due to the increased effect of drag (horizontal substrate motion). In the current problem of interest, the contact line at the trailing edge of the cell can only be taken as pinned for $Ca \to 0$, and the volume under the meniscus is not arbitrary. As Ca is increased, there is leakage from meniscus into the cell; the existence of cell should also be considered.

With this motivation, we analyze the problem in two different regimes. In the limit as $Ca \to 0$, the meniscus is separated from the cell and the problem has an inner and outer structure: in the neighborhood of pinned contact line, the viscous forces are important (inner structure); away from this inner region, viscous forces are irrelevant and this inner region connects to a bulk meniscus (outer structure). By solving the outer problem (§ 4.1), we first predict the meniscus shape in the static regime; we formulate the inner problem (§ 4.2) by making a local analysis near the tip (where the contact line is pinned at the trailing edge of the cell), and then we form the composite expansion (§ 4.3) of the inner and outer problem to show that the interface is rotated around the pinned contact line by viscosity and connects to the static bulk meniscus away from the tip. In § 4.4, we predict that the thickness of the film coated away from the bulk meniscus decreases linearly in time forming a tail shape.

By matching the outer limit of the inner problem to the inner limit of the outer problem, we form a composite expansion. A comparison of composite expansion with the Stokes solution requires Ca to be small. It is computationally expensive to solve the Stokes problem at this low Ca. The computations required for the surface force integration include a factor of Ca^{-1} and as Ca is decreased, any numerical error in the computations multiplied by Ca^{-1} and this requires the use of extremely small time step due to the explicit time step integration of the solver and this results with computationally expensive method.

In § 4.5, we solve the corresponding problem in Stokes regime for $Ca = 10^{-3}$, and show that as the angle of the interface at the tip decreases, inner viscous solution given in § 4.2 agrees with the numerical solution of the Stokes problem within a region which scales as ~ 0.1 away from the tip. In §4.6, we include the cell into the computations of the Stokes problem of tail formation.

A tail forms faster as Ca is increased. As the smear volume drawn from the cell is less for higher Ca regime, the tail length shortens. As Ca is reduced, however, the tail formation process takes longer and tail length increases with decreasing Ca first because the meniscus volume increases as Ca is reduced, as shown in chapter 3: the limit $Ca \to 0$ sets an upper bound to the smear volume, as a result tail formation takes longer; second the coated film thickness scales like $rCa^{2/3}$ as Ca gets smaller.

Solver's being computationally expensive for small Ca motivates us to model the corresponding problem in the lubrication regime. The earlier analyses are valid for arbitrary contact angles on the blade; $0 \leq \theta < \pi/2$. For small slope interface, on the other hand, lubrication theory is appropriate to analyze the tail formation mechanism.

In § 4.7, lubrication theory is used to model the tail formation problem. Comparison between the Stokes solution and lubrication model shows that, for contact angle $\theta = \pi/3$

and $Ca = 10^{-2}$, the lubrication theory closely predicts the interface evolution. Because the contact line on the blade moves freely in the lubrication model, it over–predicts the meniscus growth stage resulting with longer tail behind the cell. As θ approaches $\pi/2$ and Ca is decreased, on the other hand, the Stokes solution and lubrication model agree for the meniscus printing problem. This motivates us to analyze the smear formation mechanism by using lubrication theory for $Ca < 10^{-3}$. When Ca is $O(10^{-8})$, the slope of the linear decrease observed in the thickness of coated film computed from the numerical solution approaches the slope predicted in § 4.4. The composite expansion predicts the interface profile closely when $Ca = 10^{-8}$. We also observe the inner and outer structure; the meniscus rotates around the tip at the trailing edge of the cell by the squeeze film flow, the film of decreasing thickness connects to a thin film region of thickness $\sim rCa^{2/3}$ (Landau-Levich film) which is coated away from the static outer meniscus.

Finally, in §4.7.3, we consider the effect of a sequence of cells in the tail formation mechanism. We show that although smear formation is reduced between cells as the gap between cells is reduced, the liquid drawn from the cells accumulates under the meniscus resulting with tail formation behind the last cell in the sequence.

Chapter 2

Development and Testing of a Numerical Method for the Stokes Problem

In gravure printing of electronics, the flow is not affected by inertial and gravitational forces: the Reynolds number ($Re = \rho UL/\mu$) based on substrate length $L < 10\mu$m, substrate speed $U < 1$ mm/s and viscosity μ=29Pa.s is less than 10^{-6} and Weber number ($We = \rho UL^2/\gamma$) based on corresponding cell length, substrate speed and surface tension γ of 0.0269 N/m is less than 10^{-5}. The flow is governed by the Stokes equations of motion.

Our objective here is to analyze the smear formation problem without any complications. Because the radius of curvature r of the blade tip is large compared with a representative length scale of the cell such as its length L, we model the blade as horizontal to the substrate and its trailing edge face, at the first attempt, to be perpendicular to the substrate motion as shown in figure 2.1. We assume the blade covers the top of the cell acting as a lid and the cell is assumed to be full of liquid when it enters under the gap between the blade and the substrate. As we analyze the problem in the following chapters by using the Stokes equations of motion, in this chapter, we first formulate the corresponding Stokes problem in §2.1, and then, give the details of the numerical method to solve the free-boundary problem in §2.2 and validate the solver in §2.3.

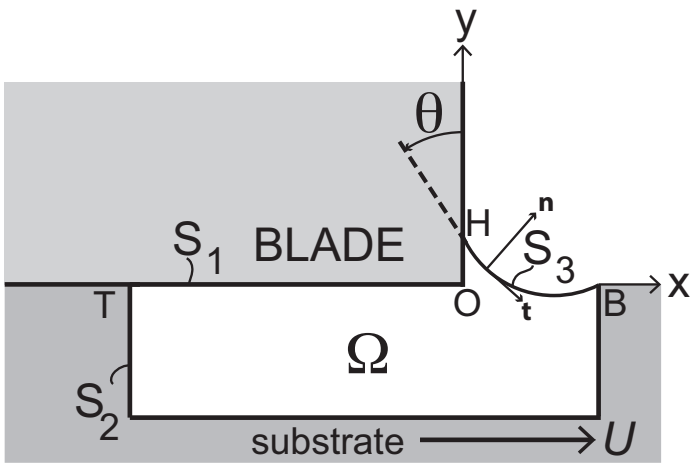

Figure 2.1: Flow domain Ω for the Stokes problem of smearing: S_1, wiper blade; S_2, cell boundary; S_3, free surface. Coordinate axis is fixed on wiper blade which is stationary, cell translates with velocity $U\boldsymbol{i}$. T is the trailing edge, B is the leading edge of the cell and the contact line is at H. The aspect ratio of the cell is set to $L/d = 2$ where L is the length of the cell, d is the depth of the cell.

2.1 Problem formulation

The flow domain is shown in figure 2.1: the coordinate is fixed on the exit of the stationary blade; x-axis lies along the substrate, y-axis along the wiper blade. Nondimensionalized by the cell length L, substrate speed U and pressure $\mu U/L$, non–dimensional stress field is divergenceless:

$$\boldsymbol{\nabla} \cdot \boldsymbol{\sigma} = 0 \quad \text{in} \quad \Omega \tag{2.1}$$

where the dimensionless Newtonian stress tensor is defined by

$$\boldsymbol{\sigma} = -p\boldsymbol{I} + \left(\boldsymbol{\nabla u} + \boldsymbol{\nabla u}^T\right). \tag{2.2}$$

In (2.2), p is the dimensionless pressure and $\boldsymbol{u}$ is the dimensionless velocity field. The continuity equation requires that velocity field is divergenceless:

$$\boldsymbol{\nabla} \cdot \boldsymbol{u} = 0. \tag{2.3}$$

The boundary of the domain Ω is $S = S_1 \cup S_2 \cup S_3$ where S_1 is the wiper blade surface, S_2 is the moving cell boundary, S_3 is the free surface which is unknown *a priori*. On the wiper blade surface and cell boundary; no-slip, no penetration boundary conditions are applied, except where the free surface and trailing edge of the cell meets the wiper blade:

$$\boldsymbol{u} = \boldsymbol{0} \quad \text{on} \quad S_1, \tag{2.4a}$$

$$\boldsymbol{u} = \boldsymbol{i} \quad \text{on} \quad S_2. \tag{2.4b}$$

On the interface the normal $\boldsymbol{n}$ is the outward pointing unit normal vector, and the corresponding unit tangent vector $\boldsymbol{t}$ along the interface is given by $\boldsymbol{t} = \boldsymbol{k} \times \boldsymbol{n}$ ($\boldsymbol{k}$ is the unit normal in z-direction which is out of page). Free surface boundary conditions are obtained by balance of interfacial mass and momentum. Neglecting the traction on the interface due to outside fluid (*e.g.* low viscosity gas) and neglecting the Marangoni traction, there is only normal component of the stress on the interface which is given by

$$\boldsymbol{n} \cdot (\boldsymbol{\sigma} \cdot \boldsymbol{n}) = -\frac{1}{Ca} \boldsymbol{\nabla} \cdot \boldsymbol{n}. \tag{2.5}$$

In (2.5), Ca is defined by $Ca = \mu U/\gamma$ which is a dimensionless number showing the strength of viscous forces over surface tension forces. The contact line where the free surface meets the wiper blade is free to move (Point H in figure 2.1). The stress singularity at the contact line is released by applying the Navier-slip condition (Silliman and Scriven, 1978) given by

$$\boldsymbol{t}_{wiper} \cdot (\boldsymbol{\sigma} \cdot \boldsymbol{n}_{wiper}) = \frac{1}{s} \boldsymbol{t}_{wiper} \cdot (\boldsymbol{u}_{slip} - \boldsymbol{u}_{wiper}) \tag{2.6}$$

where s is the dimensionless slip coefficient with $s \to 0$ recovering no-slip, $s \to \infty$ recovering perfect–slip conditions.

We assume that the contact line is pinned at the leading edge of the cell and the moving contact line at H meets the blade at Young angle:

$$\boldsymbol{t}_{interface} \cdot \boldsymbol{t}_{wiper} = \cos\theta. \tag{2.7}$$

If there is an effect of dynamic contact angle, it will emerge from the solution. We use the static solution given in § 3.2 for the free surface profile when the leading edge of the cell (point B in figure 2.1) has emerged $0.1d$ from the wiper blade as initial condition.

2.2 Numerical method

To integrate the initial boundary value problem given in § 2.1, we wrote a finite element method (FEM) based solver for the Stokes equations of motion on unstructured triangular meshes. In this section, we first give the variational formulation of the Stokes problem (Johnson, 2009, p. 232), and then discretize the governing equations and finally give the details of the time integration.

2.2.1 Galerkin formulation

A Galerkin formulation is obtained first by multiplying the Stokes equations of motion with the virtual velocities $\bar{u}, \bar{v}$ and virtual pressure $\bar{p}$ (Johnson, 2009, p. 232). Virtual velocity components and pressure are functions (test functions) chosen from the spaces V and H, respectively, defined by

$$V = \left[H_o^1(\Omega)\right]^2 = \left\{ \bar{u}_i = (\bar{u}, \bar{v}) : \bar{u}_i \in H_0^1(\Omega), i = 1, 2 \right\},$$

$$H = \left\{ \bar{p} \in L_2(\Omega) : \int_\Omega \bar{p} dx \equiv 0 \right\}.$$

Here, $H_0^1\Omega$ and $L_2(\Omega)$ are Hilbert spaces (Johnson, 2009, p. 33, p. 232). After multiplying the Stokes equation by the virtual velocities and pressure, we integrate over the domain Ω to obtain:

$$\int_\Omega \frac{\partial \sigma_{ij}}{\partial x_j} \bar{u}_i d\Omega = 0, \tag{2.8}$$

$$\int_\Omega \frac{\partial u_i}{\partial x_i} \bar{p} d\Omega = 0. \tag{2.9}$$

In (2.8), $\bar{u}_i$ is not a vector and summation over i is not implied; it is the corresponding virtual velocity component: for the x–component of (2.8) it refers to $\bar{u}$ and for the y–component of (2.8) it refers to $\bar{v}$. We apply divergence theorem on the diffusion term:

$$\int_\Omega \left(\frac{\partial \sigma_{ij} \bar{u}_i}{\partial x_j} - \sigma_{ij} \frac{\partial \bar{u}_i}{\partial x_j} \right) d\Omega = - \int_\Omega \sigma_{ij} \frac{\partial \bar{u}_i}{\partial x_j} d\Omega + \int_S \bar{u}_i \sigma_{ij} n_j dS = 0, \tag{2.10}$$

and we use the interfacial boundary condition (2.5) along S_3 to obtain

$$\int_\Omega \sigma_{ij} \frac{\partial \bar{u}_i}{\partial x_j} d\Omega = - \int_{S_3} \frac{1}{Ca} \bar{u}_i n_i \frac{\partial n_j}{\partial x_j} dS + \int_{S_1 \cup S_2} \bar{u}_i \sigma_{ij} n_j dS. \tag{2.11}$$

We evaluate the surface integral in (2.11) by using integration by parts (Ruschak, 1980). To do so, we rewrite the surface integral in vectorial notation:

$$\int_{S_3} \frac{1}{Ca} \bar{u}_i \left(\boldsymbol{\nabla} \cdot \boldsymbol{n} \right) \boldsymbol{n} dS = \int_{S_3} \frac{1}{Ca} \bar{u}_i \frac{d\boldsymbol{t}}{ds} ds \tag{2.12}$$

where $\boldsymbol{t}$ is the unit tangent vector in the increasing s direction. Integrating by parts, we obtain:

$$\int_{S_3} \frac{1}{Ca} \bar{u}_i \frac{d\boldsymbol{t}}{ds} ds = \left[\frac{1}{Ca} \bar{u}_i \boldsymbol{t} \right]_H^B - \int_H^B \frac{1}{Ca} \boldsymbol{t} \frac{d\bar{u}_i}{ds} ds, \tag{2.13}$$

where H and B are the positions of the contact lines on the solid boundaries as shown in figure 2.1. As the model problem lies in the plane, we rewrite x and y components of the momentum equation using the stress tensor definition given in (2.2):

$$x : \int_\Omega -p \frac{\partial \bar{u}}{\partial x} d\Omega + \int_\Omega 2 \frac{\partial \bar{u}}{\partial x} \frac{\partial u}{\partial x} d\Omega + \int_\Omega \frac{\partial \bar{u}}{\partial y} \frac{\partial u}{\partial y} + \int_\Omega \frac{\partial \bar{u}}{\partial y} \frac{\partial v}{\partial x} d\Omega + \left[\frac{1}{Ca} \bar{u} t_x \right]_H^B - \int_H^B \frac{1}{Ca} t_x \frac{d\bar{u}}{ds} ds = 0, \tag{2.14}$$

$$y : \int_\Omega -p \frac{\partial \bar{v}}{\partial y} d\Omega + \int_\Omega 2 \frac{\partial \bar{v}}{\partial y} \frac{\partial v}{\partial y} d\Omega + \int_\Omega \frac{\partial \bar{v}}{\partial x} \frac{\partial v}{\partial x} + \int_\Omega \frac{\partial \bar{v}}{\partial x} \frac{\partial u}{\partial y} d\Omega + \left[\frac{1}{Ca} \bar{v} t_y \right]_H^B - \int_H^B \frac{1}{Ca} t_y \frac{d\bar{v}}{ds} ds = 0, \tag{2.15}$$

and the continuity equation:

$$\int_\Omega \left(\frac{\partial u}{\partial x} + \frac{\partial v}{\partial y} \right) \bar{p} d\Omega = 0. \tag{2.16}$$

At the moving contact line, t_x and t_y are computed by the use of (2.7) to set the contact angle. We should note that the last term in (2.11) is zero when Dirichlet boundary condition is applied along the boundary because the virtual velocities are set to zero at corresponding nodes. However, when we apply the slip boundary condition along the distance l, we add that integral to the corresponding x, y component of the equation (2.14),(2.15) with the use of slip boundary condition. In the model geometry shown in figure 2.1, this occurs at the free surface and blade intersection (point H), and at the intersection of blade and trailing edge of the cell (point T) and blade and substrate intersection (point O) after the cell emerges fully from beneath the blade. With the use of (2.6), we add these two surface integrals to (2.14) and (2.15), respectively:

$$x : + \int_{S_1(slip)} \frac{1}{s} \bar{u} u dS, \tag{2.17}$$

$$y : + \int_{S_1(slip)} \frac{1}{s} \bar{v} v dS. \tag{2.18}$$

This ends the Galerkin formulation of the problem.

2.2.2 Discretization

We use $P2 - P1$ isoparametric triangular elements (Bathe, 1996, figure 5.11) for the solution variables: Figure 2.2 shows a representative element in the isoparametric domain with the numbers of the nodes. The velocity components are represented by the values at the six nodes per element (1 to 6 in figure 2.2) and interpolated using quadratic polynomials ($P2$ element), pressure is represented by the three corner nodes (1 to 3 in figure 2.2) and interpolated using linear polynomial ($P1$ element). This choice of element satisfies the Ladyzhenskaya-Babushka-Brezzi stability condition (Johnson, 2009, p. 232).

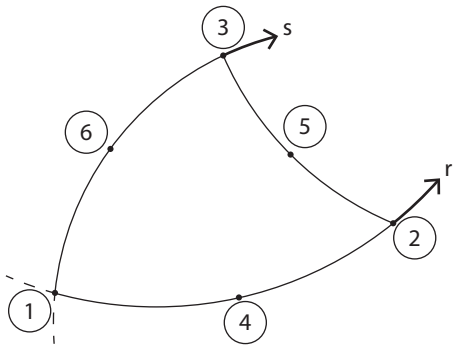

Figure 2.2: Nodal points in the isoparametric plane: 1 to 6 is used for $P2$ element, 1 to 3 is used for $P1$ element.

The quadratic interpolation for the velocity components are defined as follows (with r and s defined in figure 2.2):

$$h_1^q(r,s) = 1 - 3r - 3s + 2r^2 + 4rs + 2s^2, \tag{2.19a}$$

$$h_2^q(r,s) = -r + 2r^2, \tag{2.19b}$$

$$h_3^q(r,s) = -s + 2s^2, \tag{2.19c}$$

$$h_4^q(r,s) = 4r - 4rs - 4r^2, \tag{2.19d}$$

$$h_5^q(r,s) = 4rs, \tag{2.19e}$$

$$h_6^q(r,s) = 4s - 4rs - 4s^2. \tag{2.19f}$$

Similarly, the linear functions used for the pressure are given by

$$h_1^l(r,s) = 1 - r - s, \tag{2.20a}$$

$$h_2^l(r,s) = r, \tag{2.20b}$$

$$h_3^l(r,s) = s. \tag{2.20c}$$

We approximate the velocity components and pressure in the isoparametric plane as follows:

$$u(r,s) = \sum_{i=1}^{6} h_i^q u_i, \tag{2.21}$$

$$v(r,s) = \sum_{i=1}^{6} h_i^q v_i, \tag{2.22}$$

$$p(r,s) = \sum_{i=1}^{3} h_i^l p_i. \tag{2.23}$$

Here h_i^q, h_i^l are quadratic and linear interpolations; u_i, v_i and p_i are the corresponding nodal values. Subscripts denote the nodal points shown in figure 2.2.
The unit tangent vector in the xOy is computed by

$$\boldsymbol{t} = \frac{\sum_{i=1}^{3} s_i \frac{dh_i^q}{ds}}{\left\| \sum_{i=1}^{3} s_i \frac{dh_i^q}{ds} \right\|} \tag{2.24}$$

with s_i being nodal position vector and dh_i^q/ds being scalar corresponding to the element edge over which the computation is carried out. The normal component is found simply by $\boldsymbol{n} = \boldsymbol{k} \times \boldsymbol{t}$.

The coordinates are interpolated with the quadratic interpolation functions:

$$x(r,s) = \sum_{i=1}^{6} h_i^q x_i, \tag{2.25}$$

$$y(r,s) = \sum_{i=1}^{6} h_i^q y_i, \tag{2.26}$$

where x_i and y_i are the coordinates of the node points in the element and h_i^q is defined in (2.19). Because the computations are performed in the isoparametric domain, we need to express the mapping for the derivatives from the xOy plane to the isoparametric plane, which is given by

$$\begin{bmatrix} \frac{\partial}{\partial x} \\ \\ \frac{\partial}{\partial y} \end{bmatrix} = J^{-1} \begin{bmatrix} \frac{\partial}{\partial r} \\ \\ \frac{\partial}{\partial s} \end{bmatrix}. \tag{2.27}$$

Jacobian (J) of the transformation in (2.27) is given by

$$J = \begin{bmatrix} \frac{\partial x}{\partial r} & \frac{\partial y}{\partial r} \\ \\ \frac{\partial x}{\partial s} & \frac{\partial y}{\partial s} \end{bmatrix}. \tag{2.28}$$

We use Gauss quadrature to carry out the integrations. Plane integrations are evaluated over triangles using 7–point Gauss integration rule (Bathe, 1996, §5.5.4 and 5.5.5). r and s are evaluated at the Gauss points of integration over triangles. Boundary integrals are evaluated using 3–point Gauss integration rule (Bathe, 1996, §5.5.3). In both cases, the Gauss quadrature integrates exactly polynomials of order at most 5. The highest order polynomial in the integrations is 4, therefore the integrations are exact throughout the numerical method.

After forming the element matrix $\boldsymbol{A}^k$ and right hand side vector $\boldsymbol{R}^k$ over each element e^k for the unknowns by using (2.14) to (2.16), we form a global stiffness matrix $\boldsymbol{A}$, and right hand side vector $\boldsymbol{R}$. We impose constraints on certain solution variables with the use of Lagrange multiplier method: we extend the solution vector by adding the Lagrange multipliers λ for the constraints and extending the system of equations to

$$\begin{bmatrix} \boldsymbol{A} & \boldsymbol{n}_i^T \\ \\ \boldsymbol{n}_i & 0 \end{bmatrix} \begin{bmatrix} \boldsymbol{u} \\ \\ \lambda \end{bmatrix} = \begin{bmatrix} \boldsymbol{R} \\ \\ u_i^* \end{bmatrix} \tag{2.29}$$

where $\boldsymbol{n}_i$ is a vector with all entries equal to zero, but its ith entry which is equal to 1, u_i^* is the imposed constraint at node i. The unstructured mesh is generated using the methods explained by Persson (2004), Persson and Strang (2004).

2.2.3 Time integration

The Stokes equations are quasi-steady, it is the moving boundaries that introduce time dependence.

Mass conservation along the interface requires that no fluid can cross it and the condition is given by the kinematic boundary condition:

$$\boldsymbol{n} \cdot (\boldsymbol{u} - \dot{\boldsymbol{s}}) = 0, \tag{2.30}$$

where $\dot{\boldsymbol{s}}$ is the velocity of a material point along the free surface.

Time integration is performed explicitly: at time t, the linear Stokes problem is solved using the boundaries determined at the previous time $t - \Delta t$; boundaries are then displaced in the normal direction to the interface using the velocity field from the same time $t - \Delta t$. Because this method is explicit, we restrict the magnitude of Δt using a Courant condition: $\Delta t < c\Delta x/u$ where Δx is the minimum edge length in the mesh and u is the maximum velocity. We take $c < 1/4$. To maintain resolution, the quality of the mesh was checked regularly to refine the mesh; between refinements, the mesh was simply displaced from one

time step to the next using the local fluid velocity. The mesh is dynamic so the number of elements varies throughout the integration. Generally, we use approximately 1000 elements distributed non-uniformly over the domain. During mesh movement and remeshing, the mass of liquid must remain constant in the model problem for smear formation. In the corresponding computations, mass is conserved to within an error of 0.01%.

2.3 Validation of the solver

Before solving model problem for smear formation in chapters 3 and 4, the method was tested against problems in plane Stokes flow having explicit solutions: biharmonic problems such as flow through a slit (Green, 1944), the problem of over–damped capillary-wave, and stick–slip problem (Richardson, 1970) describing a free jet emerging from a slit in a thick wall. Apart form these problems, we also compare the numerical solution of the Stokes equations of motion for the smear formation problem with the corresponding lubrication model in chapter 4.

2.3.1 Flow through a slit

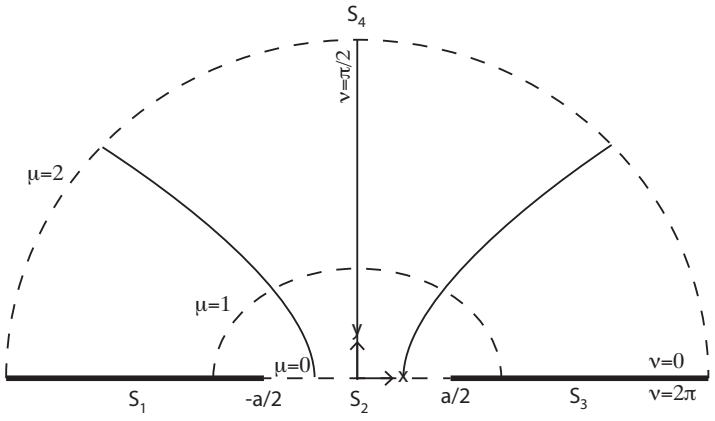

Figure 2.3: Geometry for the flow through a slit.

We consider the Stokes flow through a slit of width a in an infinite plane. Figure 2.3 shows the problem domain; the coordinate axis is fixed at the middle of slit. The incoming flow in the positive y–direction with flow rate Q at the slit is given by

$$v_y = \frac{4Q}{\pi a}\left\{1 - \left(\frac{2x}{a}\right)^2\right\}^{1/2}. \tag{2.31}$$

The boundary conditions at the edges of the slit (S_1 and S_3) are no-slip and no penetration boundary conditions. Far away from the slit, the pressure drops to zero.

According Green (1944), solution to the boundary value problem is that the streamlines are hyperbolas with foci at $x = \pm 1/2a$. We first introduce the elliptic cylindrical coordinates (μ, ν) that we have used. Note that in this subsection (μ, ν) are unrelated to viscosity. The curve μ=const. is the ellipse

$$\frac{x^2}{a^2 \cosh^2 \mu} + \frac{y^2}{a^2 \sinh^2 \mu} = \frac{1}{4}. \tag{2.32}$$

The curve ν=const. is the hyperbola

$$\frac{x^2}{a^2 \cos^2 \nu} - \frac{y^2}{a^2 \sin^2 \nu} = \frac{1}{4}. \tag{2.33}$$

The mapping from elliptic coordinates to Cartesian coordinates is given by

$$x = \frac{a}{2} \cosh\mu \, \cos\nu, \tag{2.34a}$$

$$y = \frac{a}{2} \sinh\mu \, \sin\nu. \tag{2.34b}$$

We use the mapping (2.34a,b) in the numerical solution because the solver is written in Cartesian coordinates. According to Green (1944), the velocity filed is given by

$$v_\mu = \frac{4Q}{\pi a} \frac{\sin^2 \nu}{\left(\sinh^2 \mu + \sin^2 \nu\right)^{1/2}}, v_\nu = 0, \tag{2.35}$$

and the pressure distribution is given by

$$p = \frac{8\eta Q}{\pi a^2} \left(2 - \frac{\sinh 2\mu}{\sinh^2 \mu + \sin^2 \nu} \right), \tag{2.36}$$

where η is the dynamic viscosity, Q is the flow rate through the slit. Note that $p \to 0$ as $\mu \to \infty$. As shown in figure 2.3, through the slit, $\mu = 0$ and ν varies between 0 and π.

We solve the corresponding Stokes problem on the domain shown in figure 2.3. For the outer boundary S_4 we choose the ellipse with $\mu = 2$: on this surface we impose as boundary conditions the velocity and pressure given by the exact solution (2.35), (2.36), by setting $a = 1$ and $\mu = 2$. On the slit (S_2), vertical velocity is set to (2.31) and $u = 0$ and we apply no–slip, no penetration boundary conditions on the walls (S_1 and S_3). We use 2300 triangular elements.

Figure 2.4 compares the velocity and pressure distribution at $x = 0$. The numerical solution and exact solution agree. In figure 2.5, we also plot the streamlines from our numerical solution and they overlie the streamlines from the exact solution.

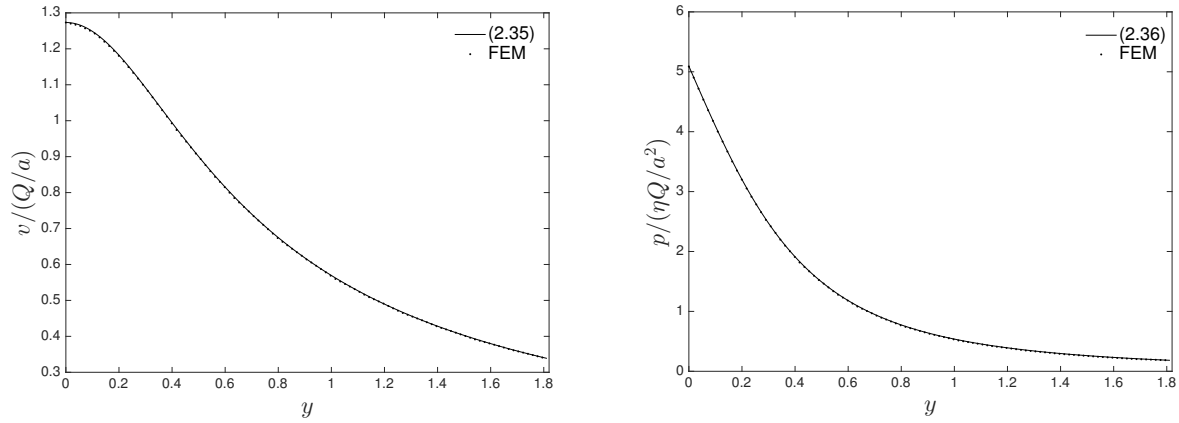

(a) v-velocity (b) pressure

Figure 2.4: Comparison of the numerical solution of the Stokes problem with exact solution of flow through a slit at $x = 0$.

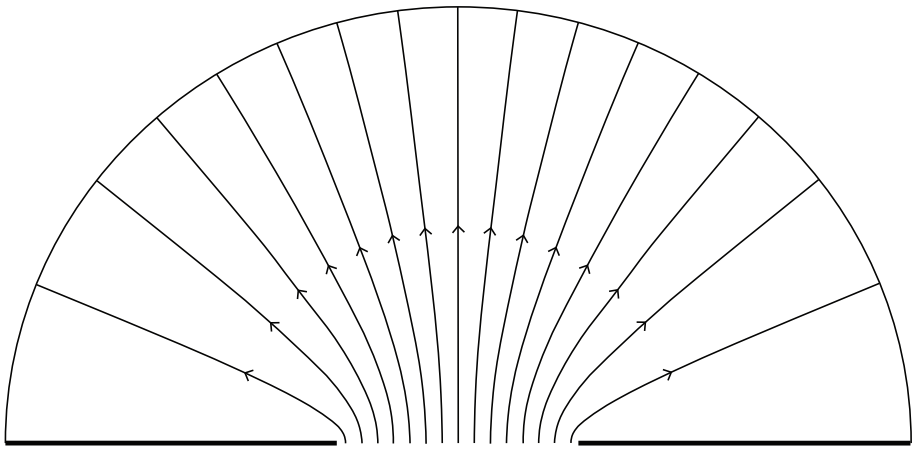

Figure 2.5: Streamlines of the flow through a slit, corresponding to figure 2.3.

2.3.2 Overdamped capillary wave problem

A capillary wave problem allows us to check the mesh movement algorithm in the solver. Lamb (1975, p.625–627) gives the decay of viscous water–waves by taking the effect of inertia and surface tension into account. In the limit density $\rho \to 0$, the flow is governed by the Stokes equations of motion, and we recover the solution of the overdamped capillary wave problem. To do so, we expand Lamb's solution into first order in ρ, keep the coefficients of ρ and then cancel ρ's. The coordinate is fixed on the unperturbed interface at $y = 0$ with y decreasing downwards. When a flat interface at $y = 0$ is perturbed from its base state in which there is no motion in the fluid, the flow decays with a dispersion relation $n = -\gamma k/(2\eta)$. Here, γ is the surface tension, k is the wave number which is given by

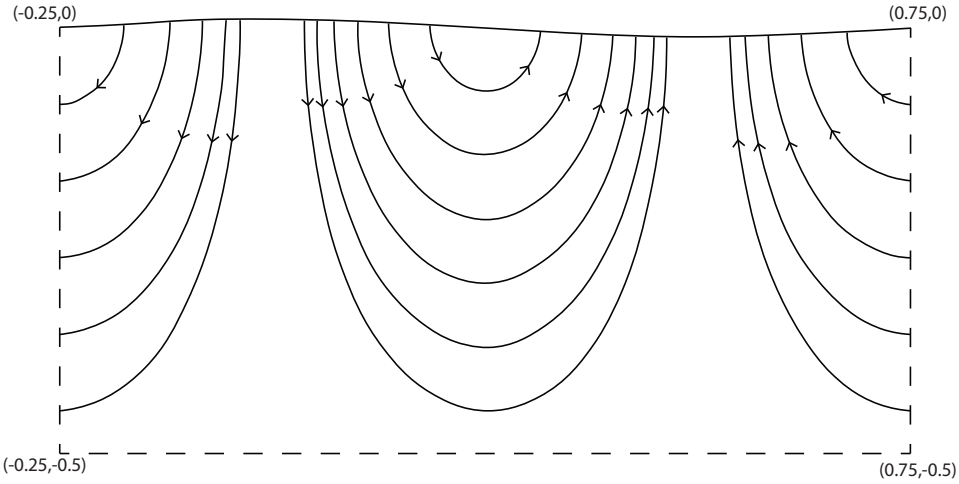

Figure 2.6: Overdamped capillary wave problem: solution domain; streamlines are obtained from the numerical solution corresponding to the interface perturbed with amplitude a=0.01 at $t = 0$.

$k = 2\pi/\lambda$ with λ being the wavelength of the perturbation and η is the dynamic viscosity. Because $n \propto k$, the short waves are removed first; the opposite is true for viscous gravity waves as $n \propto 1/k$. Note that in this subsection k is unrelated to a unit vector.

The position of the free surface ζ is defined from $y = 0$, and the interface profile is given by

$$\zeta(x,t) = Ae^{\mathrm{i}kx+nt}, \tag{2.37}$$

where A is the amplitude of the wave. The velocity field is found to be

$$u(x,y,t) = \frac{\gamma}{2\eta}\mathrm{i}k^2Aye^{ky}e^{\mathrm{i}kx+nt}, \tag{2.38}$$

$$v(x,y,t) = \frac{\gamma}{2\eta}kA\left(-1+ky\right)e^{ky}e^{\mathrm{i}kx+nt}. \tag{2.39}$$

Integrating the momentum equations, pressure distribution is found to be

$$p(x,y,t) = \gamma k^2 Ae^{ky}e^{ikx+nt}. \tag{2.40}$$

We non-dimensionalize the equations using the scales $l_s = \lambda$, $u_s = \gamma/\eta$, $p_s = \gamma/\lambda$, $t_s = \lambda\eta/\gamma$. For the following, all variables are dimensionless. We take A to be real and the perturbation solution as the real part of the solution with $a = A/\lambda$, then the dimensionless interface profile is given by

$$\zeta(x,t) = a\cos(2\pi x)e^{-\pi t}, \tag{2.41}$$

and the dimensioneless velocity components are given by

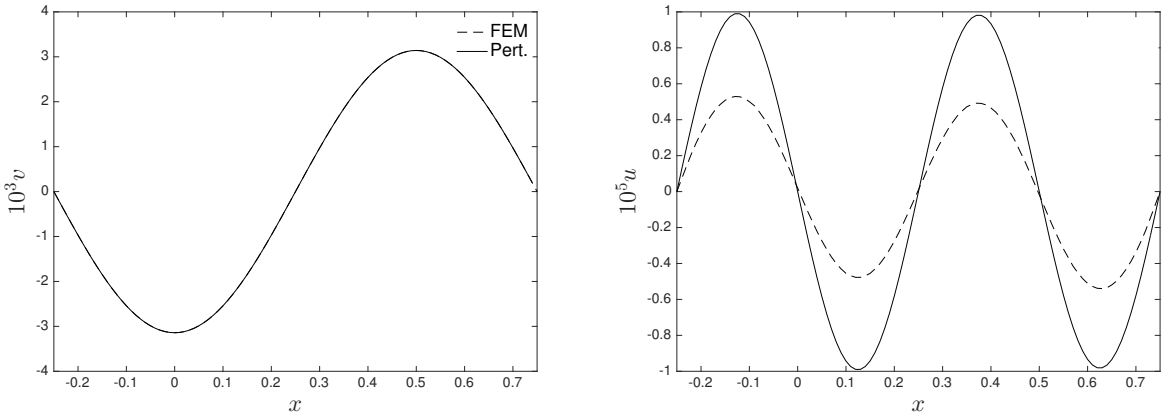

(a) v-velocity (b) u-velocity

Figure 2.7: Comparison of numerical solution of the Stokes problem with the exact solution of overdamped capillary–wave problem: (a) v–velocity on free surface at $t = 0$, 2–norm of the difference is 3.0525e-6, (b) Comparison of the Stokes solution and perturbation solution: u–velocity on free surface at $t = 0$, 2–norm of the difference is 2.3769e-05. See text for the discussion on the discrepancy in u-velocity and the definition of the 2–norm is given in (2.35).

$$u(x, y, t) = -2\pi^2 a y e^{2\pi y} \sin(2\pi x) e^{-\pi t}, \tag{2.42}$$

$$v(x, y, t) = \pi a(-1 + 2\pi y) e^{2\pi y} \cos(2\pi x) e^{-\pi t}. \tag{2.43}$$

The corresponding dimensionless pressure distribution is given by

$$p(x, y, t) = 4\pi^2 a e^{2\pi y} \cos(2\pi x) e^{-\pi t}. \tag{2.44}$$

To test the solver, we use the problem domain shown in figure 2.6. We set the wavelength to unity and depth to 0.5. We use non–uniform mesh with finer mesh close to the free surface with a total of 994 triangular elements. We set the velocity distribution along the boundary except the free surface from the perturbation solution as boundary condition. Initially, for a small amplitude perturbation, we set a to 10^{-3}. In figure 2.7a,b we compare, on the free surface, the v and u–velocities respectively. The two norm of the error (defined in (2.45)) is order 10^{-5}. The discrepancy observed in the u–velocity, although the solution predicts the correct wave pattern, is due to the perturbation analysis in which zero shear stress condition is applied at y=0. A rough computation of the shear stress from the perturbation solution at the interface gives that shear is of order 10^{-4} for the maximum amplitude. Therefore, any error of order 10^{-4} or smaller in the resulting solution is expected.

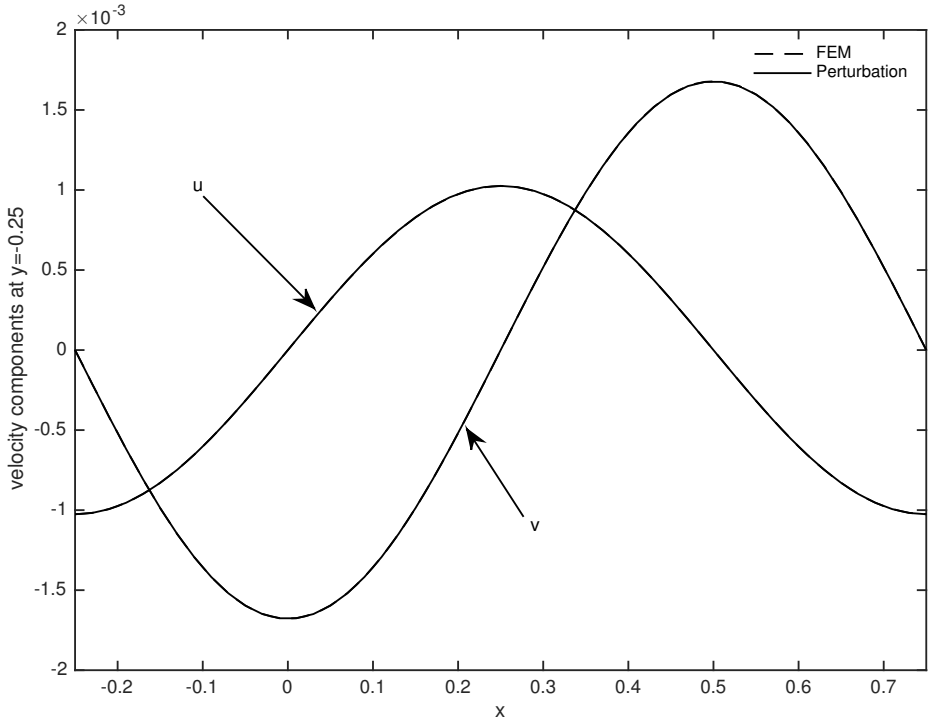

Figure 2.8: Comparison of the numerical solution of the Stokes problem and perturbation solution of the overdamped capillary–wave problem: x and y–velocity at the mid of the domain at $t = 0$; 2-norm of the difference in u is 1.0259e-5 and in v is 1.1537e-05.

We also compare the solutions at the middle of the domain, y=-.25 in figure 2.8 which shows good agreement with the perturbation solution.

We now increase the amplitude of the perturbation 10 times and check the time evolution by plotting the free surface profiles at various times for $a = 10^{-2}$ and compare with the perturbation solution in figure 2.9, plot the pressure distribution in figure 2.10. All results agree with the perturbation solution.

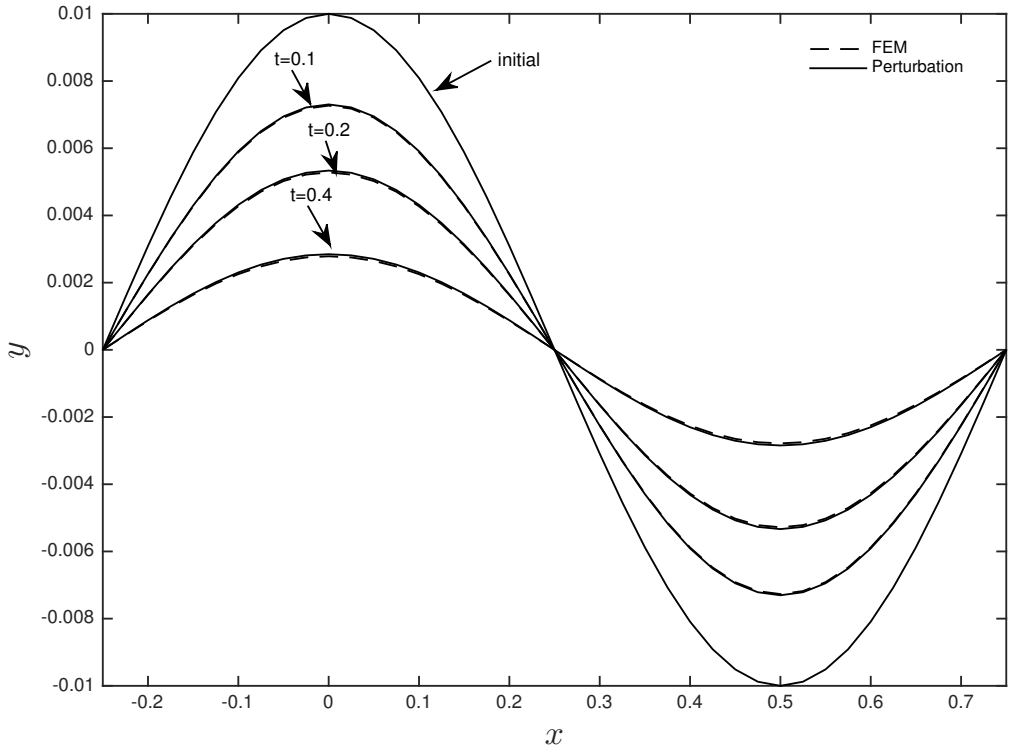

Figure 2.9: Comparison of the numerical solution of the Stokes problem and perturbation solution of the overdamped capillary–wave problem: evolution of the interface.

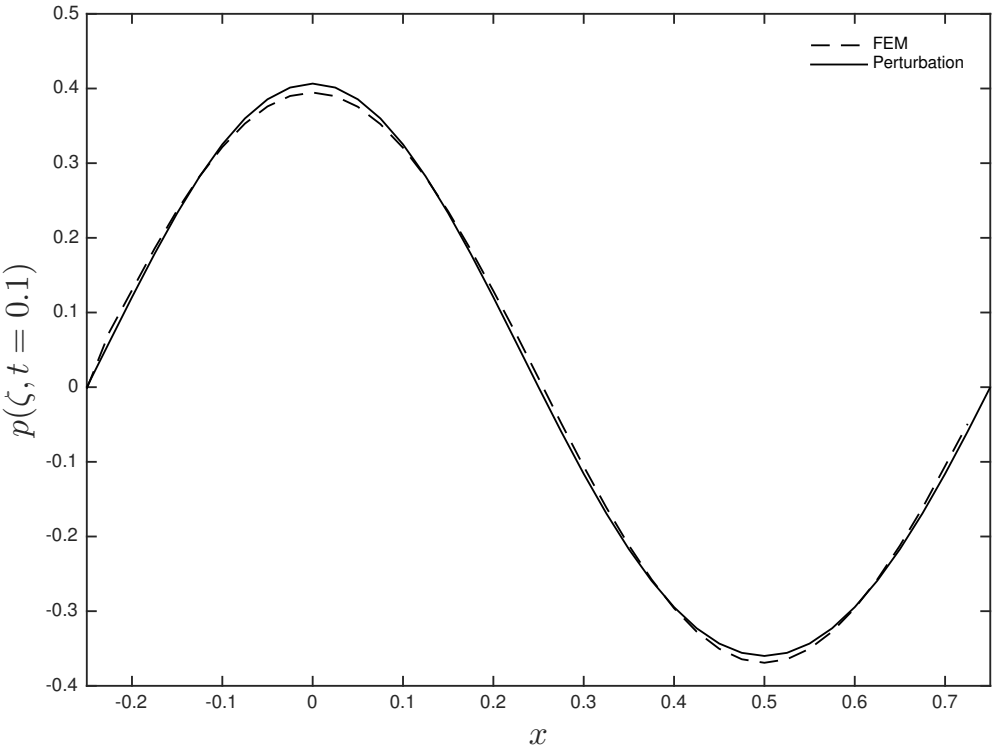

Figure 2.10: Comparison of the numerical solution of the Stokes problem and perturbation solution of the overdamped capillary–wave problem: pressure on interface at $t = 0.1$.

2.3.3 Stick–slip problem

Richardson (1970) gives the exact solution of the stick–slip problem which is a flow of a Newtonian fluid emerging between parallel plates in plane. The problem includes a stress singularity at the exit of the top plate (x=0,y=1) as shown in figure 2.11. The singularity arises from the change from a no-slip boundary condition to a perfect slip boundary condition. The velocity around the singularity varies like $r^{1/2}$, r being the radial distance from the singular point, therefore the stress varies like $\sim r^{-1/2}$.

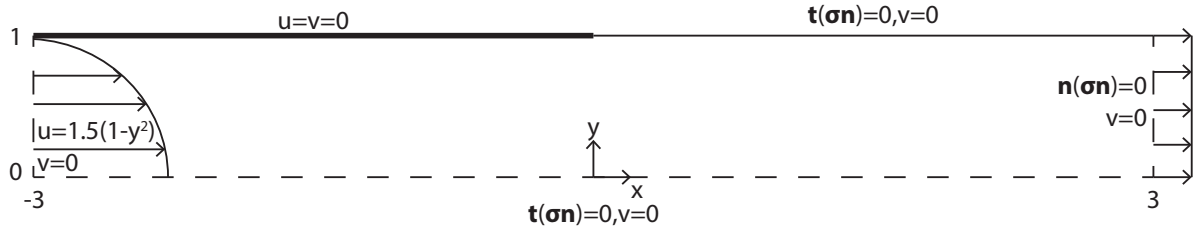

Figure 2.11: Stick–slip problem domain.

Though we do not resolve singularity there, by solving this problem, we show that our solver predicts the velocity distribution on the free surface correctly.

The free surface for $x > 0$ is replaced by a plane on which the shear stress vanishes. We solve the problem for the half domain; symmetry boundary conditions are imposed on the centerline. At the inlet, parabolic velocity profile; at the outlet plug flow are imposed. For $x < 0, y = 1$ no–slip, no penetration; for $x > 0, y = 1$ slip boundary conditions are imposed. Figure 2.12 compares the centerline and slip plane velocity with Richardson solution. Figure 2.13 shows comparison of the centerline pressure as well.

Lastly, we show the convergence of the method for two different error definitions: L_2 and L_∞ norm errors. L_2 norm of a vector $\boldsymbol{u}$ is defined by

$$||\boldsymbol{u}||_2 = \sqrt{\sum_i |u_i|^2}, \tag{2.45}$$

and L_∞ norm of a vector $\boldsymbol{u}$ is defined by

$$||\boldsymbol{u}||_\infty = \max\left(|u_i|\right). \tag{2.46}$$

We note that $\boldsymbol{u}$ in (2.45) and (2.46) is unrelates to the velocity field. The convergence of the method is shown in figure 2.14. With h being the largest edge of the element, the errors in u and in p scale respectively as h^3 and h^2. This is expected because pressure is interpolated using a polynomial with one degree less than the velocity integration polynomial.

After validating the Stokes solver, we use it to analyze the smear formation problem in Chapters 3 and 4.

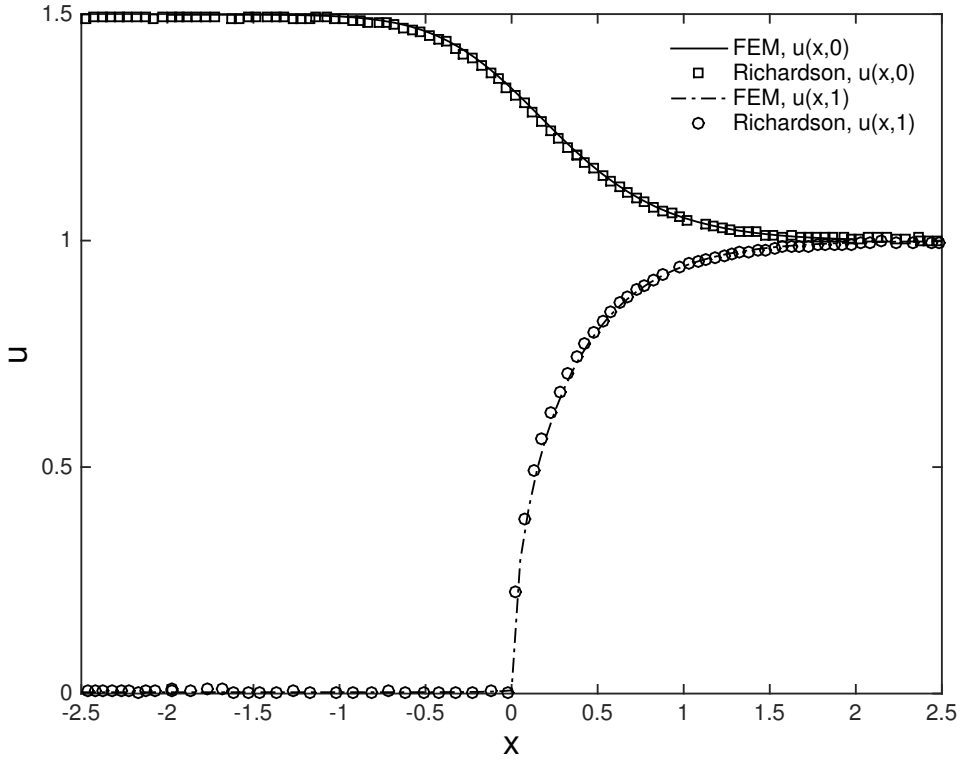

Figure 2.12: Comparison of the numerical solution of the Stokes problem and Richardson solution for stick–slip problem: centerline and slip plane u-velocity.

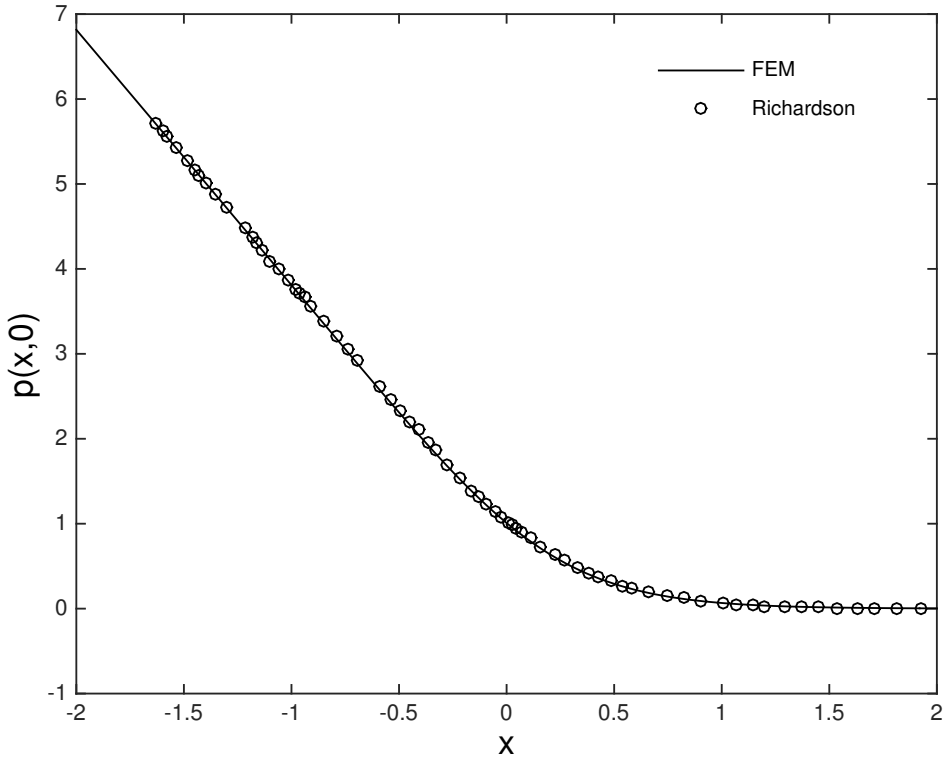

Figure 2.13: Comparison of the numerical solution of the Stokes problem and Richardson solution for stick–slip problem: centerline pressure.

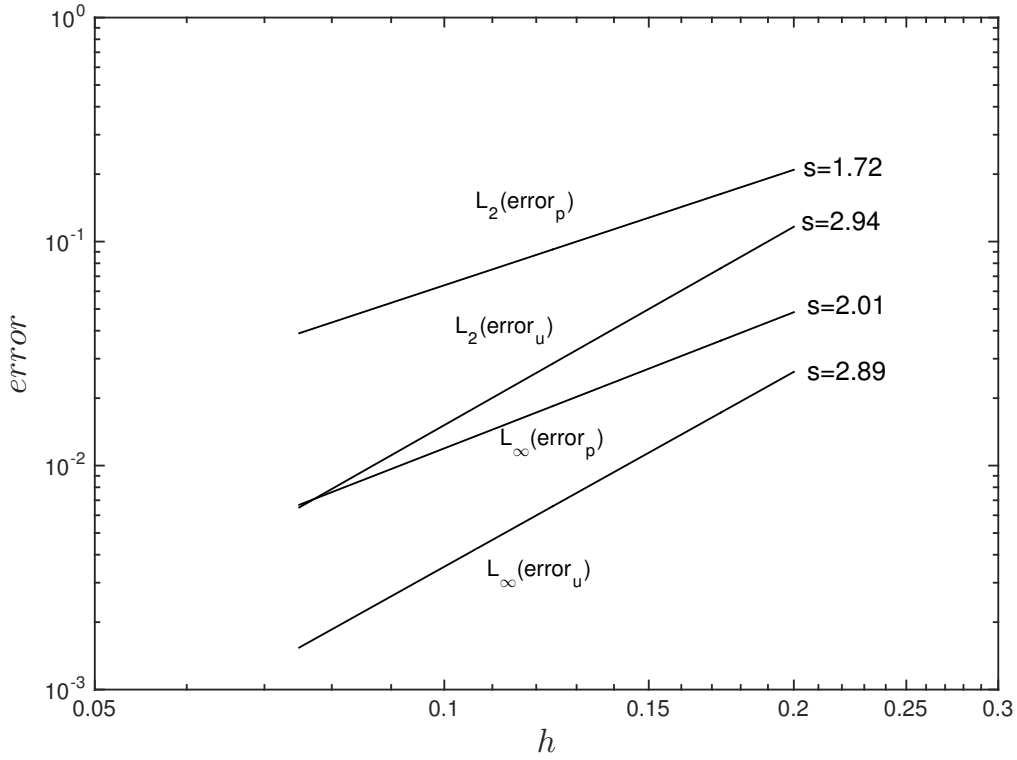

Figure 2.14: Convergence of the method: convergence is given both in terms of infinity and 2-norm errors for pressure and u-velocity (error is obtained by taking the norm of the difference between computed and correct solution), h is the element size, s is the slope.

Chapter 3

Meniscus Growth During Wiping

Cells filled with ink upstream are wiped by doctor blade to remove the excess ink from the land. As a cell translates beneath the wiper blade, some liquid is drawn from the cell and rises over the blade to satisfy the contact angle condition. In the experiments, the wiper is a carbon steel blade having roughness comparable with the cell depth (Kitsomboonloha and Subramanian, 2014, Kitsomboonloha et al., 2012). The radius of curvature of blade tip is 7.5 to 75 times larger than a typical cell size of length 1-10μm. Figure 3.1 shows the geometry of the model. In the model, we have left out certain complications. For example, all surfaces are depicted as planes, except where cells have been etched. The blade covers upper left quadrant of $x - y$ plane, the coordinate axis is fixed at the trailing edge of the stationary blade. We assume that the cell is filled fully with ink, we also do not explicitly account for liquid flow in the thin gap between the stationary wiper blade and the moving substrate. According to Kitsomboonloha and Subramanian (2014), at low speeds, liquid in the gap contributes only about 1% of the total volume flow rate Ud at the trailing edge of the cell where U is the substrate speed, d is the cell depth. This simplification allows us to model the problem without including the thin coating film downstream: the contact line is pinned at the leading edge of the cell.

The flow is not affected by inertial and gravitational forces: the Reynolds number ($Re = \rho UL/\mu$) is less than 10^{-6}, the Weber number ($We = \rho U^2 L/\gamma$) is less than 10^{-5} and the Bond number ($Bo = \rho g L^2/\gamma$) is less than 10^{-8}. The flow is governed by the Stokes equations of motion.

In this chapter, we first analyze the problem in the limit of vanishing capillary number (Ca based on substrate speed U) to predict the smear volume. We, then, solve corresponding Stokes problem by using the methods of chapter 2 for a range of Ca numbers and show that hydrostatics sets an upper bound on the smear volume. Finally, we investigate the effect of blade orientation.

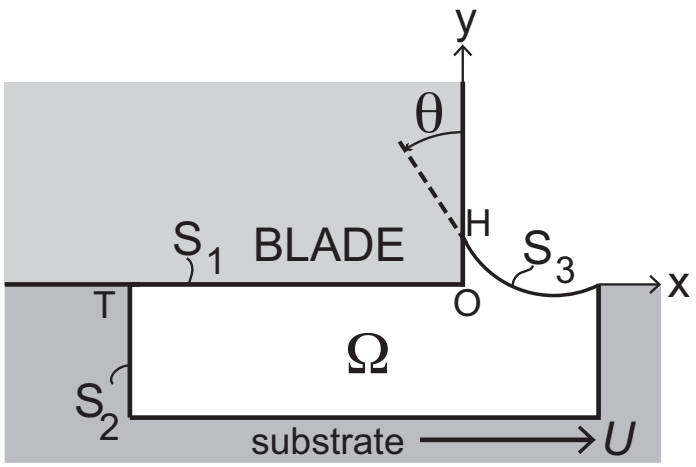

Figure 3.1: Flow domain Ω for the Stokes problem of smearing: S_1, wiper blade; S_2, cell boundary; S_3, free surface. Wiper blade is stationary, cell translates with velocity $U\boldsymbol{i}$.

3.1 Analysis as $Ca \to 0$

In this section we make an analysis in the limit as $Ca \to 0$ to show that the interface grows as circular arc while emerging from beneath the wiper blade. Non-dimensionalized by the length scale $l_s = d$, pressure scale $p_s = \gamma/d$ and velocity scale $u_s = U$ where d is the cell depth, γ is the surface tension and U is the substrate speed; dimensionless stress field is divergenceless:

$$\boldsymbol{\nabla} \cdot \boldsymbol{\sigma} = \mathbf{0}. \tag{3.1}$$

Non-dimensional Newtonian stress-tensor is given by

$$\boldsymbol{\sigma} = -p\boldsymbol{I} + Ca\left(\boldsymbol{\nabla}\boldsymbol{u} + \boldsymbol{\nabla}\boldsymbol{u}^T\right). \tag{3.2}$$

In equation (3.2), capillary number is defined as $Ca = \eta U/\gamma$ with η being dynamic viscosity. p is the dimensionless pressure field and $\boldsymbol{u}$ is the dimensionless velocity field. Continuity equation requires that velocity field is divergenceless:

$$\boldsymbol{\nabla} \cdot \boldsymbol{u} = 0. \tag{3.3}$$

Boundary conditions are given in § 2.1. The scales used in this section differs from § 2.1, though. Therefore, the normal component of the stress on the interface is different from (2.5). The interfacial boundary condition, now, is given by

$$\boldsymbol{n} \cdot (\boldsymbol{\sigma} \cdot \boldsymbol{n}) = -\boldsymbol{\nabla} \cdot \boldsymbol{n}. \tag{3.4}$$

By defining the interface height as $\zeta(x)$ measured from substrate level, we can write the outwatd unit normal on the interface by

$$\boldsymbol{n} = \frac{\boldsymbol{\nabla}\left(y - \zeta(x)\right)}{|\boldsymbol{\nabla}\left(y - \zeta(x)\right)|} = \frac{\boldsymbol{e}_y - \boldsymbol{e}_x \zeta_x}{\left(1 + \zeta_x^2\right)^{1/2}}, \tag{3.5}$$

and the curvature term is found to be

$$\boldsymbol{\nabla} \cdot \boldsymbol{n} = \frac{1 - \zeta_{xx}}{(1 + \zeta_x^2)}. \tag{3.6}$$

By using (3.2) and (3.6), we can rewrite the interfacial boundary condition (3.4) as

$$p + 2Ca\left(\frac{\partial u}{\partial y} + \frac{\partial v}{\partial x}\right)\frac{\zeta_x}{1 + \zeta_x^2} + 2Ca\frac{\partial u}{\partial x}\frac{1 - \zeta_x^2}{1 + \zeta_x^2} = -\frac{\zeta_{xx}}{\left(1 + \zeta_x^2\right)^{3/2}}. \tag{3.7}$$

The contact line is pinned at the leading edge of the cell, and free to move where the free surface meets the wiper blade. Although, as discussed by Cox (1986), when the contact line advances over the wiper blade, the apparent contact angle is a flow property, the difference between the apparent contact angle and static (advancing) angle vanishes as the cube root of the Ca based on the contact line velocity, so we assume contact angle at the moving line over the wiper blade remains at its pre-defined static value given by

$$\boldsymbol{t}_{interface} \cdot \boldsymbol{t}_{wiper} = \cos\theta. \tag{3.8}$$

In the limit as $Ca \to 0$, $dp/dx = 0$ from (3.2). By taking the x–derivative of (3.7) and integrating for the free surface profile, we find the free surface profile $\zeta(x)$, to a first approximation, to be a circular arc which is pinned at the leading edge of the cell and satisfying the contact angle condition (3.8) on the wiper blade. The shape of the interface is decoupled from the flow beneath itself; the meniscus grows as a circular arc. Now, we discuss the hydrostatic stage.

3.2 Hydrostatic limit when $Ca \to 0$

After showing that the interface grows as a circular arc while emerging from beneath the blade, in this section we analyze the hydrostatic limit, show that the contact line rises over the blade with a constant speed and predict the smear volume at the end of meniscus growth stage.

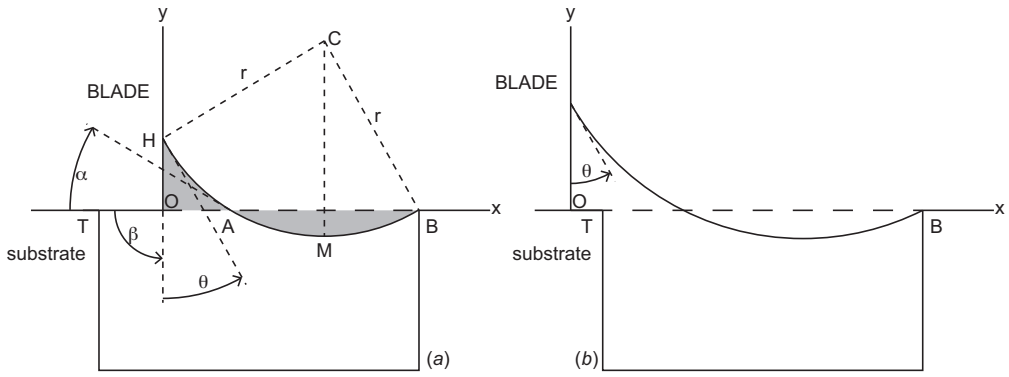

Figure 3.2: Cell translating rightwards beneath a stationary blade occupying the second quadrant of the xOy plane: (a) cell emerging; (b) cell fully emerged. See text for discussion.

Figure 3.2 shows the geometry of the model; emerging and fully emerged cells are shown to emphasize that the analysis covers the evolution from the first state to the second. The coordinate system xOy is orthogonal, with x–axis along the surface of the substrate; β denotes the angle between the blade and the y–axis. Except in § 3.4, $\beta = \pi/2$. We assume the meniscus to be pinned at the leading edge B of the cell.

In the limit as $Ca \to 0$, viscous stress is negligibly small until the interface approaches the substrate at T. Until that occurs, liquid pressure is uniform, and the meniscus is a circular arc HMB. Point A is the intersection of this arc with OB; CM is perpendicular to OB. Arc HMB has three degrees of freedom: its radius r, and the coordinates of its centre C. These variables are determined by the following conditions: because liquid that has risen above line OB has been removed from the cell, the areas shaded in figure 3.2a are equal; the arc passes through B; and it cuts the y–axis at a given angle θ (Young angle).

The area of the shaded curvilinear triangle OAH is given by

$$|OAH| = \tfrac{1}{4}r^2\{4\cos\alpha\ \cos\theta - \sin 2\alpha - \sin 2\theta - \pi + 2(\alpha+\theta)\}\,; \tag{3.9}$$

as shown in figure 3.2a, α is the angle at which arc AMB cuts the x–axis at A. The area of the shaded lens AMB formed by the chord AB and the circular arc below AB is given by

$$|AMB| = \tfrac{1}{2}r^2(2\alpha - \sin 2\alpha). \tag{3.10}$$

Equating areas, then simplifying, we obtain

$$4\cos\alpha\ \cos\theta + \sin 2\alpha = \sin 2\theta + \pi + 2(\alpha - \theta). \tag{3.11}$$

Equation (3.11) holds until the trailing edge (point T in figure 3.2a) approaches the interface.

From (3.11), we see that α is uniquely determined by the value of θ and so does not vary as the cell emerges. As θ is increased from zero to $\pi/2$, α decreases monotonically from 0.568 (about 33°) to zero. In particular, (3.11) admits the solution $\alpha = \theta = 0.482$ (about 28°).

From the geometry of figure 3.2, the arc radius r is given in terms of $|OB| = b$, α and θ by

$$b = r(\cos\theta + \sin\alpha). \tag{3.12}$$

Further, because $|OH| = h = r(\cos\alpha - \sin\theta)$,

$$h = b\frac{\cos\alpha - \sin\theta}{\cos\theta + \sin\alpha}. \tag{3.13}$$

Because α is fixed by (3.11), both the radius r of the meniscus, and its height h, are proportional to distance b of the leading edge of the cell from the blade. In particular, the meniscus rises with constant velocity until the interface approaches the substrate. We note that, although viscosity is locally important near the advancing contact line, its effect there is, merely, to distort the interface locally, and so to produce the dynamic contact angle. That effect is irrelevant here; we are assuming that, in the limit as $Ca \to 0$, the difference between the dynamic and static angles vanishes, as discussed by Hoffman (1975).

Viscous stress becomes essential to the process when the interface approaches the substrate. This can occur either if the trailing edge T of the cell approaches the interface (points A and T coincide), or at the bottom of the cell (point M approaches the cell bottom). In the first case, the hydrostatic stage ends when $|AB|$ is equal to the cell length L. Because, from the geometry of figure 3.2a, $|AB| = 2r\sin\alpha$, the radius r_1 at the end of hydrostatic stage is given by $r_1 = L/(2\sin\alpha)$. In the second case, the hydrostatic stage ends when the distance of point M to OB is equal to the cell depth d: $r - r\cos\alpha = d$. The corresponding value r_2 of the radius is $r_2 = d/(1 - \cos\alpha)$.

Cell aspect ratio L/d determines which case is relevant. As the cell emerges, r increases from zero and the hydrostatic stage ends when r is equal to the smaller of r_1 and r_2. Comparing the expressions for r_1 and r_2, we find that $r_1 < r_2$ if

$$L/d < 2\cot(\tfrac{1}{2}\alpha). \tag{3.14}$$

For perfect wetting ($\theta = 0$), (3.14) corresponds to $L/d < 6.84$. For marginal wetting ($\theta \to \pi/2$), and $\alpha \to 0$: for this system, the hydrostatic stage ends when the trailing edge of the cell approaches the interface, even for a very long shallow cell. In the Kitsomboonloha et al. (2012) experiments, the cells are square in planform, with $L/d = 2$. Because this is within the range defined by (3.14), we now consider only the first case.

As a result of the trailing edge approaching the interface, liquid between O and A is isolated from the cell. We conclude that the amount of liquid removed from the cell is determined by hydrostatics, whereas viscosity will be important in determining how that fixed amount of liquid is smeared over the substrate. The mechanism producing tails operates solely between points O and A; the cell plays no further part.

The area A_* removed from the cell of length L is given by (3.10), with $r = r_1$:

$$A_* = L^2\frac{2\alpha - \sin 2\alpha}{8\sin^2\alpha}. \tag{3.15}$$

As θ is increased from 0 to $\pi/2$, A_*/L^2 decreases from 0.099 to zero: for $\theta = \pi/2$, there is no meniscus, and no liquid is lost from the cell. Further, because the cell area is Ld, the ratio $A_*/(Ld)$ increases linearly with cell aspect ratio L/d.

3.3 Viscous effects

We have shown in §3.1 and 3.2 that the meniscus grows as a circular arc in the hydrostatic limit. Now, by using numerical solutions of the free–boundary problem for the Stokes equations of motion developed in chapter 2, we demonstrate that the hydrostatic analysis of §3.2 provides an upper bound for the amount of liquid removed from the cell. The solution domain is as shown in figure 3.2, except, of course, that interface shape is now to be determined as part of the numerical solution. As shown in figure 3.2, the interface is pinned at the leading edge B of the cell.

As initial state, we take the leading edge B of the cell to be at $x/L = 0.05$. For the initial configuration of the interface, we use the hydrostatic solution. The governing equations are the continuity equation and Stokes equations for a Newtonian liquid: in the process of interest, body force and inertia are negligibly small. At the interface, the shear stress (within the liquid) vanishes, and the normal viscous stress balances the resultant stress exerted by uniform surface tension. At the solid, the no–penetration condition is imposed and the no–slip condition is imposed with two exceptions: within a given distance ℓ of the moving contact line; and within distance ℓ of the intersection between the blade and substrate. Within those regions, the Navier–slip condition is imposed with slip length ℓ; all results are for $\ell/L = 0.01$, static contact angle $\theta = \pi/6$, and $L/d = 2$. For the element at the moving contact line, the length of the shortest edge was set equal to 0.1ℓ.

Of course, viscous stress near the moving contact line distorts the interface and, if the calculation were inadequately resolved, the interface slope would vary abruptly near the blade. For results given here, the angle computed from the solution is always within 1° of the imposed value of $\pi/6$. This accuracy is consistent with the condition given by Sprittles and Shikmurzaev (2012) for the minimum edge length of elements near a moving contact line.

To solve the initial boundary value problem, we use the finite element method explained in Chapter 2.

Figure 3.3 shows the interface height ζ/L at the instant $t = 0.95$ the trailing edge of the cell leaves the blade, corresponding to point T in figure 3.2 coinciding with point O. For $Ca = 1$ (curve (f)) and $Ca = 2$ (curve (g)), the interface slope is small (~ 0.1) everywhere, except very near the blade where the contact angle condition requires the slope to be of the order of unity. As Ca is decreased from curve (g) to curve (b) ($Ca = 0.025$), the interface approaches the static shape shown by curve (a). For clarity, curves for $Ca = 0.01$, 0.005 and 0.0025 are omitted from the figure; they are almost identical with curve (a).

The inset shows the velocity of the contact line. According to the hydrostatic solution (3.13), the contact line rises with uniform speed until the trailing edge of the cell touches

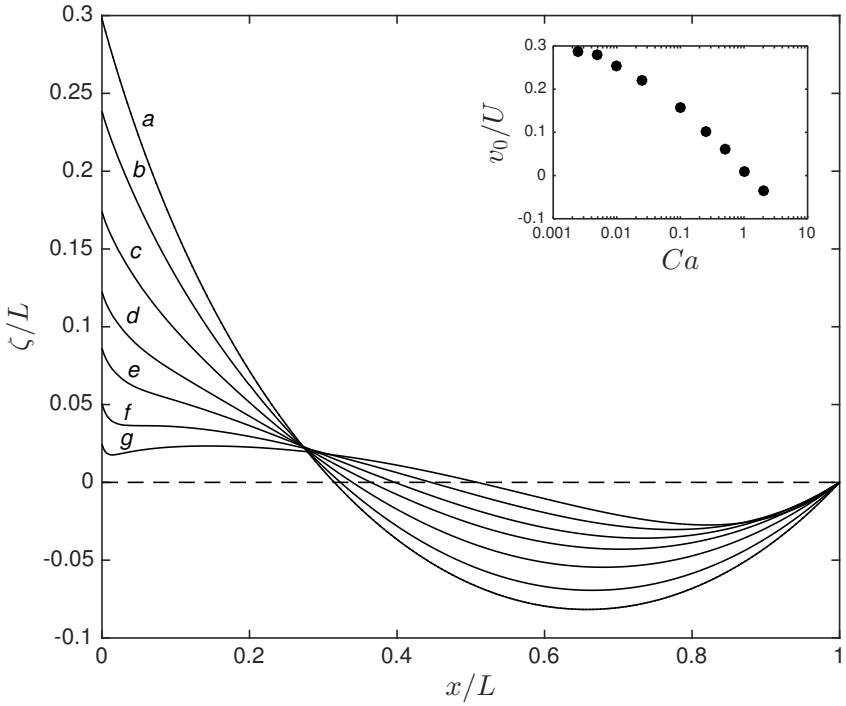

Figure 3.3: Interface shape at the instant $t = 0.95$ the trailing edge of the cell leaves the blade; L/d=2, $\theta = \pi/6$. Curve (a) hydrostatic; curves (b) to (g), computed for $Ca = 0.025, 0.1, 0.25, 0.5$, 1 and 2. Inset, ratio v_0/U of contact line velocity to substrate velocity.

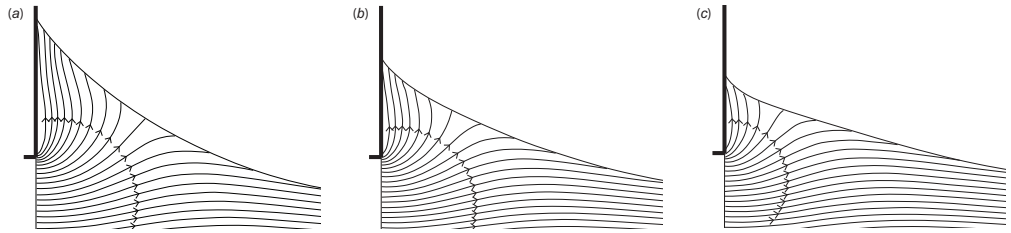

Figure 3.4: Streamlines corresponding to curves (b) to (d) in figure 3.3. Region $0 < x/L < 0.5$, $-0.125 < y/L < 0.25$ and (a), Ca= 0.025; (b), 0.10 and (c) 0.25.

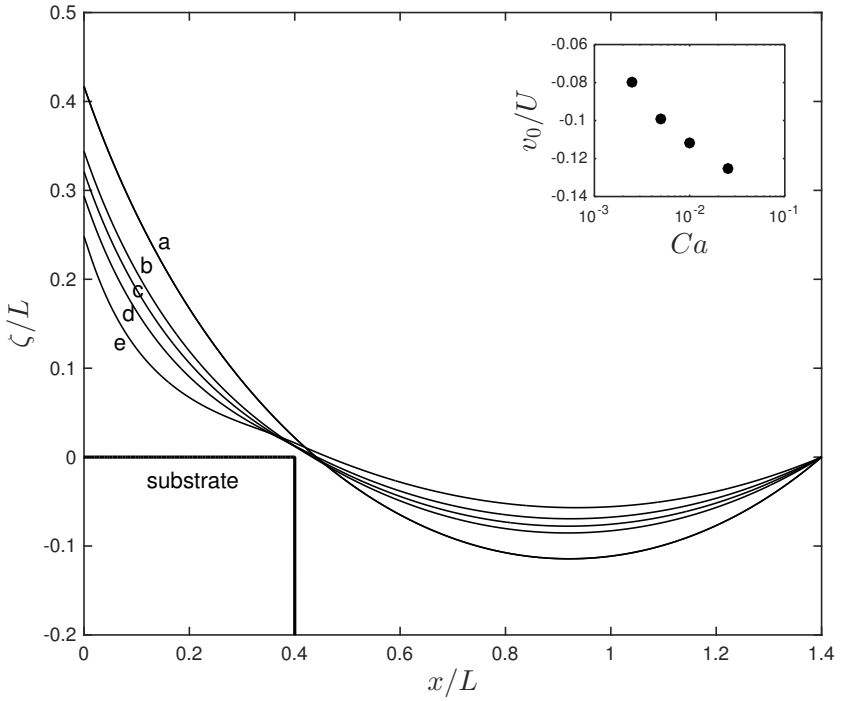

Figure 3.5: Interface shape at the instant $t = 1.35$ the trailing edge of the cell is at $x/L = 0.4$. For θ and L/d, see caption to figure 3.3. Curve (a), hydrostatic; curves (b) to (e), computed for $Ca = 0.0025, 0.005, 0.01$ and 0.025. Inset, ratio v_0/U of contact line velocity to substrate velocity.

the interface; for $\theta = \pi/6$, $v_0/U = 0.298$. The numerical solutions show that v_0 decreases markedly as Ca is increased. To explain that effect, we show streamlines in the next figure.

Figure 3.4 shows, in particular, the behaviour of the streamline that divides liquid rising along the blade from that moving rightwards with the substrate. In all three cases, the contact line is rising over the blade but, as the viscous pressure increases relative to capillary pressure (increasing Ca), an increasing fraction of the liquid is pulled to the right. As a result, the dividing streamline moves leftwards along the interface; this is consistent with the flattening of the interface seen in figure 3.3.

Figure 3.5 shows the interface height at a later time ($t = 1.35$). The trailing edge T of the cell has now advanced to $x/L = 0.4$; this value of x/L is slightly less than that (0.460) at which the hydrostatic analysis predicts that T reaches the interface. Curve (e) for $Ca = 0.025$ shows the later stage of the solution given as curve (b) in figure 3.3: there, viscosity has only a modest effect on interface shape. By contrast, the inflection on curve (e) shows that viscosity now has a significant effect: for the larger values of Ca, the meniscus is beginning to be printed as a tail.

The pronounced effect of viscosity is also apparent in the inset showing the ratio v_0/U:

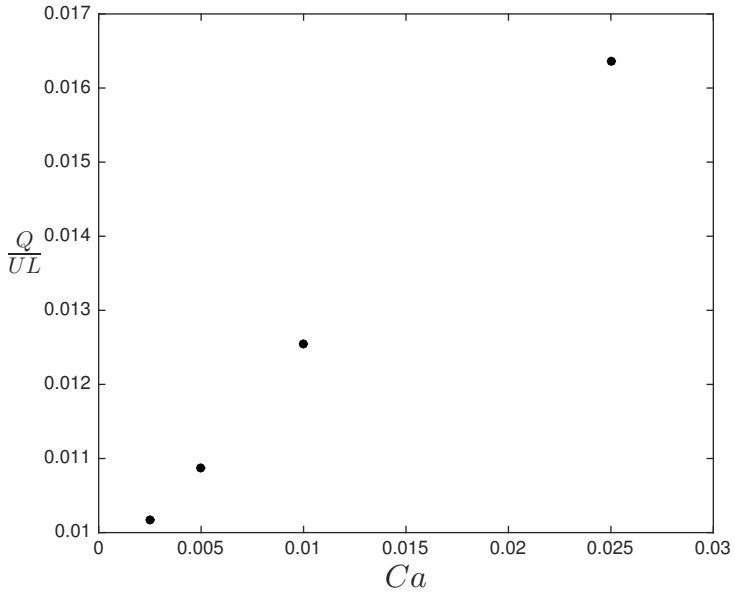

Figure 3.6: Flow rate at the trailing edge of the cell; configuration as in figure 3.5.

even for the smallest value of $Ca = 0.0025$, the contact line is retreating ($v_0/U \simeq -0.08$), whereas in the hydrostatic solution, the contact line advances with uniform speed ($v_0/U = 0.298$) until the trailing edge of the cell touches the interface.

We note that the retreating meniscus deposits no film on the blade $x = 0$. Two explanations offer themselves. First, the geometry differs from that in dip coating. Viscous stress here plays a double role; shear stress near the contact line promotes film deposition but substrate drag opposes it. Second, even if that effect were absent, as in dip coating or bubble flow in a tube, no film is deposited if the capillary number Ca_0, based on contact line velocity v_0, is less than a critical value: Ca' depends on static contact angle θ and, weakly, on slip length ℓ and on the radius r of curvature of the outer meniscus (Quéré 1991, equation 5; Eggers 2005, equation 41). Because Ca' is an increasing function of ℓ/r, the relatively large value of $\ell/r \sim 10^{-2}$ used here would inhibit coating.

The preceding figures show clearly that the area under the meniscus is a decreasing function of Ca. It remains to show that, with decreasing Ca, liquid is increasingly trapped as the trailing edge of the cell approaches the interface.

From figure 3.6, we see that, for the configuration shown in figure 3.5, the flow rate $Q = \int_0^\zeta v_x \, \mathrm{d}y$ through the restriction between the interface and trailing edge of the cell is $\sim 1\%$ of the characteristic flow rate UL within the cell itself. The ratio $Q/(UL)$ decreases with decreasing Ca. We conclude that hydrostatics provides an upper bound to the volume left behind on the substrate. The problem of minimizing smearing simplifies to one of reducing that upper bound.

3.4 Blade geometry

The smears shown in Kitsomboonloha et al. (2012, figure 7) were observed in experiments in which the cell length $L = 7.5\,\mu$m, and the radius of the blade tip, 75 μm. Kitsomboonloha and Subramanian (2014, figure 8) show that printed features become more sharply when the blade is polished to reduce the tip radius to 3 μm. In this section, we use hydrostatic theory to suggest why polishing is effective.

In the first case, the tip radius is $10L$, and a careful sketch shows that the curved surface of the blade can be modeled, at the scale of the cell, by a flat blade making an acute angle β with the x–axis. (Though in figure 1b of Kitsomboonloha et al. (2012), the blade as a whole is shown as making an obtuse angle with the x–axis, we are concerned here the local angle where the cell leaves the blade; that angle is acute.)

Assuming now that the angle made by the blade with the x–axis is now β, rather than $\pi/2$, the angle made by the interface with the vertical at the contact line H is $\theta' = \theta + \beta - \pi/2$. The effect of tilting the blade is to create additional area beneath it. To illustrate this effect, we consider the case $\theta' \geq 0$ in which the area A of the meniscus can be calculated using results already given: to obtain the area A_C of the curvilinear triangle formed by the interface, x–axis, and abscissa passing through H, we need only replace θ in (3.9) by θ'. The other contribution is the area A_T of the right triangle formed by that same abscissa, the blade, and x–axis: $A_T = (r^2/2)(\cos\alpha - \sin\theta')^2 \cot\beta$. As β is reduced, A_T increases without bound. As far as the cell is concerned, tilting a flat blade creates a large volume sink.

Equating the total area $A = A_C + A_T$ to the area $|AMB|$ removed from the cell, then simplifying, we find that α, β and $\chi = \beta + \theta$ satisfy the relation

$$4\cos\alpha\ \sin\chi + \sin 2\chi + \sin 2\alpha + 2(\cos\alpha + \cos\chi)^2 \cot\beta = 2(\pi + \alpha - \chi). \tag{3.16}$$

This equation holds for $\chi \geq \pi/2$.

For a system that is only marginally wetting, so that $\theta \uparrow \pi/2$, the condition $\chi \geq \pi/2$ is satisfied even for $\beta \ll 1$. To obtain the solution of (3.16) in that case, we note that arc AH in figure 3.2 then approximates to chord AH. From the geometry of the triangle formed by the blade, chord AH and the x–axis, $\beta + \theta + \alpha = \pi$, whence $\alpha \to \pi - \theta$ as $\beta \to 0$. To obtain the next term in this approximation, we substitute the series

$$\alpha \sim \pi - \theta + c\beta^{1/2}, \tag{3.17}$$

into (3.16), and find that $c = -(2\pi + \sin 2\theta - 2\theta)^{1/2}/\sin\theta$. Together, (3.15) and (3.16) determine the area A_* that has been removed from the cell when its trailing edge reaches the interface.

Figure 3.7 shows $A_*/(Ld)$ as a function of blade angle β for contact angle $\theta \uparrow \pi/2$. According to the results in §3.2, for this value of θ, and blade angle $\beta = \pi/2$, a negligibly small amount of liquid is removed: $A_* \to 0$ at the right end of the figure. At the other extreme, $\beta \to 0$; in this case, $\alpha \to \pi/2$. The inset shows the corresponding meniscus: it is a semi–circle spanning the cell and having a little finger that reaches up to touch the blade,

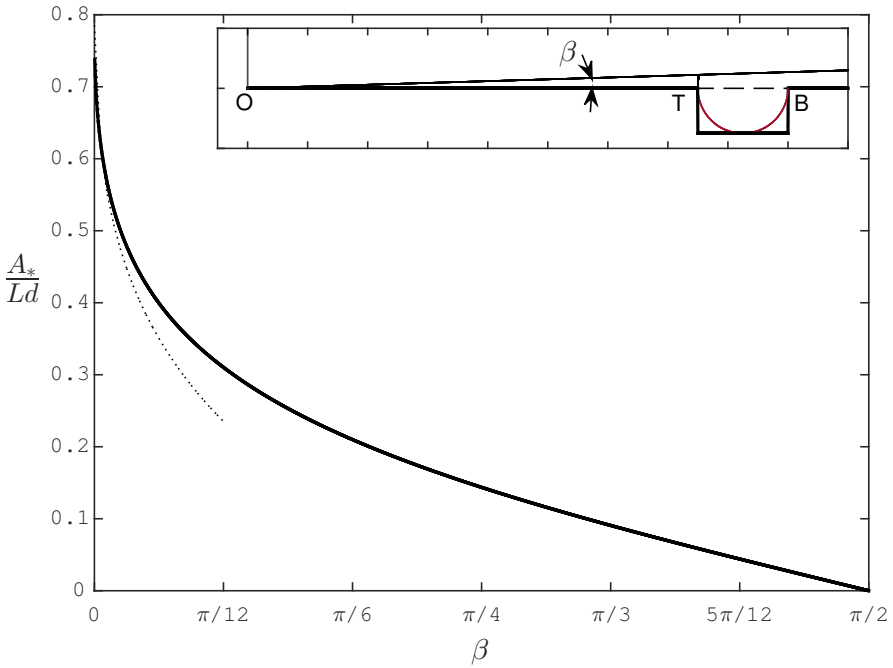

Figure 3.7: Relation defined by (3.15) and (3.16) for L/d=2, and contact angle $\theta \uparrow \pi/2$. Solid curve, equation (3.16); dotted curve, small–β asymptote (3.17).

thereby completing the right triangle whose area is the very A_T described above. It remains to verify that this extreme situation is not an artefact of assuming a flat blade.

Figure 3.8 shows the corresponding situation for the parabolic blade $y = (x + x_0)^2/(2\rho)$, and cell aspect ratio $L/d = 2$. The coordinate origin O is at the centre of the top of the cell; the ends of the cell are at $x = \pm d$. The sketch is drawn to scale for $\varepsilon = L/\rho = 0.1$; it suggests that the following assumptions hold in the limit as $\varepsilon \to 0$: (a) the contact line is at $x = -L/2$; (b) when the trailing edge reaches the meniscus, as shown in the figure, the cell has emerged a distance $x_0 \gg L$; and (c) the slope of the parabola at the contact line H is vanishingly small. We assume, then verify, these properties.

First, by assumption (a), the area of the meniscus is given by $A_2 = \int_{-x_0}^{-L/2} y \, \mathrm{d}x$. Equating that area to the area $A_1 = 1/2L^2(1 - \pi/4)$ removed from the cell, then using (b) to neglect a small term of the order of L/x_0, we find that in the limit as $\varepsilon \to 0$,

$$x_0/L \sim 0.863/\varepsilon^{1/3}; \tag{3.18}$$

this justifies assumption (b). Next, the contact line H is located at the intersection of the parabola $y = (x + x_0)^2/(2\rho)$ with the circular arc $x^2 + y^2 = L^2/4$. Eliminating y between these equations, then using (b) to neglect terms of the order of L/x_0, we find that

$$x_c \sim -(L/2)(1 - 0.373\varepsilon^{4/3}); \tag{3.19}$$

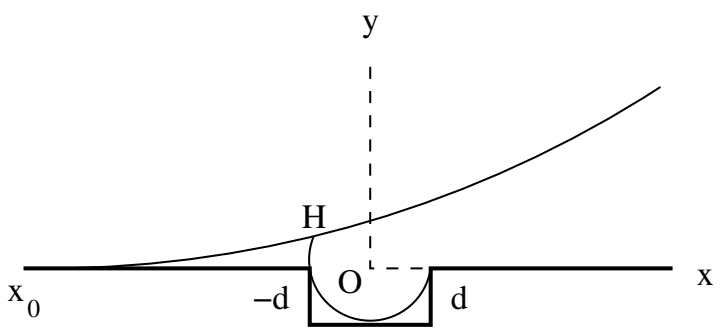

Figure 3.8: Meniscus of a marginally wetting liquid beneath a parabolic blade.

this justifies assumption (a). Lastly, because $x_0 \gg |x_c|$, the slope of the parabola at H is given by $x_0/\rho \sim 0.863\varepsilon^{2/3}$ showing that the slope of the parabola is vanishingly small at H; this justifies the assumption (c). We conclude that if the tip radius of the blade is large compared with the cell length, most of cell volume is drawn into the meniscus even for a marginally wetting system.

By examining the limit $Ca \to 0$, we have shown that the phenomenon of 'drag–out' during the wiping stage of gravure printing effect phenomenon in gravure printing is caused by the growth of a meniscus on the wiping blade. For $Ca \to 0$, viscosity only enters significantly when the trailing edge of the cell approaches the interface, thereby isolating the meniscus from the cell. The problem of tail formation now reduces to that of the coating of a substrate by the meniscus extending from the blade to the trailing edge of the cell. We treat that problem in the following chapter.

Chapter 4

Tail Formation

We show in chapter 3 that liquid is drawn from a cell passing beneath the wiper blade. In the limit of vanishing Ca, that liquid becomes isolated from the cell. In this chapter, we first analyze printing of the resulting meniscus in this limit. As Ca is increased, however, we consider the existence of the cell due to the leakage from meniscus into the cell as shown in figure 3.6 of chapter 3.

4.1 Outer problem: static prediction

From the hydrostatic analysis in §3.2, the meniscus is separated from the cell as shown in figure 4.1, the contact line is pinned at the trailing edge T of the cell. As a result, the angle α, the angle at which the interface makes with the horizontal as shown in figure 4.1, is no longer fixed but, instead, decreases as the distance $x_T = |OT|$ increases. Because the area under the meniscus is now constant, and equal to A_* given in (3.15), equation (3.10) determines radius of curvature r of the circular arc meniscus as a function of α. Solving the

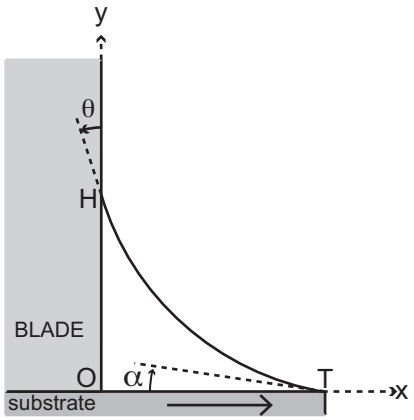

Figure 4.1: Meniscus sitting between blade and trailing edge (T) of the cell.

resulting expression for r, we find that

$$\frac{r}{A_*^{1/2}} = \frac{2}{\{4\cos\alpha\,\cos\theta - \sin 2\alpha - \sin 2\theta - \pi + 2(\alpha+\theta)\}^{1/2}}. \tag{4.1}$$

Further by geometry $x_T = |OT| = r(\cos\theta - \sin\alpha)$. Substituting for r from (4.1), we obtain

$$\frac{x_T}{A_*^{1/2}} = \frac{2(\cos\theta - \sin\alpha)}{\{4\cos\alpha\,\cos\theta - \sin 2\alpha - \sin 2\theta - \pi + 2(\alpha+\theta)\}^{1/2}}. \tag{4.2}$$

In parametric form, (4.1) and (4.2) determine r as a function of the distance x_T from the blade to the trailing edge of the cell. Because (4.1) and (4.2) contain the scale $A_*^{1/2}$, the meniscus is not geometrically self–similar.

For later use, we note that in the limit as $\alpha \to 0$,

$$x_T = r_0\,(\cos\theta - \alpha) + O(\alpha^2), \tag{4.3}$$

$$r = r_0 + \frac{r_o^3 \cos\theta}{4A_*}\alpha^2 + O(\alpha^3), \tag{4.4}$$

so

$$r = r_0 + \frac{r_0 \cos\theta}{4A_*}\left(r_0\cos\theta - x_T\right)^2 + O(\alpha^3). \tag{4.5}$$

Here, r_0 is obtained by setting $\alpha = 0$ in (4.1).

Figure 4.2 shows radius r as a function of distance x_T for $\theta = 0$ and $\theta = \pi/6$. For a given value of θ, the curve begins at a point corresponding to the value of α appropriate to the end of meniscus growth stage, and terminates at the value $x_T = r_0\cos\theta$ given by (4.3). According to (4.5), for arbitrary θ, the slope dr/dx_T vanishes at the terminus. Lastly we note that, for $\theta = 0$ and $\theta = \pi/6$, r decreases by about less than one–third during this stage.

We have shown that, in the limit of vanishing capillary number, the meniscus develops in two stages. As the cell emerges during meniscus growth stage, the radius r of the arc increases from zero to a maximum $r_1 = L/(2\sin\alpha)$ when the interface pins on the trailing edge of the cell. As a result, in the meniscus printing stage, r decreases as the cell continues to translate. This decrease continues until $\alpha \to 0$. We now discuss the effect of viscosity.

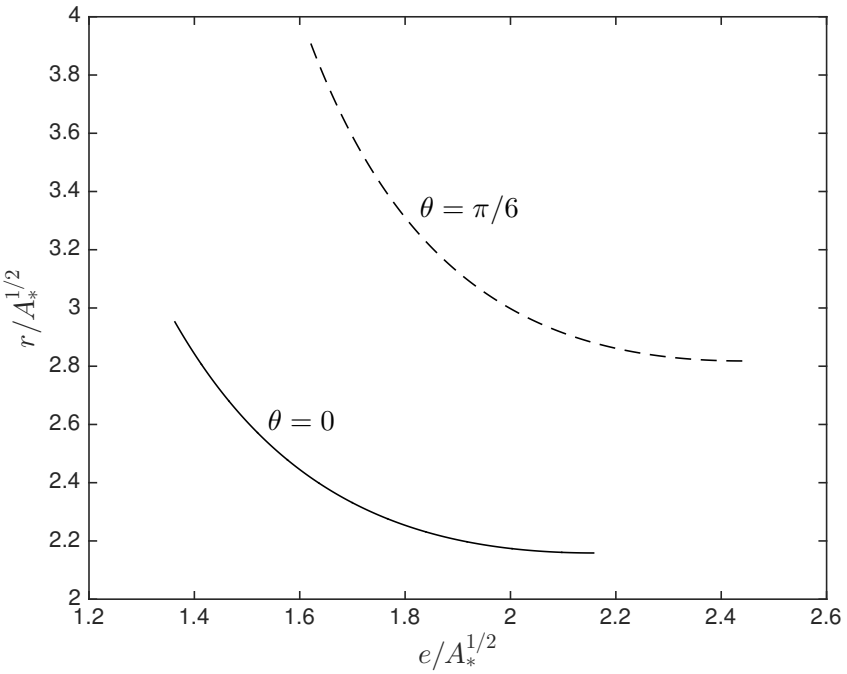

Figure 4.2: Relation between r and distance $x_T = |OT|$ for $\theta = 0$ (solid line), $\theta = \pi/6$ (dashed line).

4.2 Inner problem: viscous effect

As shown by the static analysis, in the limit as $Ca \to 0$, the meniscus is a circular arc until the effect of viscosity first becomes important; this occurs at the trailing edge of the cell. We now make the analysis in the neighborhood of the trailing edge of the cell. Figure 4.3 shows near the trailing edge of the cell. The effects of viscosity are important here rather than the blade.

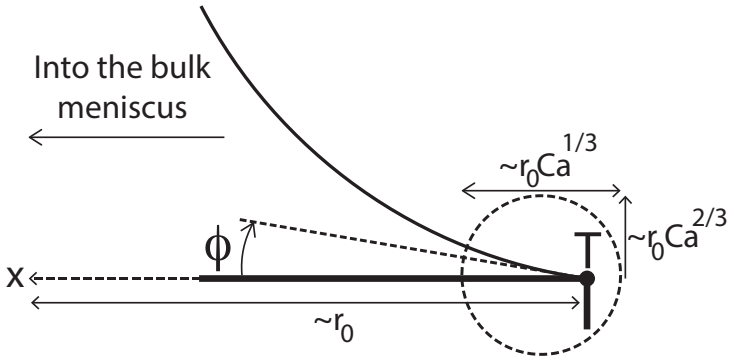

Figure 4.3: Inner problem: meniscus pinned at the trailing edge T of the cell, x grows into the meniscus.

In the limit of vanishing Ca, there exists an inner and outer structure. Outer problem is given in §4.1. We now formulate the inner problem by making a local analysis as $Ca \to 0$ around the pinned contact line.

ϕ being the apparent contact angle, a lubrication analysis is appropriate for $\phi << 1$. Here ϕ is a parameter replacing α and it is going to be determined by matching the inner and outer problems. Moving with the reference frame fixed at T, with x now chosen to increase toward the meniscus as shown in figure 4.3; the evolution of the interface ζ measured from horizontal is given by

$$\frac{\partial \zeta}{\partial t} + \frac{\gamma}{3\eta}\frac{\partial}{\partial x}\left(\zeta^3 \frac{\partial^3 \zeta}{\partial x^3}\right) = 0. \tag{4.6}$$

As in the Landau-Levich coating problem, the boundary condition is that pressure must match that in the static meniscus. To impose this, for small slope interface, we set

$$\zeta = \phi x + \frac{1}{2r}x^2 + \hat{\zeta}, \tag{4.7}$$

where ϕ is the slope of the interface at $x = 0$ and r is the radius of curvature of the circular arc meniscus and $\hat{\zeta}$ is the difference between the inner solution and parabolic interface. Although ϕ is to be determined, r has to be the same as the bulk meniscus: r is specified. (4.7) holds near $x = 0$ provided $\phi << 1$; $\hat{\zeta}$ is not assumed to be small. Note that provided

$\hat{\zeta}$ is $o(x^2)$ for large x, (4.7) ensures that pressure is matched to the static solution. We put (4.7) into the evolution equation (4.6) to obtain:

$$\dot{\phi}x + \frac{1}{2}\frac{d}{dt}\left(r^{-1}\right)x^2 + \frac{\partial\hat{\zeta}}{\partial t} + \frac{\gamma}{3\eta}\frac{\partial}{\partial x}\left\{\left(\phi x + \frac{1}{2r}x^2 + \hat{\zeta}\right)^3\frac{\partial^3\hat{\zeta}}{\partial x^3}\right\} = 0. \tag{4.8}$$

From the static analysis, $\dot{\phi}x/(\dot{r^{-1}}x^2) \sim (\phi r)/(x_T x) << 1$, ($x_T$ denotes the distance from trailing edge to the blade). To $O(\phi^2)$, $r = r_0$ from (4.4), therefore the second term in (4.8) is small compared with the first term. Eliminating the second term in (4.8) and rescaling to the inner region by using the scales $x = r_0 Ca^{1/3}\hat{x}$, $\phi = Ca^{1/3}\hat{\phi}$, $\hat{\zeta} = r_0 Ca^{2/3}\hat{y}$ and $t = r_0/UCa^{1/3}\hat{t}$ with $\dot{\phi} = -U/r_0$, $r = r_0$, we obtain the evolution equation of the inner problem:

$$\frac{\partial\hat{y}}{\partial\hat{t}} + f = 0, \tag{4.9}$$

where

$$f = -\hat{x} + \frac{1}{3}\frac{\partial}{\partial\hat{x}}\left\{\left(\hat{\phi}x + \frac{1}{2}\hat{x}^2 + \hat{y}\right)^3\frac{\partial^3\hat{y}}{\partial\hat{x}^3}\right\}, \tag{4.10a}$$

$$\hat{\phi} = Ca^{-1/3}\phi_0 - \hat{t}. \tag{4.10b}$$

Equation (4.2-4.10) is valid for $0 \leq \hat{x} < \infty$. Boundary conditions are:

$$\hat{y}(0,\hat{t})\frac{\partial^3\hat{y}(0,\hat{t})}{\partial\hat{x}^3} = 0, \tag{4.11a}$$

$$\frac{\partial\hat{y}(\infty,\hat{t})}{\partial\hat{x}} = 0. \tag{4.11b}$$

Boundary condition (4.11a) is no flux condition at T, (4.11b) is the growth condition. The initial condition is

$$\hat{y}(\hat{x},0) = 0. \tag{4.12}$$

We integrate (4.9-4.12) implicitly and map the domain $0 < \hat{x} < \infty$ onto interval [0,1] by introducing new coordinate defined by $z = \hat{x}/(1+\hat{x})$(Appendices A and B give the details of the numerical method).

We have verified by using 3 different initial ϕ (ϕ_0) that, the solution is, asymptotically, independent of ϕ_0 for $\phi << \phi_0$; therefore we use the small slope analysis here even though ϕ_0 is not necessarily small. In figure 4.4, we plot the difference between the actual and parabolic interface. We take the initial value of ϕ corresponding to the problem with contact angle on the blade is $\theta = \pi/6$ and α when the interface touches the trailing edge of the cell at the end of hydrostatic stage. $\phi \to 0$ before the evolution converges to steady state. To be able to see how close we are to the steady state solution when ϕ vanishes, we continue integrating

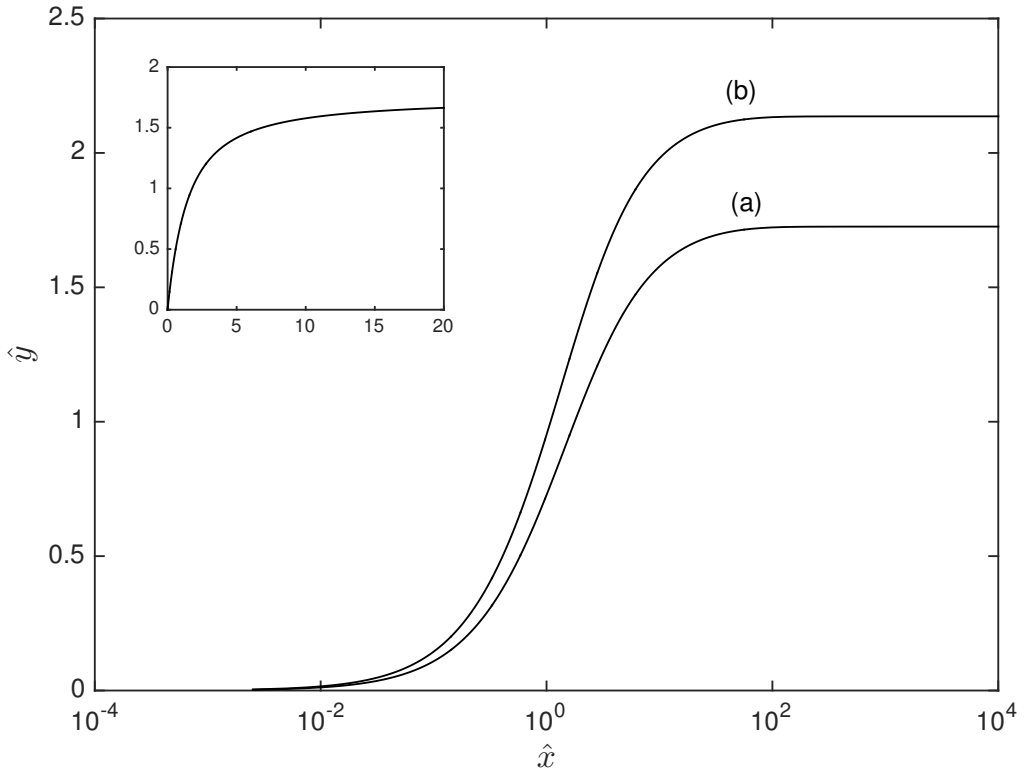

Figure 4.4: Inner viscous solution for the meniscus printing problem, (a) $\phi = 0$, (b) steady state solution. $\phi_0 = 0.468$ is taken to be corresponding to the problem with contact angle on the blade is $\theta = \pi/6$. Inset: the neighborhood of the contact line in linear scale corresponding to curve (a).

in time by setting $\phi = 0$ after that point (when $\hat{y} \sim 1.7$). $\hat{y}$ converges to 2.136 as $\hat{x} \to \infty$ as $1/\hat{x}$.

As shown by the inset in figure 4.4, the $\hat{\zeta}$ is concave down, approaches a constant very slowly like $1/\hat{x}$. The curvature is positive everywhere, highest at T; pressure perturbation is produced by a squeeze film flow.

Because $\hat{\zeta}$ approaches to limiting value at infinity very slowly, separation of length scales exists under one of the two conditions: if $\pi/2-\theta >> Ca^{1/3}$ or if the mass under the meniscus is infinite. The second condition is not valid for the meniscus printing problem because the mass under the meniscus is limited by the meniscus growth stage. First condition, on the other hand, is observable. Though it is not practical to solve the corresponding Stokes problem of meniscus printing for too small Ca numbers, lubrication analysis is valid when the interface slope is small and we treat this problem in §4.7. We, of course, compare the inner viscous solution with the Stokes solution even though the separation of length scales does not exist for the Ca values of order 10^{-3} studied.

4.3 Composite expansion

In this section we form the composite expansion of meniscus printing problem by matching the outer limit of the inner problem to the inner limit of the outer problem.

For $\phi << \phi_0$, at a fixed instant, the overall effect of viscous flow (squeeze film) near T, is to displace the interface upwards by an amount $\delta = \lim_{\hat{x}\to\infty} \hat{y}$. This value varies with time t, but since $\phi = \mathrm{fn}(t)$, δ can also be considered to be a function of the single variable ϕ. The displacement thickness δ is as shown in figure 4.5. To ensure mass conservation, radius r and angle α are defined as the solutions of (4.1) and (4.2). However, the quantity x_A is no longer exactly equal to the distance $|OT| = x_T$ to the trailing edge of the cell. Instead x_A now refers to the distance $|OA|$ to the point A at which the static meniscus extrapolates to the x–axis, an apparent point. From the rotating meniscus solution, the displacement $|TG| = r_0 Ca^{2/3}$ (to within a constant factor); from the geometry of $\triangle TAG$, $|TA| = |TG|/\alpha = r_0 Ca^{1/3}/\hat{\alpha}$ where the scaling $\alpha = Ca^{1/3}\hat{\alpha}$ has been used. The area under the actual interface (solid curve), differs from that A_* under the circular arc meniscus by an amount of the order of the area of triangle TAG; that area is of the order of $r_0^2 Ca/\hat{\alpha}$. Mass is, therefore, conserved to within an error of the order of Ca; this error is of the same order as that made in taking the outer meniscus to be a circular arc.

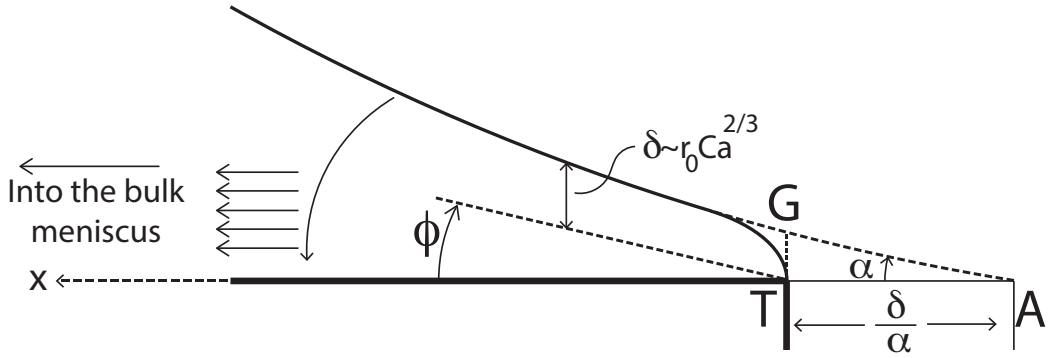

Figure 4.5: Effect of viscosity: meniscus is displaced by an amount δ as the trailing edge T advances.

Figure 4.6 shows the geometry of the whole meniscus. We let x_T be the abscissa at the trailing edge of the cell and x_A be the abscissa at an apparent point where the outer meniscus cuts the x–axis.

The outer region is defined by the limit $Ca \to 0$ ($x \neq x_T$) as given in § 4.1. To $O(Ca)$, the pressure in the outer region meniscus is uniform and the interface is a circular arc. The area A_* beneath the arc is defined by the initial condition (for meniscus printing stage).

We let the radius of this arc be r and the angle at which the arc cuts the x–axis be α. Expressed in terms of r, α and the contact angle θ, the coordinates of the centre C of the circular arc are $\{r\cos\theta, r\cos\alpha\}$. The equation of the circle is

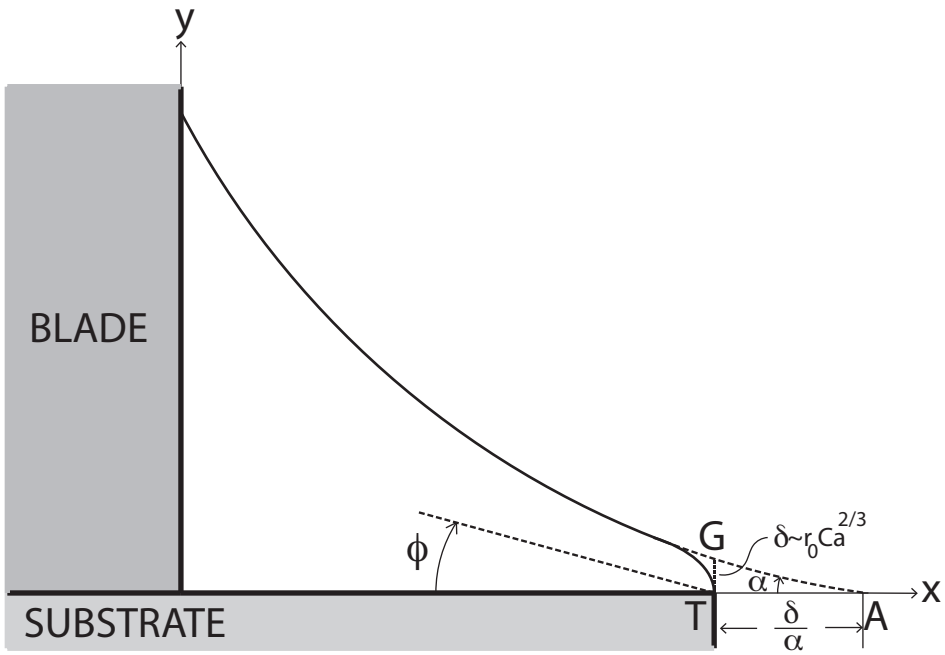

Figure 4.6: Geometry for the composite expansion.

$$(x - r\cos\theta)^2 + (y - r\cos\alpha)^2 = r^2. \tag{4.13}$$

The area A_* under the interface is imposed by the initial condition: this constraint means that r is a known function of the parameter α. Consequently, the abscissa a of the point A at which the arc cuts the x–axis is also a known function of α: setting $y = 0$ in (4.13), then solving for $x = x_A$, we obtain $x_A = r(\cos\theta - \sin\alpha)$. In particular, for $\alpha \to 0$, $r \sim r_0\{1 + O(\alpha^2)\}$, and

$$x_A = r_0(\cos\theta - \alpha) + O(\alpha^2). \tag{4.14}$$

Matching to inner viscous solution gives the remaining condition needed to determine the interface. Expressing (4.13) in terms of $x - x_A$, then solving for y^O, the ordinate of the outer meniscus, we obtain:

$$y^O = r\cos\alpha - r\cos\alpha\big[1 + 2(x - x_A)r^{-1}\tan\alpha\,\sec\alpha - (x - x_A)^2 r^{-2}\sec^2\alpha\big]^{1/2}. \tag{4.15}$$

We find the inner limit of the outer solution by expanding (4.15) to $O([x - x_A]^2)$:

$$y^O \sim (x_A - x)\tan\alpha + \frac{1}{2r}(x - x_A)^2\sec^3\alpha. \tag{4.16}$$

Equation (4.16) can also be obtained by forming the Taylor expansion about $x = x_A$, using $y' = -\tan\alpha$ and $y''(1+y'^2)^{-3/2} = r^{-1}$.

The inner solution is defined by the limit $Ca \to 0$ (fixed $[x_T - x]/Ca^{1/3}$). The function y^I vanishes at x_T. The outer limit of the inner solution is defined by $Ca \to 0$ ($x \neq x_T$). In this limit

$$y^I \sim \phi(x_T - x) + \frac{1}{2r_0}(x_T - x)^2 + r_0 Ca^{2/3}\delta. \tag{4.17}$$

In (4.17), the coefficient of $(x_T - x)^2$ must equal $\lim_{\alpha\to 0} r$, because matching of the pressure requires the outer limit of the (inner) curvature to equal the uniform curvature of the outer interface. The apparent contact angle ϕ is to be determined by matching. Because ϕ appears as a parameter (replacing α) in the statement of the inner viscous problem, the displacement thickness δ is a function of ϕ.

We now perform the matching: for $x_T - x = O(r_0 Ca^{1/3})$, the second and third terms in (4.16) are $O(r_0 Ca^{2/3})$. Matching consists of making the difference $y^O - y^I = o\Big(r_0 Ca^{2/3}\Big)$; the difference is then small compared with either y^O or y^I.

Using the identity $x_A - x = (x_A - x_T) + (x_T - x)$ to express y^O in terms of $x - x_T$, then rearranging, we obtain

$$\begin{array}{rcccccc} y^O & \sim & \alpha(x_A - x_T) + \frac{1}{2r_0}(x_A - x_T)^2 & + & (x_T - x)[\alpha + \frac{1}{r_0}(x_A - x_T)] & + & \frac{1}{2r_0}(x_T - x)^2; \\ y^I & \sim & r_0 Ca^{2/3}\delta & + & (x_T - x)\phi & + & \frac{1}{2r_0}(x_T - x)^2. \end{array} \tag{4.17a,b}$$

Equating coefficients in (4.17a,b), we obtain

$$r_0\phi = r_0\alpha + (x_A - x_T), \tag{4.18a}$$

$$\alpha(x_A - x_T) + (x_A - x_T)^2/(2r_0) = r_0 Ca^{2/3}\delta. \tag{4.18b}$$

In this system, δ is computed as a function of ϕ as part of the inner viscous solution. The unknowns are therefore ϕ, α and x_A. Equation (4.14) provides the remaining relation needed to determine the three unknowns. Eliminating $x_A + r_0\alpha$ between (4.18a) and (4.14), we find that

$$\phi = (\cos\theta - x_T/r_0). \tag{4.19}$$

This equation determines the coefficient entering into the inner viscous problem. Solving the inner problem then determines δ.

With δ determined, α is found by eliminating $x_A - x_T$ between (4.18a) and (4.18b): this gives

$$\alpha = \left[\phi^2 - 2Ca^{2/3}\delta\right]^{1/2}. \tag{4.20}$$

Lastly, according to (4.18a), $x_A - x_T = r_0(\phi - \alpha)$:

$$x_A - x_T = r_0\big\{\phi - \big[\phi^2 - 2Ca^{2/3}\delta\big]^{1/2}. \tag{4.21}$$

The quantities x_A, α and ϕ have been determined; mass is conserved; and the inner and outer solutions have been matched.

The composite solution is

$$y^C \sim y^O + r_0 Ca^{2/3}\{y_{\rm num} - \delta\}\,; \tag{4.22}$$

In (4.22), y^O is given by (4.15), and $y_{\rm num}$ denotes the numerical solution of the inner viscous problem, specifically the component that approaches δ far from x_T. In the outer limit, $y^C \sim y^O$. Using (4.17a,b), in the inner limit

$$y^O \sim r_0 Ca^{2/3}\delta + (x_T - x)\phi + \frac{1}{2r_0}(x_T - x)^2; \tag{4.23}$$

so that

$$y^C \sim (x_T - x)\phi + \frac{1}{2r_0}(x_T - x)^2 + r_0 Ca^{2/3}\; y_{\rm num}. \tag{4.24}$$

The matching allows for the variation in slope that occurs between x_T and x_A as the viscous effect becomes stronger.

To show the meniscus rotation, we form the composite solution for $\theta = 5\pi/12$. The composite solution is for fixed time, the corresponding static solution at the same time is found from (4.1) and (4.2) and the parabolic approximation is computed at the corresponding time by using (4.25).

Figure 4.7 shows the composite expansion for $Ca = 10^{-7}$ and $Ca = 10^{-8}$ and $\theta = 5\pi/12$. The matching is valid provided $\phi^2 > 2r_0 Ca^{2/3}\delta$. In figure 4.7; $\alpha = 0.0030$, $\phi = 0.0065$, $|x_A - x_T| = 0.0095$ for $Ca = 10^{-7}$; $\alpha = 0.0012$, $\phi = 0.0030$, $|x_A - x_T| = 0.0049$ for $Ca = 10^{-8}$. To be able to show the structure at the tip, we subtract the parabolic interface which given by

$$y^P = (x_T - x)\phi + \frac{1}{2r_0}(x_T - x)^2 \tag{4.25}$$

from the actual interface y^O. As shown by the insets, the rotation of meniscus is visible at the tip region and as Ca is decreased separation of length scales is also visible close to the tip (T).

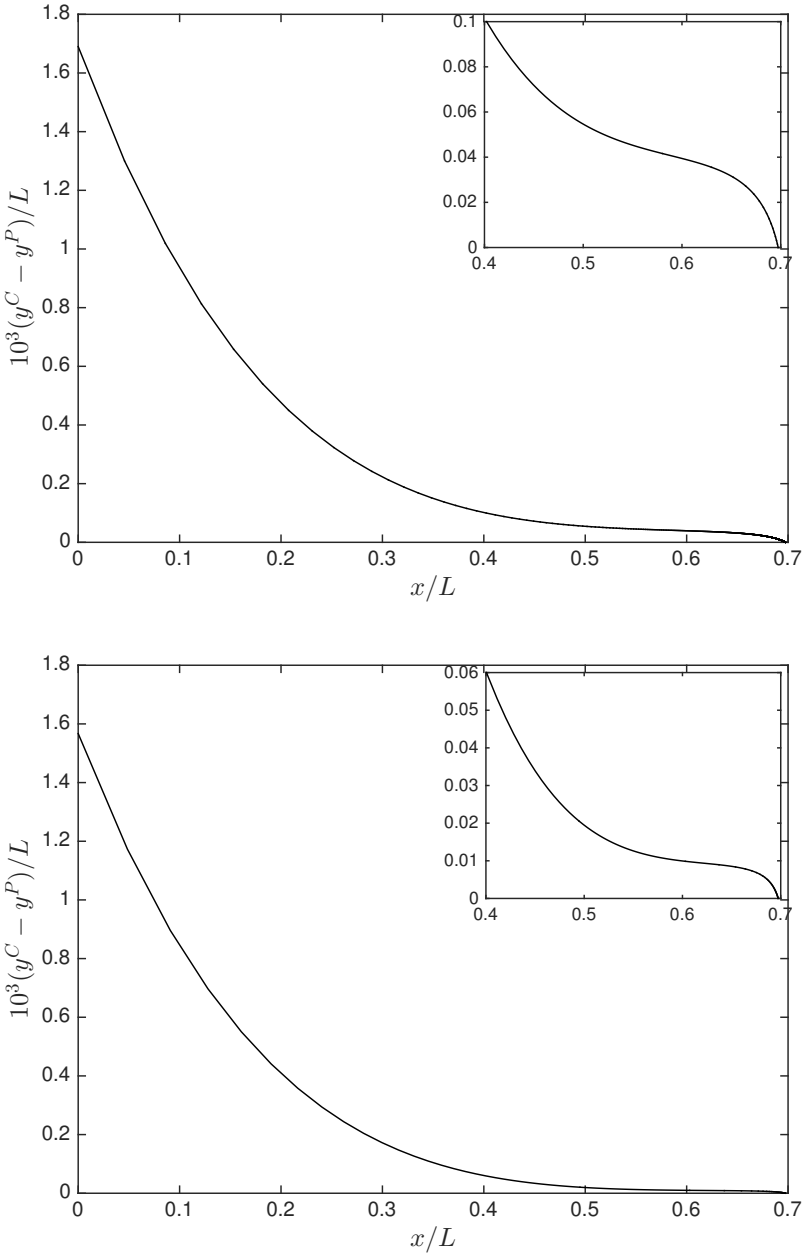

Figure 4.7: Composite expansion $(y^C - y^P)/L$ for $\theta = 5\pi/12$; (top) $Ca = 10^{-7}$,(bottom) $Ca = 10^{-8}$; we have subtracted parabolic interface to be able to see the structure at the tip. The inset scale is the same as the main figure axes. See text for the values of α and ϕ.

4.4 Later stage of tail formation in the limit $Ca \to 0$

Figure 4.8 shows the film to be coated with continuing motion of the substrate at a later stage. As shown in the control volume (C.V.), the mass exiting the C.V. is Uh_∞. When the radius of curvature of the meniscus is r, h_∞ is the film thickness to be coated at this instant; that film thickness is at a distance r away from the blade (assuming perfectly wetting case) where the interface slope is zero. The corresponding film thickness is given by $h_\infty = 1.34rCa^{2/3}$ (Landau and Levich, 1942). As the tip advances, however, the thickness of the film decreases with time because the volume of the meniscus is finite.

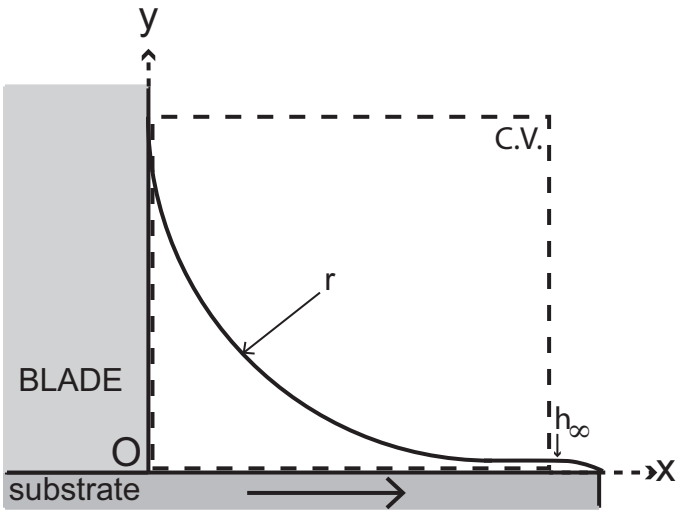

Figure 4.8: Coating of a Landau–Levich film.

Figure 4.9 shows the expected tail shape. From T to M, we expect the film thickness to increase from the inner analysis. To the left of M, the film thickness is controlled by the volume under the meniscus because the meniscus is coating the substrate.

Assume that at time t, the radius of curvature of the meniscus from which a thin film is coated be r. Here, r is not constant in time. The volume constraint, for arbitrary contact angle θ on the vertical blade, requires that

$$\frac{d}{dt}r^2\left\{\cos\theta\left(1-\frac{1}{2}\sin\theta\right)+\frac{\theta}{2}-\frac{\pi}{4}\right\}=-Uh_\infty=-1.34UrCa^{2/3}. \tag{4.26}$$

Using (4.26), time rate of change of the film thickness away from the bulk meniscus is found to be

$$\frac{dh_\infty}{dt}=\frac{(1.34)^2UCa^{4/3}}{2\left\{\cos\theta\left(1-\frac{1}{2}\sin\theta\right)+\frac{\theta}{2}-\frac{\pi}{4}\right\}}. \tag{4.27}$$

As the radius of curvature of the bulk meniscus decreases linearly in time, so does the coated

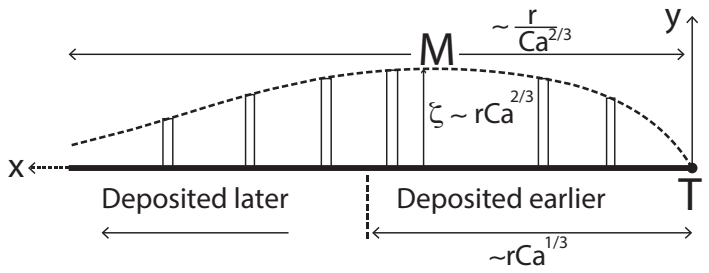

Figure 4.9: For a fixed point on substrate, expected tail formation.

film thickness. (4.27) is valid, in the limit as $Ca \to 0$, and when r changes slowly compared with either of the terms, h_∞ or $Ca^{2/3}$, in Landau–Levich equation. Gutenev et al. (2002) makes a similar analysis for liquid entrainment from the meniscus of a liquid wedge in the limit as $Ca \to 0$, but they do not consider the viscous effects.

The draining time of the mass scales as $t_d \sim rU^{-1}Ca^{-2/3}$; therefore the corresponding tail length scales like $\sim Ut_d \sim rCa^{-2/3}$.

4.5 Tail formation studied using numerical solution of Stokes equations with no cell

In the previous sections, we have demonstrated the physical picture. We now demonstrate using numerical solution that the physical picture is correct.

As shown in §3.3, for vanishing capillary number, there is no leakage into the cell: the interface touches the trailing edge of the cell and pins at the trailing edge of the cell. The meniscus is separated from the cell and printed with the continuing motion of the substrate.

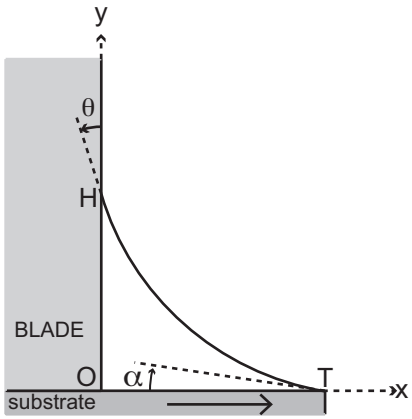

Figure 4.10: Geometry of the meniscus sitting between blade and trailing edge (T) of the cell.

Figure 4.10 shows the geometry of the meniscus printing problem. In this section we assume that the contact line is pinned at T and free to move at H. We solve the corresponding Stokes problem between points O and T with initial free surface profile predicted at the end of meniscus growth stage with $Ca = 0.001$, $\theta = \pi/6$ which is given in chapter 3.

Figure 4.11 shows the interface evolution with continuing motion of substrate for $\theta = \pi/6$. The interface rotates around the pinning point T at the trailing edge of the cell and starts coating a thin film downstream.

The static solution given by (4.1) and (4.2) predicts the meniscus printing problem closely until the trailing edge of the cell has advanced to about $0.1L$ from its initial location (at $x_0 = 0.4596L$). At the time when the trailing edge of the cell advances $x/L = 0.2$ from its initial position, the difference between static prediction and Stokes solution is visible close to the tip region with maximum absolute error of 0.004.

Figure 4.12 shows the tip region for the tip locations $(x_T - x_0)/L = 0.05, 0.1, 0.2$. The difference between Stokes solution and static prediction grows as the tip advances.

According to static prediction, α vanishes when the trailing edge of the cell has advanced by a distance of $0.2323L$ from its initial position. At this position, the maximum absolute error is 0.006. We plot the difference between the Stokes solution and the static prediction when the trailing edge of the cell advances $x/L = 0.23$ from its initial position, and compare

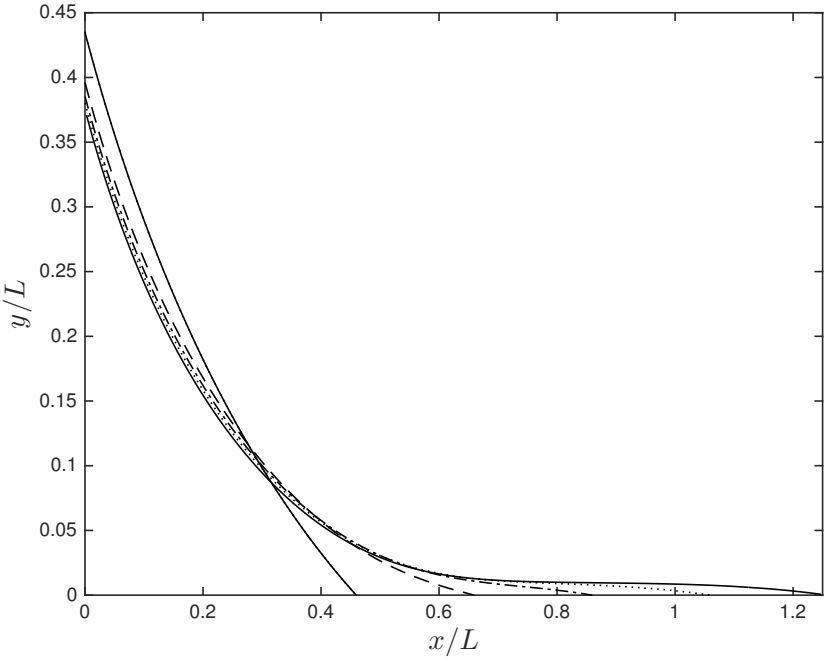

Figure 4.11: Time evolution of meniscus printing computed using Stokes equations, $Ca = 0.001$, $\theta = \pi/6$.

it with the inner viscous solution in figure 4.12. From static prediction, $\alpha = 0.0029$ and $r = 0.799$. Inner solution predicts the solution closely for x/L up to 0.02. As the contact angle θ over the blade is decreased, the difference between the two reduces. Figure 4.13 shows the corresponding comparison for $\theta = 5\pi/12$. In this case, $\alpha_0 = 0.13011$, and α vanishes when T advances $x/L = 0.20877$ away from its initial position, therefore we give the results for the time when T advances $x/L = 0.2$ away from its initial position. The inner prediction approaches the Stokes solution as θ is increased. For $\theta = \pi/6$, the inner solution predicts Stokes solution closely up to $x/L = 0.03$ away from the tip, on the other hand, for $\theta = 5\pi/12$, the corresponding value of x/L is approximately 0.1. It is expected that as $\theta \to \pi/2$, and $\alpha \to 0$, this range is going to increase because the parabolic interface approximates the circular arc interface closely away from the tip as $\theta \to \pi/2$. From figures 4.12,4.13 and 4.14, we observe that the interface is pushed upwards as predicted from the inner analysis in §4.2.

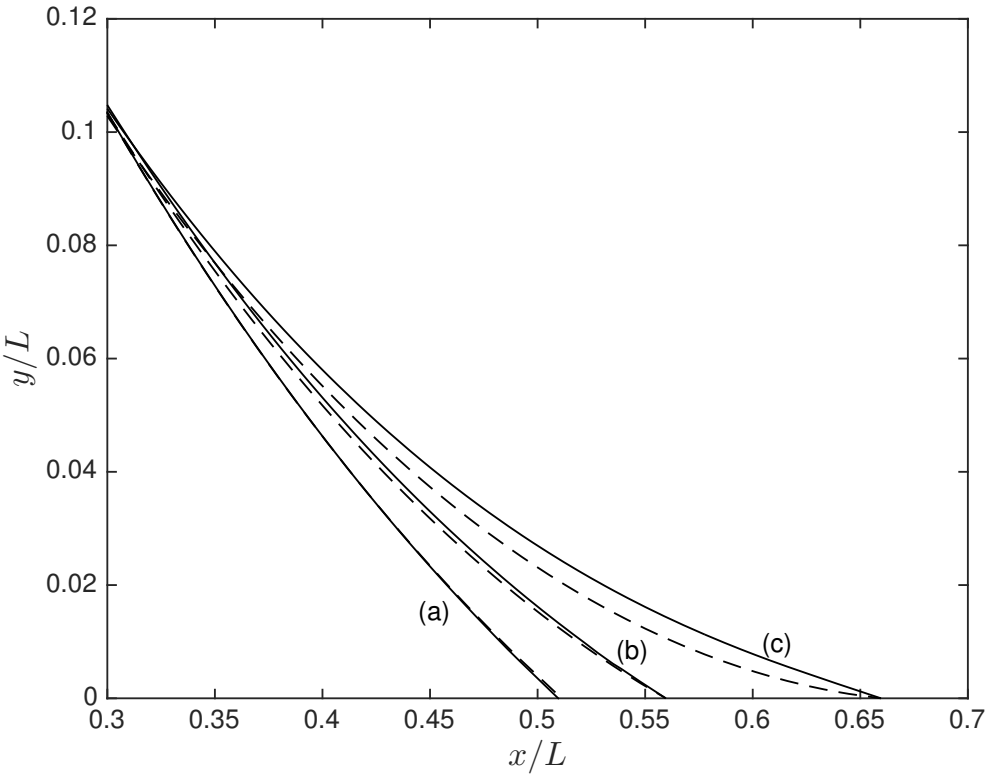

Figure 4.12: Comparison of the static prediction and Stokes solution of meniscus printing problem, $Ca = 0.001$, $\theta = \pi/6$: (a) $x/L = 0.5096$, (b) $x/L = 0.5596$, (c) $x/L = 0.6596$; (—) Stokes solution, (- - -) static prediction.

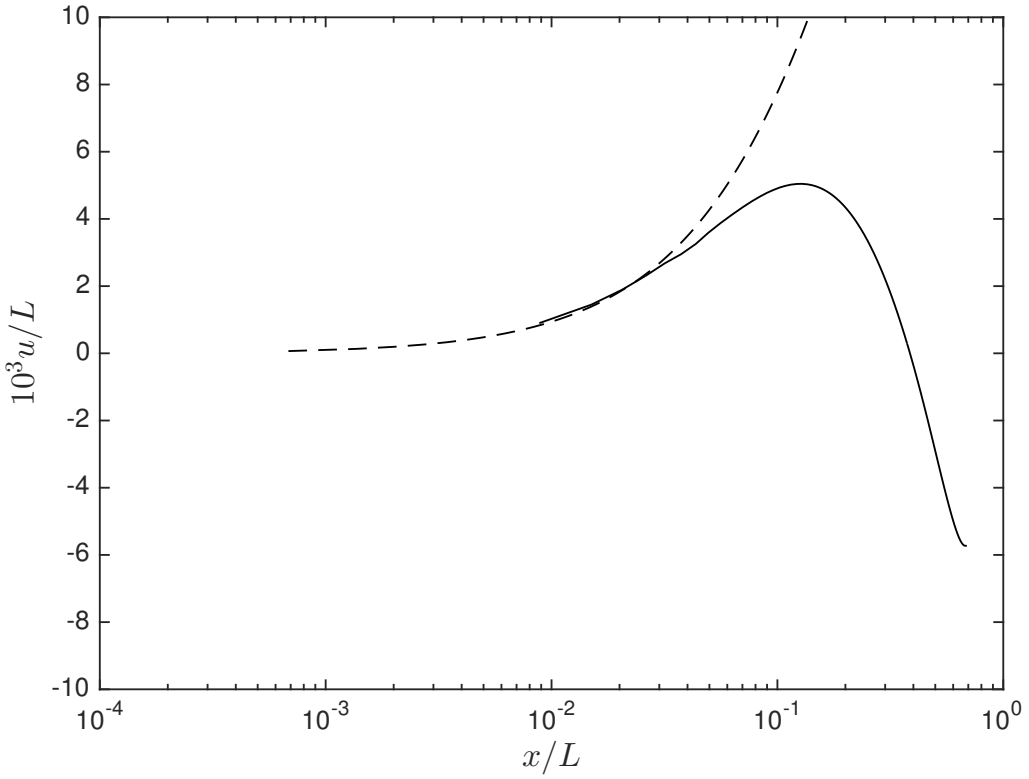

Figure 4.13: Comparison of the inner viscous solution and Stokes solution. - - -: inner solution solution, —: the difference u/L between Stokes solution and static prediction at the corresponding time. Inner solution is obtained using α and x/L corresponding to Stokes problem solved for $Ca = 0.001$, $\theta = \pi/6$, $x/L = x_0/L + 0.23$.

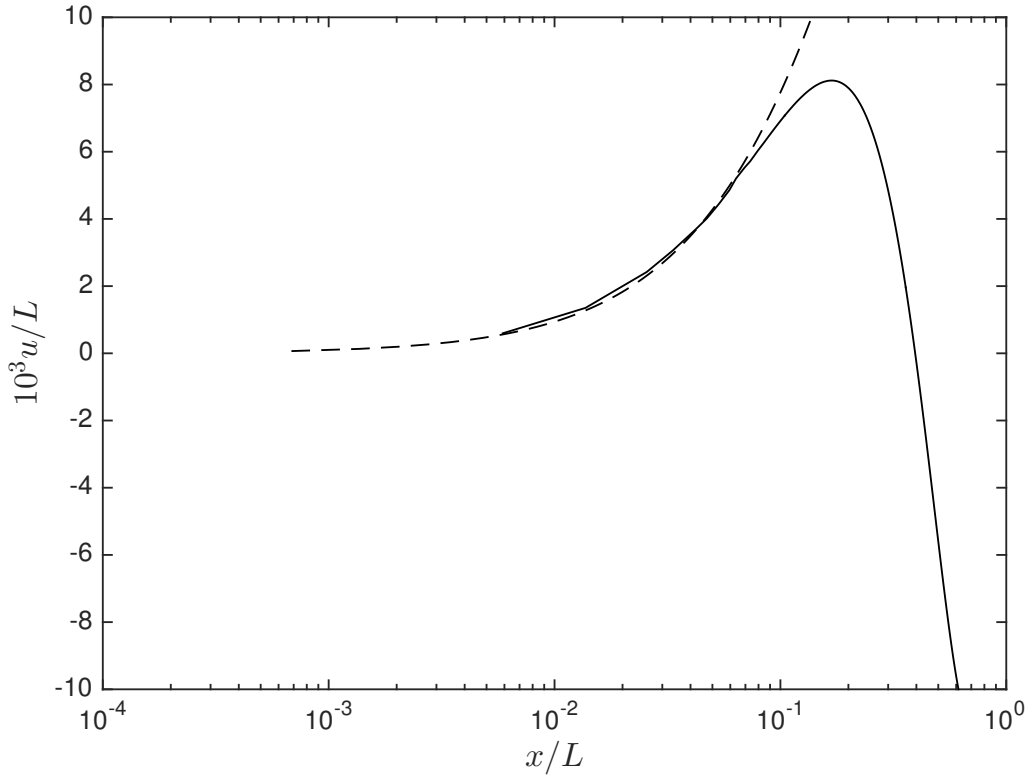

Figure 4.14: Comparison of the inner viscous solution and Stokes solution. - - -: inner solution, —: the difference u/L between Stokes solution and static prediction at the corresponding time. Inner solution solution is obtained using α and x/L corresponding to Stokes problem solved for $Ca = 0.001$, $\theta = 5\pi/12$, $x/L = x_0/L + 0.2$.

4.6 Tail formation studied using numerical solution of Stokes equations with cell

As Ca increases, the no–leakage back into the cell assumption is not valid. Now we include the cell: The difference from the meniscus printing problem is that the flow domain includes the cell as well because the interface does not touch the trailing edge of the cell at the location predicted in the hydrostatic analysis (§3.2) and the leakage is shown in §3.3. Figure 4.15 shows the domain of the problem. The interface shape is determined as part of the solution. We continue integrating the problem from the point when the cell has emerged fully beneath the blade (figure 4.15a) by taking the interface shapes given in chapter 3.

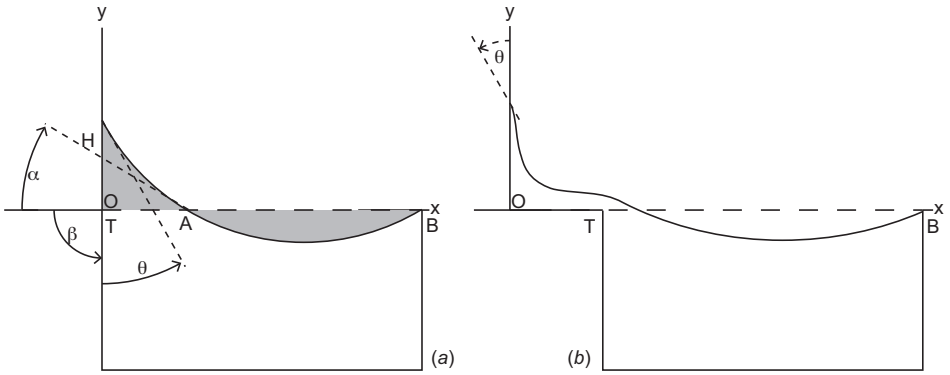

Figure 4.15: Geometry of the domain for tail formation problem, cell translating rightwards beneath a stationary blade occupying the second quadrant of the xOy plane: (a) cell fully emerged; (b) cell is away from the blade.

In figure 4.16, the evolution of the interface into a tail shape for $Ca = 0.1$ is plotted. For each time step, each curve is overlaid relative to the horizontal distance of the leading edge of the cell to the blade. The history of the interface profiles are plotted starting from $t = 1$ to $t = 1.7$ with $\Delta t = 0.1$ increments. As shown by the inset in figure 4.16, the contact line on the blade retreats while evolving into a tail shape. The drag due to substrate motion pulls the meniscus down as shown with the corresponding streamlines for x_T/L=0.2,0.4 and 0.6 in figure 4.17; the free surface evolves into a tail shape.

For relatively large Ca numbers, tail formation occurs faster. In figure 4.18, we show the interface profiles for Ca numbers of 0.1, 0.5 and 1. We show the interfaces at the times when the minimum film thickness behind the tail is 0.01. This occurs when the trailing edge of the cell is 0.091, 0.219 and 0.85 away from the blade for Ca=1, 0.5 and 0.1, respectively. The horizontal is scaled with the horizontal distance of the leading edge of the cell to the blade. The tail forms faster as Ca is increased and tail length grows as Ca is reduced. This is consistent with the analysis given in chapter 3 because less liquid is trapped under the meniscus as Ca increases.

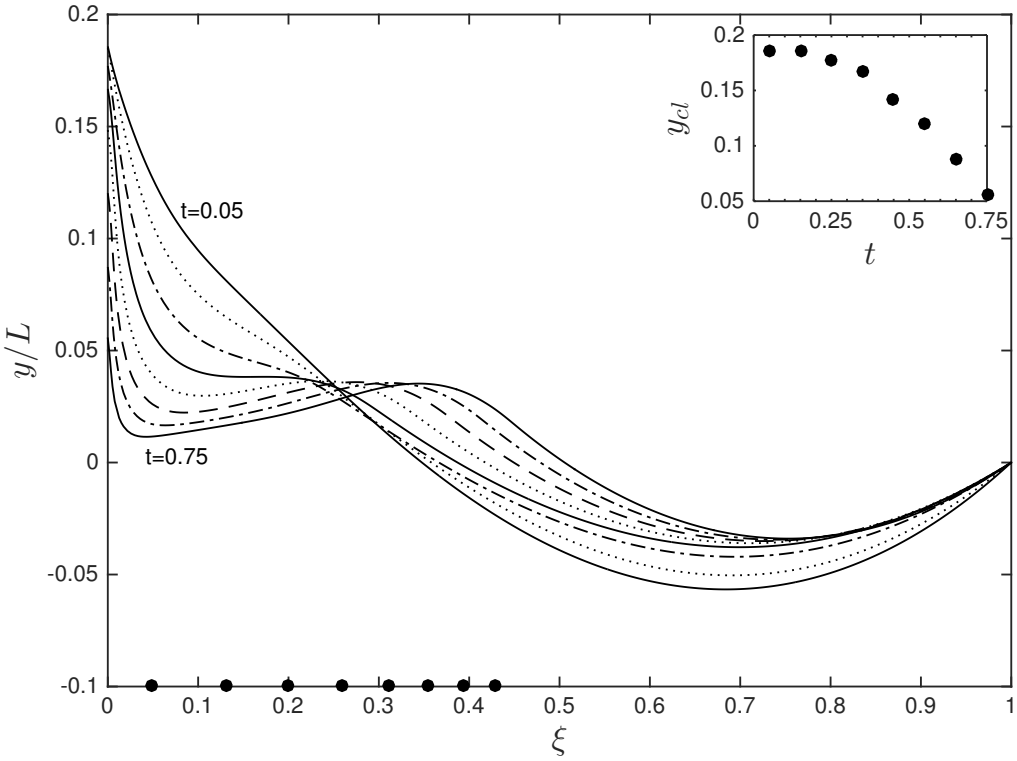

Figure 4.16: Interface evolution into tail shape for $Ca = 0.1$, $\theta = \pi/6$. The history of the interface profiles are plotted starting from x_T/L=0.05 to x_T/L=0.75 with 0.1 increments. Each curve is overlaid relative to the distance of leading edge of the cell to the blade. Solid circles along ξ axis show the corresponding location of the trailing edge of the cell: $\xi = 0.0476, 0.1304, 0.2, 0.2593, 0.3103, 0.3548, 0.3939, 0.4286$, respectively.

As Ca is decreased below $Ca = 0.1$, on the other hand, the interface approaches the trailing edge of the cell as it translates further away. This slows down the computations in terms of meshing of the domain and computational effort spent within the cell. When the interface is almost touching the trailing edge of the cell, we cut the cell from computational domain, pin the interface at T and continue integrating in time. After this point, we can treat the problem as meniscus printing which occurs between points O and T as shown in figure 4.10. In figures 4.19 and 4.20, comparison of the interface profiles for $Ca = 0.025, 0.01$ and 0.005 at $t = 1.773$ and $t = 2.368$ shows that tail formation takes longer for smaller Ca. As Ca is increased, the interface rotates faster and the interface slope away from the pinned contact line reaches zero and after this point maximum formation occurs. In all three cases, maximum formation is visible in figure 4.20. We should note that tail thickness decreases linearly as predicted in (4.27); the mass under the meniscus is used to coat the tail. In figure 4.21, for a fixed point away from the blade, we plot the change of film thickness with time

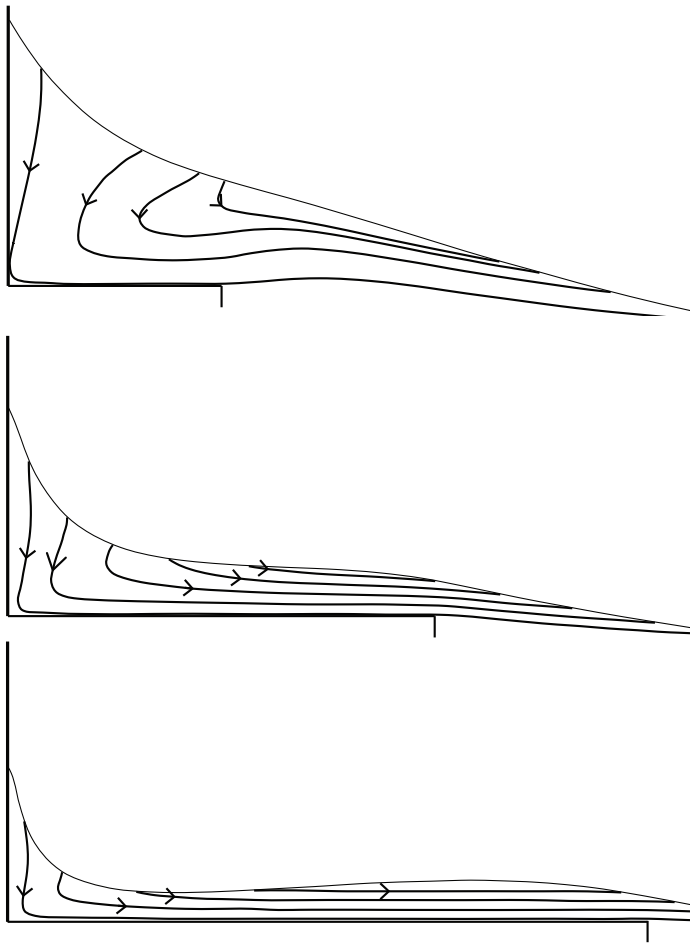

Figure 4.17: Streamlines corresponding to figure 4.16, x_T/L=0.2,0.4 and 0.6.

for $Ca = 0.025, 0.005$. The slope of the line for $Ca = 0.025$ is -0.0196. According to (4.27), corresponding slope is -0.0521. The corresponding slope for $Ca = 0.005$ is -0.0043; (4.27) predicts the corresponding slope to be -0.0061. Though (4.27) over–predicts the slope, as Ca is decreased, the prediction approaches the numerical solution.

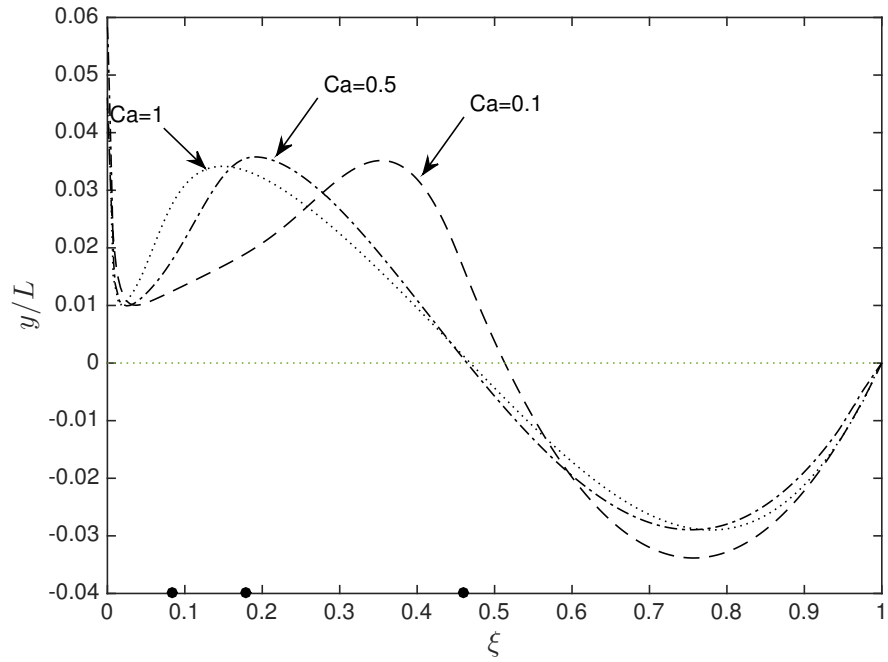

Figure 4.18: Interface shape at the instant the minimum film thickness behind the tail is 0.01. Curves are for Ca=1,0.5 and 0.1. Each curve is overlaid relative to the distance of leading edge of the cell to the blade. Solid circles along ξ axis show the corresponding location of the trailing edge of the cell: $\xi = 0.0834, 0.1797, 0.4595$, respectively.

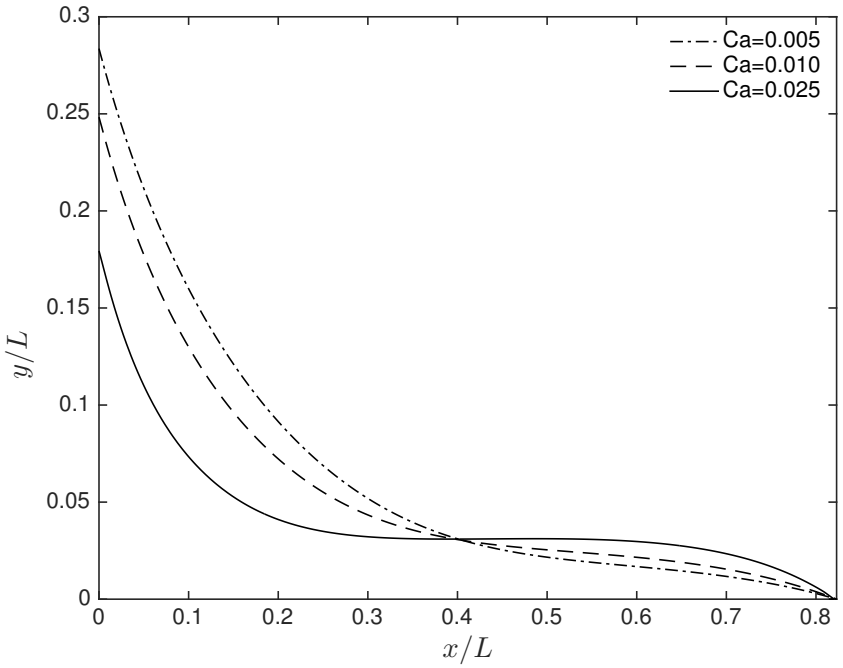

Figure 4.19: Comparison of interface profiles computed from the Stokes equations for $Ca = 0.025, 0.01$ and 0.005 at $t = 1.773$.

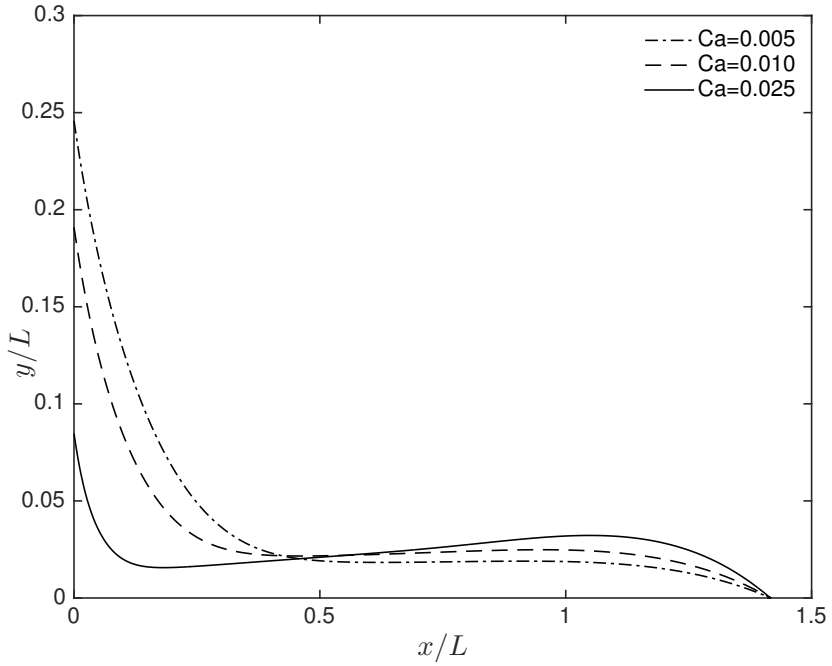

Figure 4.20: See caption for figure 4.19, $t = 2.368$.

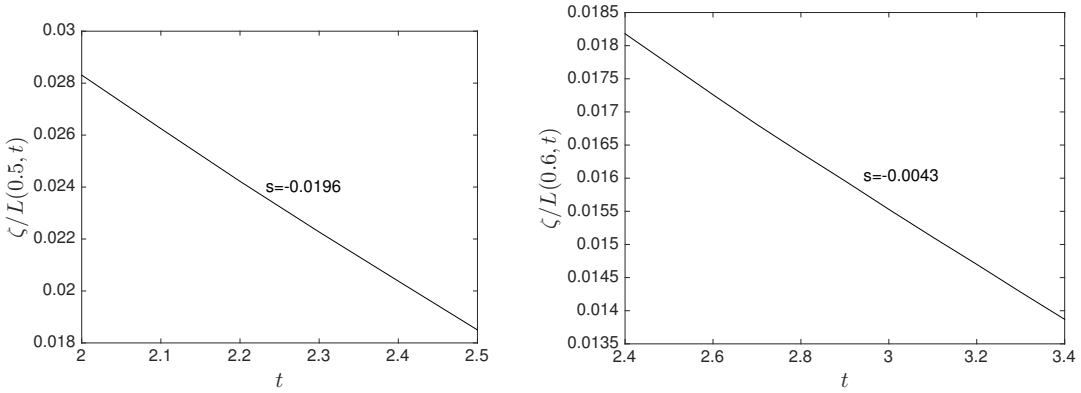

Figure 4.21: Change of film thickness with time at (left)$x = 0.5L$ away from the blade, Ca=0.025, (right)$x = 0.6L$ away from the blade, Ca=0.005; s is the slope of the line; $\theta = \pi/6$.

4.7 Lubrication analysis

The analysis made in § 4.1, 4.2, 4.3 and 4.4 requires Ca to be small. The comparison of this analysis with small Ca Stokes solution is difficult because any numerical error on the interfacial force computations given by the last term in (2.13) is multiplied by Ca^{-1}; when Ca is small, this computations require the time step to be extremely small as the time integration is made explicitly. This results in a computationally expensive method. If the lubrication model of the problem, however, captured the smearing problem, the use of this model for small slope interface would be computationally much cheaper than solving the corresponding Stokes problem. With this motivation, in this section, we formulate a lubrication model of tail formation problem.

When the interface slope is small, lubrication theory holds throughout the entire liquid film. By deriving the Reynolds equation for the film evolution, in § 4.7.1, we compare the lubrication model of tail formation with the corresponding Stokes problem. In §4.7.2, we formulate a lubrication model of meniscus printing problem to be able to show that as Ca is decreased, inner and outer structures exist. Lastly, in § 4.7.3, we consider the effect of a sequence of cells.

4.7.1 A model for smear formation including the cell

Figure 4.22 shows the geometry of the model. The coordinate axes are fixed in the stationary blade; the substrate velocity is $U\boldsymbol{e}_x$ and y–axis is perpendicular to the plane of the substrate, with $y = 0$ on the base of the cell. On the free surface $y = \zeta(x, t)$; on the solid–liquid interface $y = g(x, t)$.

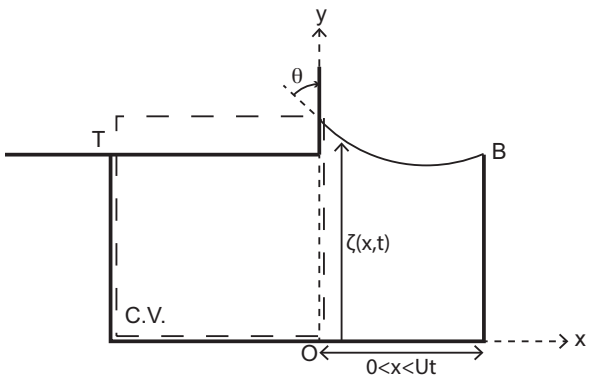

Figure 4.22: Schematic of a cell emerging beneath the stationary blade used in the lubrication analysis of tail formation.

As shown in figure 4.22, the cell emerges from beneath the wiper blade. Because liquid wets the blade, the meniscus rises over the blade surface; the necessary liquid is supplied by the cell. Mass conservation requires the free surface to rearrange itself: the contact line at $x = 0$ rises over the blade, whilst the film thins over the cell during meniscus growth

process. After the cell has emerged fully from beneath the blade, drag is introduced due to the change in topography. The substrate motion pulls the meniscus down on the blade. The liquid retained in the meniscus is printed as a tail later in time.

We allow the contact line on the blade to move freely with a predefined static contact angle θ. We are assuming that, because the capillary number based on substrate velocity is small, so too is that based on the contact line velocity. We show in Chapter 3, figure 3.3 that as Ca is reduced, the contact line velocity approaches the hydrostatic prediction. The contact line on the leading edge of the cell is pinned at the corner of the cell.

The volume flow rate

$$\boldsymbol{q} = \int_g^\zeta (v_x \boldsymbol{e}_x + v_y \boldsymbol{e}_y)\, dy \tag{4.28}$$

is related to the film thickness $(\zeta - g)$ by the mass balance:

$$\frac{\partial(\zeta - g)}{\partial t} + \boldsymbol{\nabla} \cdot \boldsymbol{q} = 0. \tag{4.29}$$

The gradient operator in the xOy plane is defined by $\boldsymbol{\nabla} = \boldsymbol{e}_x \frac{\partial}{\partial x} + \boldsymbol{e}_y \frac{\partial}{\partial y}$.

In the lubrication approximation, $\boldsymbol{q}$ is related to dynamic viscosity η. liquid pressure p and film thickness $\zeta - g$ by

$$\boldsymbol{q} = -\frac{1}{2\eta} (\zeta - g)^3 \boldsymbol{\nabla} p + U (\zeta - g) \boldsymbol{e}_x. \tag{4.30}$$

This relation holds provided no–slip condition holds at the substrate liquid interface, and the shear stress vanishes on an interfacial element: provided the interface slope is small,

$$-p = \gamma \nabla^2 \zeta. \tag{4.31}$$

Our point here is to describe the tail formation mechanism without complication. Because of this reason, we do not include disjoining pressure. Eliminating p and $\boldsymbol{q}$ and then using the identity $\frac{\partial g}{\partial t} + U \frac{\partial g}{\partial x} = 0$, we obtain the Reynolds equation for ζ:

$$\frac{\partial \zeta}{\partial t} + U \frac{\partial \zeta}{\partial x} + \frac{\gamma}{3\eta} \boldsymbol{\nabla} \cdot \left\{ (\zeta - g)^3 \boldsymbol{\nabla} \nabla^2 \zeta \right\} = 0. \tag{4.32}$$

The film is parametrically forced by the cell; in (4.32), this effect is represented by the function g in the third term. We define the cell function by arctan as in Stillwagon and Larson (1988), but moving with speed U;

$$g(x,t) = d \left\{ \frac{1}{2} + \frac{1}{\pi} \arctan\left(\frac{-x - L + Ut}{L\epsilon} \right) \right\} \tag{4.33}$$

where L is the length, d is the depth of the cell, and ϵ is the edge smoothness parameter.

In the model problem, (4.32) holds in the domain $0 < x < Ut$; in that domain g varies between zero and d according to its definition. The initial condition for the interface

shape is determined by the power series expansion of the governing equation which holds for arbitrarily small length $Ut \to 0$. For $t > 0$, two boundary conditions are applied at $x = 0$. First, we allow the contact line to move freely with a predefined contact angle at $x = 0$:

$$\frac{\partial \zeta}{\partial x} = -\cot\theta. \tag{4.34}$$

The second boundary condition at $x = 0$ is obtained by a mass balance on the control volume shown in figure 4.22. This is the key boundary condition that allows us to determine the location of the meniscus on the blade as part of the initial boundary value problem. Because the trailing edge of the cell acts as a piston displacing to the right, the incoming flow to the control volume is $U(d - g)$; and this inflow rate is equal to the axial flux across the interface at $x = 0$:

$$U(d-g) = U(\zeta - g) + \frac{\gamma}{3\eta}\left\{(\zeta - g)^3 \frac{\partial^3 \zeta}{\partial x^3}\right\}, \tag{4.35}$$

simplifying, we find that at $x = 0$

$$\frac{\partial^3 \zeta}{\partial x^3} = -3Ca\frac{\zeta - d}{(\zeta - g)^3}. \tag{4.36}$$

Equation (4.36) holds throughout the process. When g jumps from zero to d, the incoming flux is zero and same equation applies after the cell has emerged fully from beneath the blade. At $x = Ut$, we pin the contact line the upper corner of the leading edge of the cell:

$$\zeta = d, \tag{4.37}$$

and continuity of volume flow rate requires pressure gradient to vanish there:

$$\frac{\partial^3 \zeta}{\partial x^3} = 0. \tag{4.38}$$

This ends the problem statement.

Because the cell is moving, we solve the problem using a stretched domain which is fixed. To do so, we define new variables: $\zeta = df(\xi, t')$ where $\xi = x/(Ut)$ and $t' = Ut/dCa^{1/3}$. The dimensionless Reynolds equation (4.32) in terms of the new variables is valid for $0 < \xi < 1$ and given by

$$3t'\left\{t'\frac{\partial f}{\partial t'} + (1-\xi)\frac{\partial f}{\partial \xi}\right\} + \frac{\partial}{\partial \xi}\left\{(f - g')^3 \frac{\partial^3 f}{\partial \xi^3}\right\} = 0. \tag{4.39}$$

The corresponding boundary conditions at $\xi = 0$ are

$$\frac{\partial f}{\partial \xi} = -t' Ca^{-1/3}\cot\theta, \tag{4.40}$$

$$\frac{\partial^3 f}{\partial \xi^3} = -3t'^3 \frac{f-1}{(f-g')^3}. \tag{4.41}$$

At $\xi = 1$:

$$f = 1, \tag{4.42}$$

$$\frac{\partial^3 f}{\partial \xi^3} = 0. \tag{4.43}$$

The dependent variable f can be expanded as a power series in t' whose coefficients are functions of ξ only. Initially $f = 1$ and (4.40) requires the next term in the expansion to vary as t', so $f = 1 + A(\xi)t' + ...$ Then (4.41) requires the next term to vary as t'^4:

$$f = 1 + A(\xi)t' + B(\xi)t'^4 + ... \tag{4.44}$$

Substituting the power series (4.44) into (4.39), then equating to zero the coefficients of successive powers of t', we obtain boundary value problems for the coefficients A and B. Solving for A and B, we obtain

$$A(\xi) = \frac{1}{4} Ca^{-1/3} \cot\theta \left(3\xi - 1\right)\left(\xi - 1\right), \tag{4.45}$$

$$B(\xi) = Ca^{-1/3}\cot\theta \left(\frac{1}{160}\xi^6 - \frac{9}{240}\xi^5 + \frac{9}{96}\xi^4 - \frac{1}{8}\xi^3 + \frac{15}{224}\xi^2 - \frac{1}{224}\right). \tag{4.46}$$

At $O(t')$, the meniscus rises linearly in time in order to satisfy contact angle condition (4.40), and the volume constraint requires A to change sign within the interval $0 < \xi < 1$. This is explicitly shown in (4.45). Growth slows when the dimensional time $t \sim \frac{d}{5U} Ca^{-1/3}$; for times of this order, the two terms in the expansion (4.44) are comparable.

Here, we should be careful about the influx boundary condition at $x = 0$ which is applied to the lubrication region downstream. The existence of blade at $x = 0$ requires the Stoke's solution within a region of $O(d)$ to impose the impermeability on the blade. However, the lubrication approximation computes the axial component of the velocity, so the motion of the contact line on the blade is determined by the continuity equation, and it does not see the no–slip condition on the blade. With small slope assumption, however, the vertical velocity is small compared with horizontal velocity; so it is expected that this Stokes region is small compared with horizontal scale within which the lubrication equation is solved. The power series expansion is a useful tool to prove this claim. The expansion to $O(t'^4)$ is good approximation up to $t' \sim 2$, at that time the contact line is at $O(d)$, whereas the film length is $\sim 2dCa^{-1/3} >> d$. Imposing the inflow condition to the inlet of the lubrication model is self–consistent.

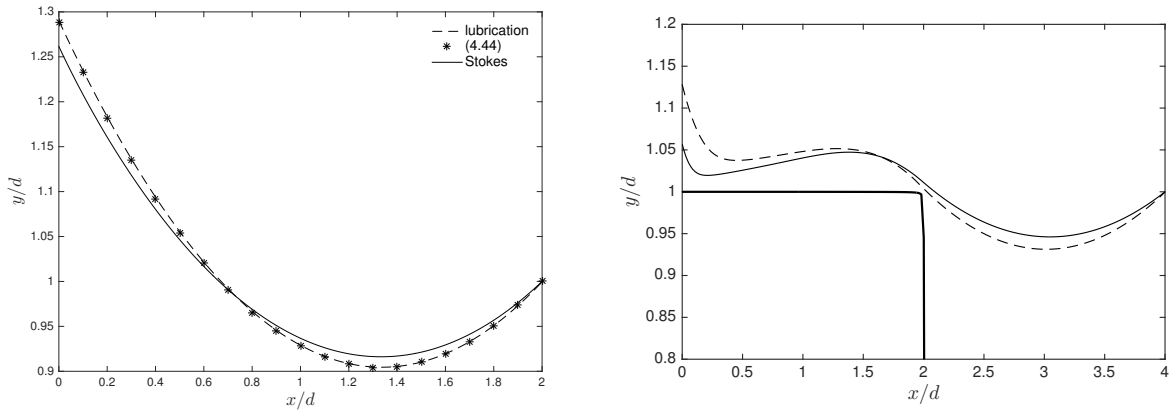

(a) cell has emerged fully

(b) T is x/d=2.0 away from the blade($x = 0$)

Figure 4.23: Comparison of lubrication model and the numerical solution of the Stokes problem, $Ca = 0.01$, $\theta = \pi/3$. The power series expansion uses two terms in (4.44). The bottom of the cell is at $y = 0$.

We integrate the equations in time implicitly and employ a positivity preserving scheme for the diffusion coefficient (Zhornitskaya and Bertozzi, 2000). Details of the numerical method is given in Appendix A. We set $Ca = 0.01$, $\theta = \pi/3$, $\epsilon = 0.0001$, $L/d = 2$. In figure 4.23, we compare the interface profiles at two different times. Figure 4.23a is at the time when the cell emerges fully from beneath the blade. Lubrication theory closely captures the interface profile. As shown by the Stokes solution, the lag in contact line velocity compared to the hydrostatic prediction causes the meniscus to rise below the lubrication prediction as expected. Tail formation is shown in figure 4.23b. The competition between convection and capillary pressure determines the axial flux gradient. Depending on the sign of this gradient, the interface evolves into a tail shape. Lubrication theory over–predicts tail formation for the reasons stated above.

4.7.2 Model for meniscus printing

As contact angle approaches $\pi/2$, the lubrication model predicts the meniscus printing problem very closely. This provides us to solve the problem at low Ca, to compare the results with the composite expansion given in § 4.3 and to show that the film thickness coated away from the bulk meniscus is consistent with the Landau-Levich film thickness. In this section, we first formulate the lubrication model of the meniscus printing problem and show that lubrication model captures the solution very closely compared with the corresponding Stokes solution. We then use the lubrication model for smaller Ca.

In the lubrication regime, we solve the evolution equation now between points O and T. Figure 4.24 shows the geometry of the model. Coordinate is fixed on the wiper blade; the substrate velocity is $U\boldsymbol{e}_x$ and y-axis is perpendicular to the plane of substrate, with $y = 0$

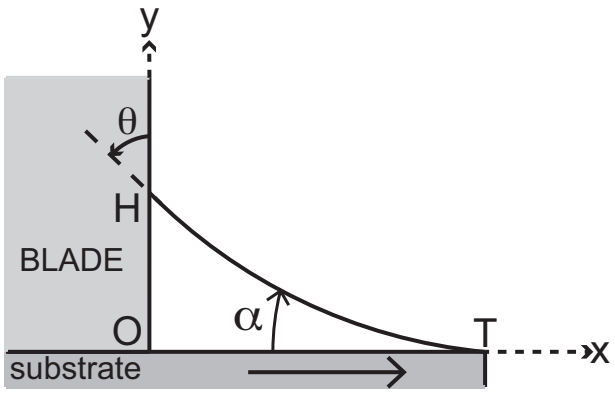

Figure 4.24: Geometry of meniscus printing problem

on the land and the trailing edge of the cell is at $x_0 + Ut$. On the free surface, $y = \zeta(x,t)$ and it is initially a circular arc profile, obtained using the relations given in Chapter 3. The interface evolution is governed by (4.32), however because we have no longer a cell, $g = 0$; the corresponding Reynolds equation is given by,

$$\frac{\partial \zeta}{\partial t} + U\frac{\partial \zeta}{\partial x} + \frac{\gamma}{3\eta}\boldsymbol{\nabla}\cdot\left\{\zeta^3\boldsymbol{\nabla}\nabla^2\zeta\right\} = 0. \tag{4.47}$$

The slope condition at $x = 0$ is the same as in (4.34). The flux condition at $x = 0$ differs from (4.35) and it is given by

$$U\zeta + \frac{\gamma}{3\eta}\left\{\zeta^3\frac{\partial^3\zeta}{\partial x^3}\right\} = 0, \tag{4.48}$$

simplifying, we find that at $x = 0$

$$\frac{\partial^3\zeta}{\partial x^3} = -3Ca\zeta^{-2}. \tag{4.49}$$

At $x = x_0 + Ut$, we pin the contact line to the upper corner of the trailing edge of the cell:

$$\zeta = 0, \tag{4.50}$$

and the continuity of volume flow rate requires the pressure gradient to vanish there:

$$\frac{\partial^3\zeta}{\partial x^3} = 0. \tag{4.51}$$

We integrate the meniscus printing problem over a fixed domain by defining the following variables: $\zeta = x_0 f(\xi, t')$, $\xi = x/(x_0+Ut)$ and $t' = (x_0+Ut)/x_0Ca^{1/3}$. The numerical method of integration is same as used for (4.39) to (4.43).

In figure 4.25, we compare the lubrication solution and Stokes solution of the meniscus printing problem for a case in which we set $Ca = 10^{-3}$, $\theta = 5\pi/12$. The interface profiles are

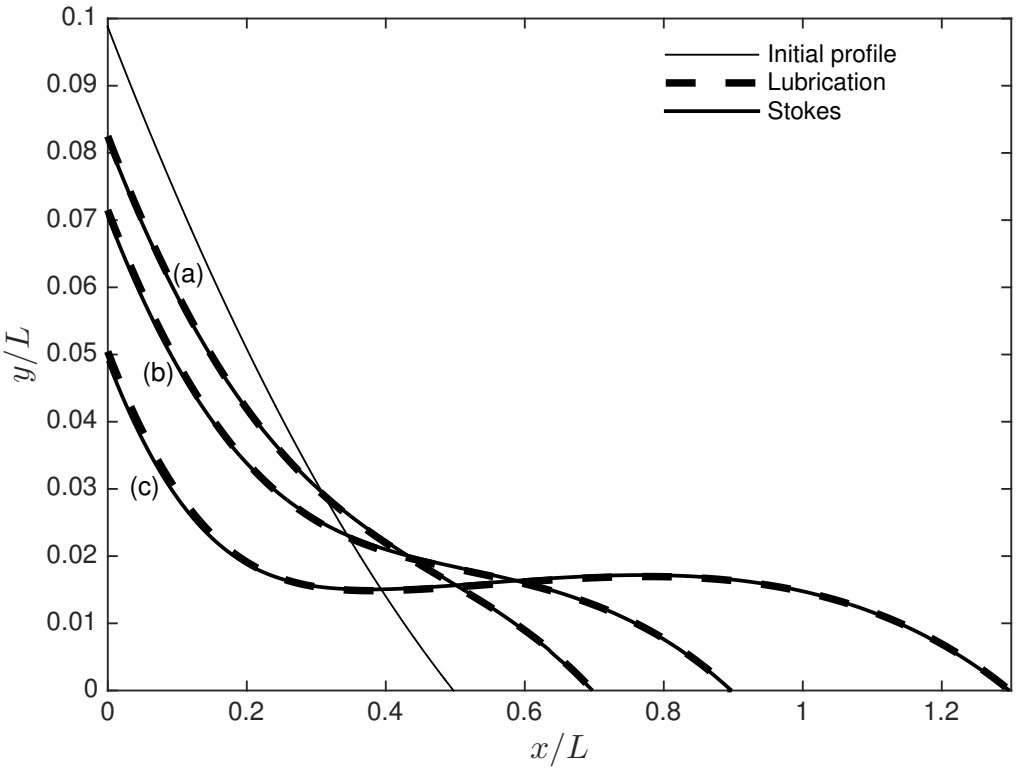

Figure 4.25: Comparison of the meniscus printing problem obtained from lubrication model and Stokes solution, Ca=0.001, $\theta = 5\pi/12$, (a) tip advanced $x/L = 0.2$ away from its initial position (solid line), (b) tip advanced $x/L = 0.4$ away from its initial position, (c) tip advanced $x/L = 0.8$ away from its initial position.

graphically the same when the trailing edge of the cell advances $x/L = 0.2$, $x/L = 0.4$ and $x/L = 0.8$ away from its initial position. The pressure distributions under the film along the interface agree as well. The pressure gradient close to the blade is not zero because separation of length scales does not exist at this capillary number; the film thickness is comparable to the meniscus height. Solving the corresponding Stokes problem for lower capillary numbers is not practical, at least with the current version of our solver. However, because the lubrication model agrees with the Stokes solution as shown in figure 4.25, we are able to solve (practically) a corresponding lubrication problem for lower Ca numbers.

With this motivation, we solve the lubrication model for $Ca = 10^{-8}$, $\theta = 5\pi/12$. In figure 4.26, we compare the lubrication solution of meniscus printing problem with composite expansion given in § 4.3 at the time when α drops to 0.00327. Within the inner region when $x << 1$, the ratio $\hat{\zeta}/(\alpha x)$ scales like $\sim \alpha Ca^{-1/3}$. For $Ca = 10^{-8}$, this corresponds to $\alpha Ca^{-1/3} \sim 1.5$, therefore $\hat{y}$ is not small. As shown in figure 4.26, the composite expansion agrees with the interface profile obtained from the lubrication model.

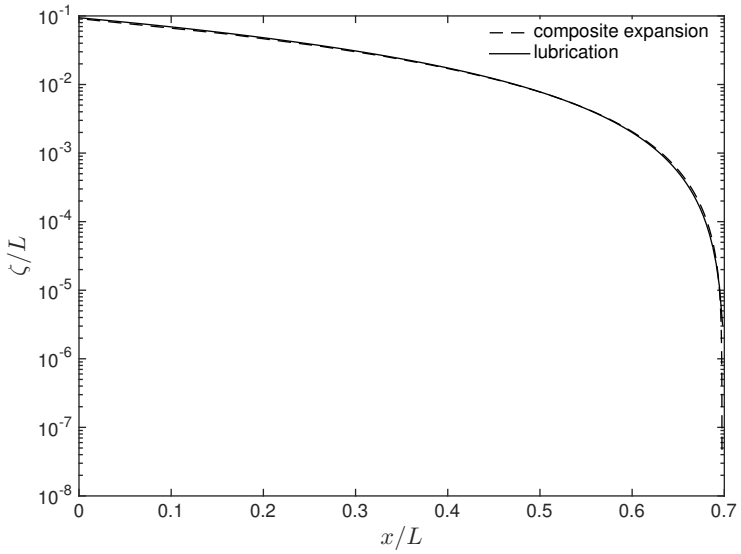

Figure 4.26: Comparison of lubrication solution of meniscus printing problem with composite expansion, $Ca = 10^{-8}$. This comparisons are made at the time when α drops to 0.00327.

Finally in this section, we solve a meniscus printing problem for $Ca = 10^{-5}$, $\theta = \pi/12$ and integrate the Reynolds equation in time until the trailing edge of the cell advances $x/x_0 = 1$ away from its initial position. Figure 4.27 shows the interface profile and the corresponding pressure distribution under the film. The pressure gradient drops to zero towards the blade showing that the outer profile remains a circular arc. The pressure distribution is different from Landau–Levich; in that case the pressure goes to zero away from the meniscus, but here the pressure is positive and highest at the tip due to squeeze film flow. Pressure ranges from $\sim -7 \times 10^4$ (static meniscus) to 1.6×10^4(squeeze film). The radius of curvature of the outer problem is $r_0 = 2.728$. The maximum thickness of the film away from the bulk meniscus is 0.00154. This thickness is consistent with the Landau–Levich coating film thickness which scales like $1.34 r_0 Ca^{2/3}$.

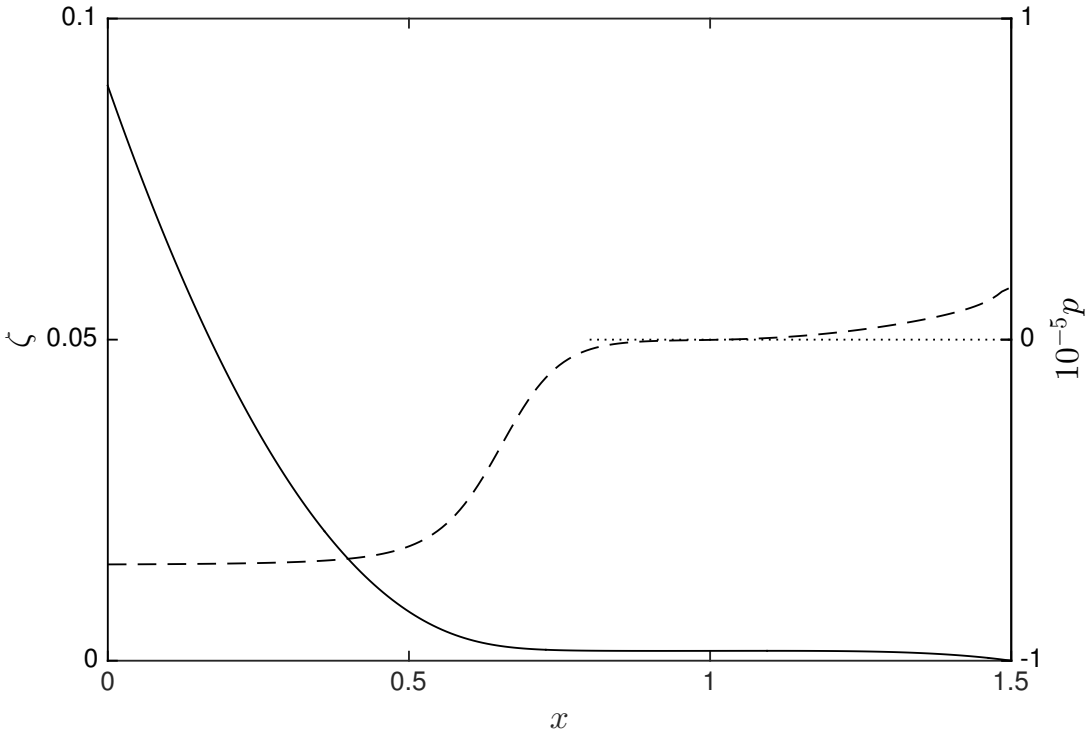

Figure 4.27: Interface profile when the tip advances $x/x_0 = 1$ away from its initial position, $Ca = 10^{-5}$, $\theta = 5\pi/12$, (solid line) interface profile, (dashed line) corresponding pressure distribution.

4.7.3 Effect of a sequence of cells on tail formation

One way of reducing the tail formation could be by adding sequence of cells. To show the effect of multiple cells, we add a second cell into the domain by modifying the cell function in the stretched domain as follows:

$$g'(\xi,t') = 1 + \frac{1}{\pi}\left(atan\left(\frac{-\xi - \frac{L}{dt'} + 1}{L/d\epsilon}t'\right) + atan\left(\frac{\xi - 1}{L/d\epsilon}t'\right)\right)$$
$$+\frac{1}{\pi}\left(atan\left(\frac{-\xi - \frac{L}{dt'} - \frac{sL}{dt'} + 1}{L/d\epsilon}t'\right) + atan\left(\frac{\xi + \frac{sL}{dt'} - 1}{L/d\epsilon}t'\right)\right). \quad (4.52)$$

In figure 4.28, we plot the film shape at $t' = 20$ for cell spacings $L/2$ and L. A cell spacing of cell length produces a film of almost the same thickness as the tail thickness behind the second cell. However, when the cell spacing is halved, i.e., $L/2$, the thickness of the film above the spacing is small compared with the the tail thickness behind the second cell, $\sim$ 1/5 th of the thickness. For $L/4$, the film almost follows the pattern of the land in between. We should note that the drag–out is the same from both of the cells.

As we add more cell in the sequence, the liquid accumulates under the meniscus as the cells translates away from the blade (see figure 4.29) and as there must be an end to the sequence of cells, smearing still exists behind the last cell in the sequence in this configuration.

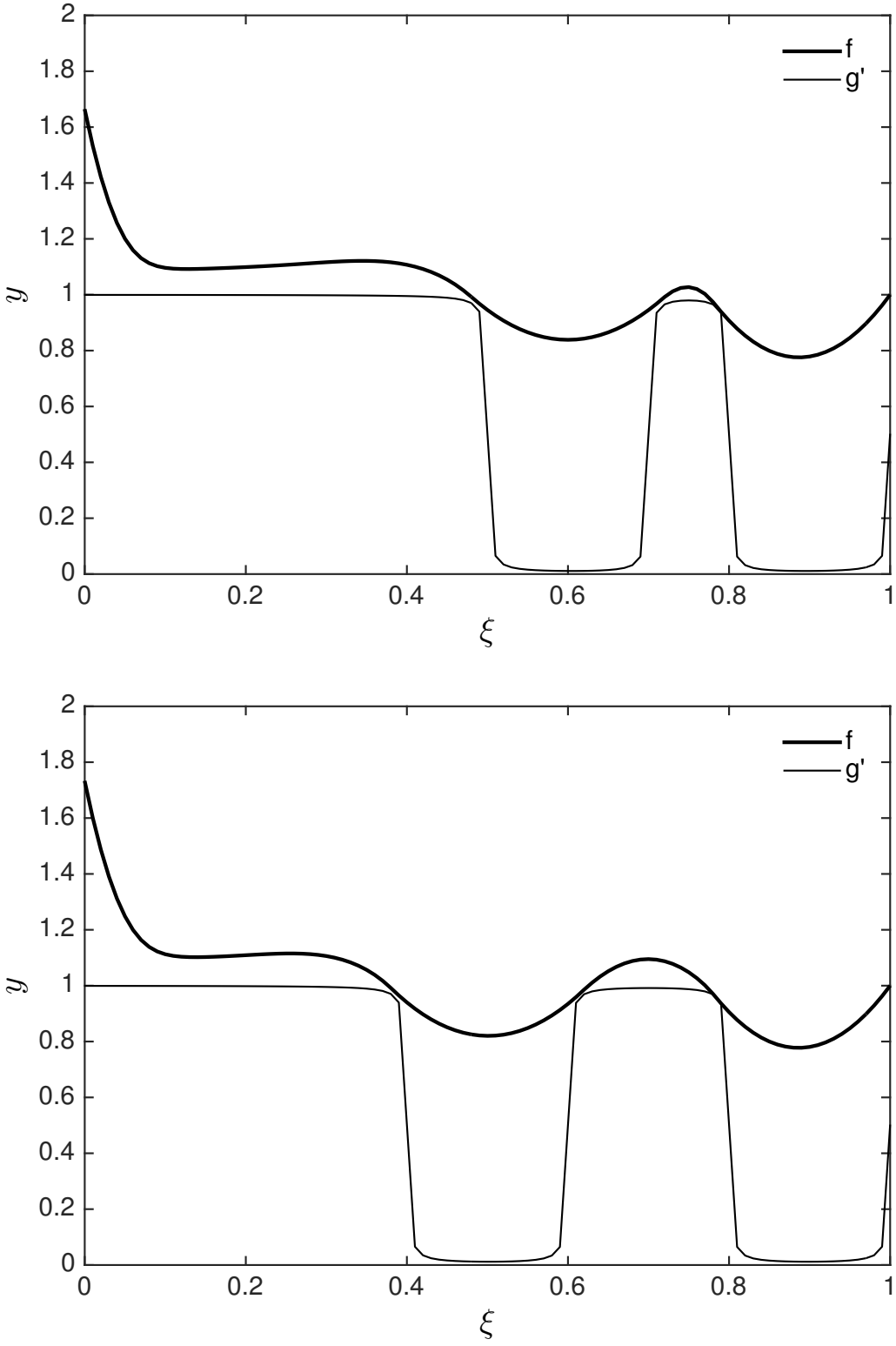

Figure 4.28: Film shape at t'=20 with two cells, Ca=0.01, $\theta = 55^o$, $\epsilon = 0.01$, cell spacing (top) $L/2$, (bottom) L.

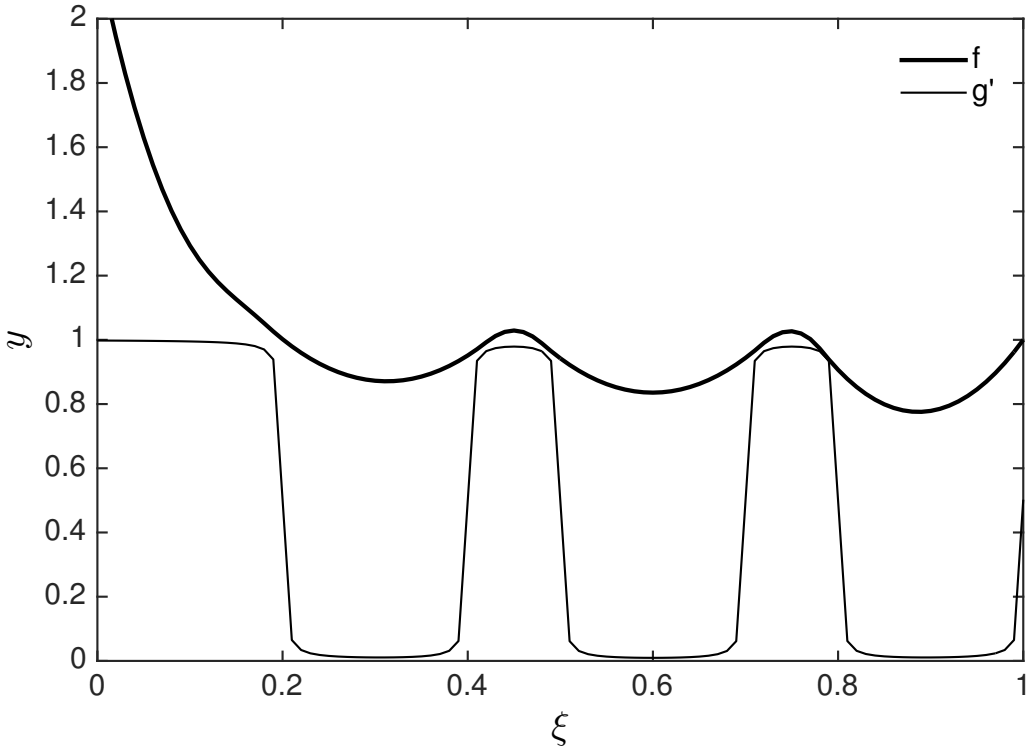

Figure 4.29: Film shape at t'=20 with three cells, Ca=0.01, $\theta = 55^o$, $\epsilon = 0.01$, cell spacing $L/4$.

Chapter 5

Conclusions

Smear formation during gravure printing of organic electronics degrades the printed features and it forms throughout the wiping stage of the process. The fluid mechanics problems motivated from this have been analyzed showing that smear formation mechanism occurs in a plane flow approximation, also.

We have reduced the problem into two canonical problems: meniscus growth and tail formation. The fluid mechanics of the problem is governed by the Stokes equations of motion owing to the small size of the cell, and to be able to solve corresponding Stokes problems, we wrote a finite element based solver using an unstructured moving mesh.

In the first stage, we have shown that liquid is drawn from the cell as it translates beneath the stationary blade; the limit $Ca \to 0$ sets an upper bound for the smear volume to be printed as tail later in time. This volume is function of Ca number, contact angle θ between liquid and blade and blade angle β. It be decreased by increasing θ, contact angle hysteresis, Ca and/or β.

We have shown that, for vanishing Ca, as the substrate continues translating, the meniscus is separated from the cell; the mechanism forming the tail operates solely between the blade and the trailing edge of the cell. Viscosity enters when the interface touches the trailing edge of the cell. An inner and outer analysis of the meniscus printing problem in the limit of $Ca \to 0$ shows that viscosity rotates the meniscus around the trailing edge of the cell by a squeeze film flow.

By solving the corresponding Stokes problem of meniscus printing, we have observed the predicted meniscus rotation. As Ca is decreased, tail length increases. As Ca approaches order unity, however, tail formation occurs on a shorter length scale, because the meniscus growth stage is limited by the viscous effects as Ca is increased.

As the Stokes solution of the problem is computationally expensive for small Ca, we formulated corresponding problem in the lubrication regime and showed that there exists an inner (squeeze film) and outer (static) structure as $Ca \to 0$. The Stokes solver should be improved to be able to integrate Stokes equations of motions for small Ca, as well as to increase the resolution in the neighborhood of the moving contact line.

By adding a sequence of cells into the model, we concluded that tail formation still exists

behind the last cell in the sequence because of the accumulation of liquid under the meniscus which is contributed from each individual cell.

There are two key intellectual contributions of the dissertation. The first contribution is that we have reduced the problem of minimizing the smear volume formation during wiping stage of gravure printing of electronics to one of reducing the upper bound set by the analysis as $Ca \to 0$. We showed that this volume can be decreased by increasing θ, Ca and β either independently or together. The second contribution is that the inner and outer analysis of printing a meniscus set the foundation of understanding the effect of viscosity which enters first from the contact line when the interface touches the trailing edge of the cell. There is one analytic problem still open: the connection between the two dynamic regions, from squeeze film flow to the Landau–Levich film, as the substrate translates further away.

Appendix A

Numerical Method for Lubrication Analysis

In this section, we give the numerical method used to integrate the free initial boundary value problem used in the lubrication models. We give the method as general and modify it according to the model problem in a stretched domain.

We employ a finite difference method. We first discretize the equations in space, and then in time and employ Newton's method because the evolution equation is a fourth order non–linear diffusion equation.

We approximate the solution ζ at a grid point x_i and time t_n by u_i, i.e.

$$u_i \approx \zeta(x_i, t_n), \tag{A.1}$$

and we let f_i represent the discretization of the terms in space. Then at every node x_i, we define an ODE in the form:

$$\frac{du_i}{dt} + f_i = 0. \tag{A.2}$$

The components of f_i include the space discretization of the convective and diffusion terms. The convective term can be discretized using a second order finite difference as follows:

$$\left(\frac{\partial \zeta}{\partial x}\right)_i \approx \frac{1}{2\Delta x}\left(u_{i+1} - u_{i-1}\right). \tag{A.3}$$

The diffusion term:
We first define the diffusion coefficient as

$$d(\zeta) = (\zeta - g)^3, \tag{A.4}$$

and then rewrite the diffusion term and approximate by

$$\frac{\partial}{\partial x}\left(d(\zeta)\frac{\partial^3\zeta}{\partial x^3}\right) = \frac{\partial}{\partial x}\left(D(\zeta)\right) \approx \frac{1}{\Delta x}\left(D_{i+1/2}(u) - D_{i-1/2}(u)\right), \tag{A.5}$$

$$D_{i+1/2} = d_{i+1/2}\left(\frac{\partial^3 u}{\partial x^3}\right)_{i+1/2}, \tag{A.6}$$

$$D_{i-1/2} = d_{i-1/2}\left(\frac{\partial^3 u}{\partial x^3}\right)_{i-1/2}. \tag{A.7}$$

To discretize the third order derivative, we employ a second order central difference scheme which is given by

$$\frac{\partial^3 u}{\partial x^3} = \frac{1}{\Delta x^3}\left(-u_{i-1} + 3u_i - 3u_{i+1} + u_{i+2}\right). \tag{A.8}$$

The approximation of the diffusion coefficient should be second order as well to get a second order scheme. We employ the Positivity Preserving Scheme of Zhornitskaya and Bertozzi (2000) as follows:

$$d_{i+1/2} = \begin{cases} \frac{2(u_{i+1}-g_{i+1})^2(u_i-g_i)^2}{(u_{i+1}-g_{i+1})+(u_i-g_i)} & (u_{i+1}-g_{i+1}) \neq (u_i-g_i) \\ (u_i-g_i)^3 & (u_{i+1}-g_{i+1}) = (u_i-g_i) \end{cases}, \tag{A.9}$$

$$d_{i-1/2} = \begin{cases} \frac{2(u_i-g_i)^2(u_{i-1}-g_{i-1})^2}{(u_i-g_i)+(u_{i-1}-g_{i-1})} & (u_i-g_i) \neq (u_{i-1}-g_{i-1}) \\ (u_i-g_i)^3 & (u_i-g_i) = (u_{i-1}-g_{i-1}) \end{cases}. \tag{A.10}$$

We use a standard implicit θ–scheme to integrate the ODE set given by

$$\frac{u_i^{n+1} - u_i^n}{\Delta t} + \theta f_i^n + (1-\theta) f_i^{n+1} = 0, \quad i = 1, ..., N+1, \tag{A.11}$$

where $0 < \theta < 1$ and N is the number of elements used in the discretization. When $\theta = 1$, the scheme is explicit, when $\theta = 0$, the scheme is implicit and first order backward Euler scheme, when $\theta = 1/2$ the scheme is a second order Crank–Nicholson scheme. The resulting system is a system of $N+1$ nonlinear algebraic equations for the unknown u_i^{n+1} for i=1,...,N+1; therefore we employ Newton's method.

To do so, we linearize the system of equations around a guess of the solution, u^*, then solve the resulting linear system for the correction, c. We then correct the guess and continue the iteration until we reach to a predefined convergence criteria. The solution at time $n+1$ in terms of guess and correction is given by

$$u_i^{n+1} = u_i^* + c_i, \quad i = 1, ..., N+1. \tag{A.12}$$

A possible guess is the solution from the previous time step, u_i^n. f_i includes the non–linear terms. We linearize it by expanding into a Taylor series around u_i^*:

$$f_i^{n+1} = f_i^* + \left.\frac{\partial f_i}{\partial c_j}\right|_* c_j, \quad i = 1, ..., N+1. \tag{A.13}$$

We now rewrite (A.11):

$$u_i^{n+1} - u_i^n + \Delta t\theta f_i^n + \Delta t(1-\theta) f_i^{n+1} = 0, \tag{A.14}$$

and by using (A.12) and (A.13), we obtain

$$u_i^* + c_i - u_i^n + \Delta t\theta f_i^n + \Delta t(1-\theta)\left(f_i^* + \left.\frac{\partial f_i}{\partial c_j}\right|_* c_j\right) = 0. \tag{A.15}$$

By rearranging (A.15), we obtain

$$\left(\delta_{ij} + \Delta t(1-\theta)\left.\frac{\partial f_i}{\partial c_j}\right|_*\right) c_j = u_i^n - u_i^* - \Delta t\theta f_i^n - \Delta t(1-\theta) f_i^* = R_i. \tag{A.16}$$

Here, $\frac{\partial f_i}{\partial c_j}$ is the Jacobian matrix which is evaluated using the guess u_i^*. Solve for the correction c_j and correct the guess to reach the tolerance.

Finally, we form the linear system for the correction evaluating (A.16) at the discretization points as

$$\underline{\underline{A}} \quad \underline{c} = \underline{R}. \tag{A.17}$$

The matrix $\boldsymbol{A}$ and the residual vector $\boldsymbol{R}$ are modified for the boundary conditions, generally, first and last two nodes.

Appendix B

Numerical Integration of Inner Viscous Problem over Semi–Infinite Domain

The inner viscous problem is of the form

$$\frac{\partial \hat{y}}{\partial \hat{t}} + f = 0, \tag{B.1}$$

where

$$f = -\hat{x} + \frac{1}{3}\frac{\partial}{\partial \hat{x}}\left\{\left(\hat{\phi}\hat{x} + \frac{1}{2}\hat{x}^2 + \hat{y}\right)^3 + \frac{\partial^3 \hat{y}}{\partial \hat{x}^3}\right\}, \tag{B.2}$$

which is valid for $0 \leq \hat{x} < \infty$. The implicit solver is as in Appendix A. The only difference here is that we map the semi–infinite region $0 \leq \hat{x} < \infty$ onto a finite region $0 \leq z < 1$ using a uniform grid. This mapping helps in a way that the boundary conditions at infinity become boundary conditions at a finite location, therefore catching the correct behavior as $\hat{x} \to \infty$ and better resolution as $\hat{x} \to 0$. We consider a general mapping of the form

$$z = m(\hat{x}), \tag{B.3}$$

and we use an algebraic mapping of the form

$$z = \frac{\hat{x}}{\hat{x}+1} \quad or \quad \left(\hat{x} = \frac{z}{1-z}\right). \tag{B.4}$$

The solution is now given in terms of $\hat{y}(z)$ and the third derivative of $\hat{y}$ is given by

$$\frac{\partial^3 \hat{y}}{\partial \hat{x}^3} = \left(\frac{\partial z}{\partial \hat{x}}\right)^3 \frac{\partial^3 \hat{y}}{\partial z^3} + 3\frac{\partial z}{\partial \hat{x}}\frac{\partial^2 z}{\partial \hat{x}^2}\frac{\partial^2 \hat{y}}{\partial z^2} + \frac{\partial^3 z}{\partial \hat{x}^3}\frac{\partial \hat{y}}{\partial z}. \tag{B.5}$$

with the derivatives of mapping:

$$\frac{dz}{d\hat{x}} = (1-z)^2, \tag{B.6}$$

$$\frac{d^2z}{d\hat{x}^2} = -2(1-z)^3, \tag{B.7}$$

$$\frac{d^3z}{d\hat{x}^3} = 6(1-z)^4. \tag{B.8}$$

Bibliography

K. J. Bathe. *Finite Element Procedures*. Prentice Hall, 1996.

R. G. Cox. *J. Fluid Mech.*, 168:169–194, 1986.

J. Eggers. *Phys. Fluids*, 17:082106–1–10, 2005.

G. Green. *Philos. Mag.*, 35:250–262, 1944.

P. I. Gutenev, A. M. Pyatnitskii, and N. V. Klimova. *Colloid Journal*, 65:301–304, 2002.

L. M. Hocking. *Q. J. Mechanics Appl. Math.*, 36:55–69, 1983.

R. Hoffman. *J. Colloid Sci.*, 50:228–241, 1975.

C. Johnson. *Numerical Solution of Partial Differential Equations by the Finite Element Method*. Dover, 2009.

B. Kang, W. H. Lee, and K. Cho. *ACS Appl. Mater. Interfaces*, 5:2302–2315, 2013.

R. Kitsomboonloha and V. Subramanian. *Langmuir*, 30:3612–3624, 2014.

R. Kitsomboonloha, S. J. S. Morris, X. Rong, and V. Subramanian. *Langmuir*, 28:16711–16723, 2012.

S. Kumar. *Annu. Rev. Fluid Mech.*, 47:67–94, 2015.

S. H. Lamb. *Hydrodynamics*. Dover, 6th edition, 1975.

L. Landau and B. Levich. *Acta Physicochim.*, 17:42–54, 1942.

C. Marangoni. *Ann. Phys. Chem.*, 143:337–354, 1871.

H. A. D. Nguyen, K.-H. Shin, and D. Lee. *Jpn. J. Appl. Phys.*, 53:05HC04–1–05HC04–6, 2014.

Y. Y. Noh, N. Zhao, M. Caironi, and H. Sirringhaus. *Nat. Nanotechnol.*, 2:784–789, 2007.

P.-O. Persson. PhD thesis, MIT, 2004.

P.-O. Persson and G. Strang. *SIAM Review*, 46:329–345, 2004.

D. Quéré. *C.R. Acad. Sci. Paris*, 313:313–318, 1991.

S. N. Reznik, W. Salalha, Y. Sorek, D. Avramov, and E. Zussman. *Phys. Fluids*, 21:102001–1–14, 2009.

S. Richardson. *Math. Proc. Camb. Phil. Soc.*, 67:477–489, 1970.

K. J. Ruschak. *Int. J. Num. Meth. Engng.*, 15:639–648, 1980.

K. J. Ruschak. *Ann. Rev. Fluid Mech.*, 17:65–89, 1985.

E. B. Secor, S. Lim, H. Zhang, C. D. Frisbie, L. F. Francis, and M. C. Hersam. *Adv. Mater.*, 26:4533–4538, 2014.

W. J. Silliman and L. E. Scriven. *Phys. Fluids*, 21:2115–2116, 1978.

J. E. Sprittles and Y. D. Shikmurzaev. *Int. J. Numer. Meth. Fluids*, 68:1257–1298, 2012.

L. E. Stillwagon and R. G. Larson. *J. App. Phys.*, 63:5251–5258, 1988.

L. H. Tanner. *J. Phys. D*, 12:1473–1484, 1979.

O. V. Voinov. *Fluid Dyn.*, 11:714–721, 1976.

H. Wong, I. Fatt, and C. J. Radke. *J. Colloid Interface Sci.*, 184:44–51, 1996.

T. Young. *Phil. Trans.*, 84, 1805.

L. Zhornitskaya and A. L. Bertozzi. *J. Numer. Anal.*, 37:523–555, 2000.